DISSERTATION

A HAVERSIAN BONE MODEL OF FRACTURE HEALING IN A SIMULATED MICROGRAVITY ENVIRONMENT

Submitted by

Benjamin C. Gadomski

School of Biomedical Engineering

In partial fulfillment of the requirements

For the Degree of Doctor of Philosophy

Colorado State University

Fort Collins, CO

Summer 2015

Doctoral Committee:

Advisor: Christian M. Puttlitz

Ray Browning
Tammy Donahue
Paul Heyliger

ABSTRACT

A HAVERSIAN BONE MODEL OF FRACTURE HEALING IN A SIMULATED MICROGRAVITY ENVIRONMENT

Ground-based models of weightlessness and microgravity have provided valuable insights into how dynamic physiological systems adapt or react to reduced loading. Almost all of these models have used rodent hindlimb unloading as the means to simulate microgravity on isolated physiological systems. Unfortunately, results derived from rodent studies are significantly limited when one tries to translate them to the human condition due to significant anatomical and physiological differences between the two species. Therefore, it is clear that a novel animal model of ground-based weightlessness that is directly translatable to the human condition must be developed in order for substantial progress to be made in the knowledge of how microgravity affects fracture healing. In light of this, four specific aims are proposed: (1) develop a ground-based, ovine model of skeletal unloading in order to simulate weightlessness, (2) interrogate the effects of the simulated microgravity environment on bone fracture healing using this large animal model, (3) develop a computational model of weightbearing in ovine bone under different experimental conditions in order to characterize the loads experienced by the fracture site, and (4) develop countermeasures that enhance bone fracture healing in the presence of simulated microgravity. Successful completion of this project will substantially elevate the understanding of how fracture site loading affects the subsequent healing cascade in the presence of microgravity and will form the foundation for designing future rehabilitation protocols to facilitate bone healing during long-duration spaceflight.

ACKNOWLEDGMENTS

I have received support, guidance, and friendship from many individuals. Dr. Christian Puttlitz has been a brilliant mentor and an exceptional friend whose guidance has made the successful completion of this project possible. I would like to extend thanks to my committee members Ray Browning, Tammy Donahue, and Paul Heyliger for their support as this project transitioned from a proposal to a completed study.

Special thanks are directed to Dr. Kirk McGilvray and Dr. Jeremiah Easley for their tireless work, encouragement, and mentorship as well as Dr. Ross Palmer, Dr. Dana Ruehlman, and Kim Lesbock. Last, but certainly not least, thanks to my past and present OBRL team: Dr. Ugur Ayturk, Cecily Broomfield, Kevin Labus, Nicole Ramo, Dr. Brandon Santoni, Dr. Snehal Shetye, and Dr. Kevin Troyer for their friendship and assistance.

DEDICATION

To my loving fiancé and best friend, Sarah, and my loving parents, Jay and Holly. Thank you for your never-ending love, support, encouragement, and belief in me.

TABLE OF CONTENTS

LIST OF TABLES

LIST OF FIGURES

LIST OF EQUATIONS

CHAPTER 1:

BACKGROUND

Bone

Macrostructure

Bone is a complex material that is often divided into numerous subsets depending on the scale of observation. At the highest observational level, the structure of mineralized tissue is divided into two categories: cortical (compact) bone and trabecular (cancellous) bone (Figure 1). Cortical bone comprises the diaphysis and thin peripheral shell surrounding the metaphysis of long bones and is characterized by its highly compact, dense microarchitecture. Trabecular bone constitutes the interior region of long bone metaphyses and spinal vertebral bodies. From a microstructural perspective, cortical bone is characterized by regular, cylindrically shaped lamellae, whereas trabecular bone possesses an irregular network of lamellae creating a highly anisotropic microstructure (116). Trabecular bone is further characterized by rod-like or plate-like geometric struts that separate its interior into interconnected pores (indicative of either low-density, open microarchitectures or high-density, closed microarchitectures, respectively) (96).

The differentiation between cortical bone and trabecular bone is commonly based on the relative density (i.e. ratio of specimen density to fully dense cortical bone) of the mineralized tissue. Cortical bone is typically characterized by a relative density between 0.7 g/cm^3 and 0.95 g/cm^3 while the density of trabecular bone varies between 0.05 g/cm^3 and 0.70 g/cm^3 (96). Large deviations in mechanical properties are common in trabecular bone due to its high level of variability in porosity and microarchitectural organization (38). Further, the inherently porous

nature of trabecular bone makes it fundamentally weaker than cortical bone (38). In addition to porosity level, the mechanical properties of bone vary greatly by mineralization level, organization of the solid matrix, and water content. The elastic modulus of cortical and trabecular bone has been reported to range between 10-20 GPa, and 0-4000 MPa, respectively (24, 32, 59, 115).

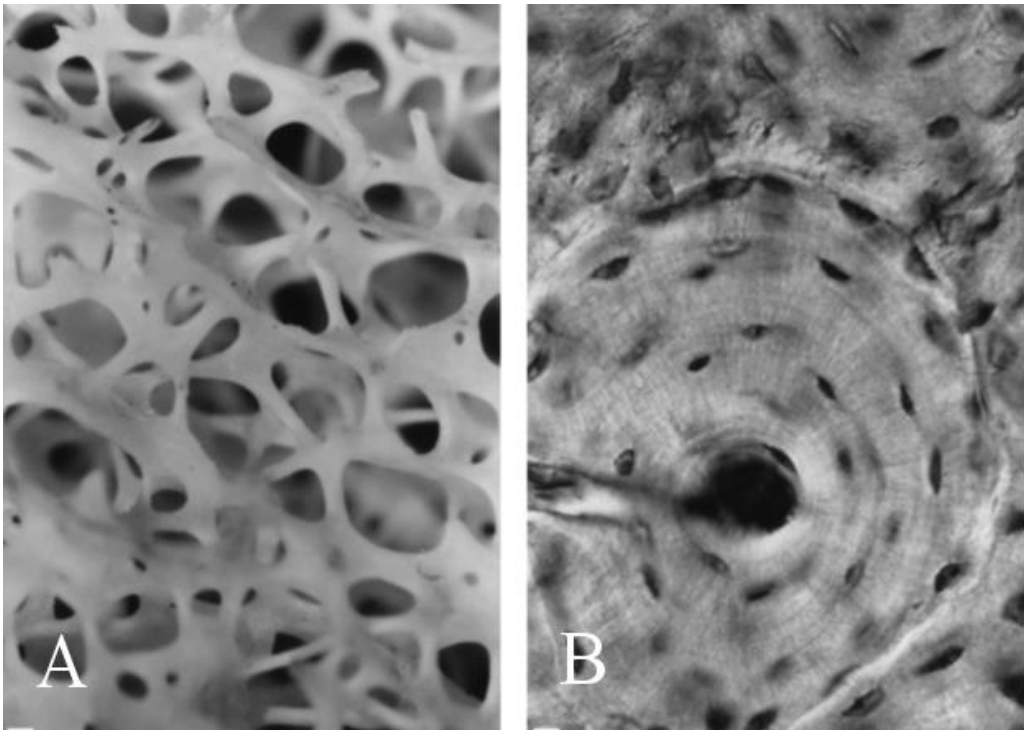

Figure 1. (A)Trabecular bone consists of a network of rod and plate-like structures, while (B) cortical bone is formed by concentric lamellar layers of bone around a central Haversian canal (17).

Microstructure

Bone tissue is a multiphase composite material with a complex hierarchal microstructure consisting of geometric structures ranging from 1 nm to 500 μm in size (Figure 2) (112, 116). Bone consists of three principal constituents: (1) a fibrous organic matrix known as osteoid, and

composed of 90% type-I collagen with the remainder comprised of glycosaminoglycans and glycoproteins; (2) a calcium phosphate and calcium carbonate-based mineral phase, mainly hydroxyapatite; and (3) water (96, 153). Water accounts for 20% of the wet weight of bone, while the collagen and mineral constituents comprise the remainder (24).

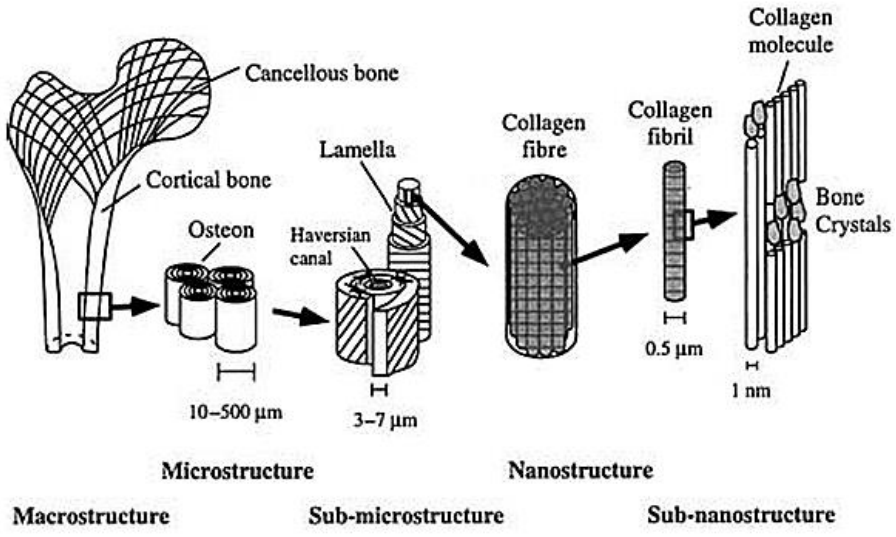

Figure 2. The hierarchal structure of human bone consists of a network of collagen fibrils circumferentially layered around a vascular channel (1).

On the nanoscale, bone is comprised of type-I mineralized collagen fibrils bundled together by carbonated apatite nanocrystals. These fiber bundles are organized into planar sheets known as lamellae. The largest structures in human bone are comprised of lamellae arranged in complex concentric layers surrounding a central vascular channel (Haversian system) that is approximately 200 µm to 500 µm in diameter (96, 116).

At the microstructural level, bone may be divided into three categories: (1) woven-fibered bone; (2) primary bone (primary lamellar, plexiform, or primary osteonal); and (3) secondary osteonal

(Haversian) bone. Woven-fibered bone is characterized by randomly oriented collagen fibers, and due to its loose packing and high porosity, is typically less dense and weaker than other types of bone (Figure 3). Woven-fibered bone is unique in that it may be deposited *de novo* and does not require any previous mineralized tissue or cartilage as a precursor. Due to these characteristics, woven-fibered bone is predominately found at birth and in the early stages of skeletal repair, specifically during early callus formation (87).

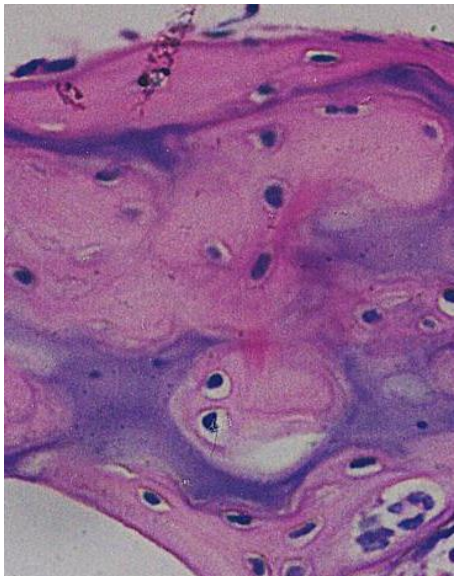

Figure 3. Woven-fibered bone is characterized by its unorganized, loosely-packed microstructure (90).

Primary bone differs from woven-fibered bone in that it must be deposited on a pre-existing substrate. There are three types of primary bone: (1) primary osteonal bone; (2) primary lamellar bone; and (3) plexiform bone, each type possessing a unique function. Primary osteonal bone is formed after birth by the successive deposition of bony matrix over previously formed woven-fibered bone and is characterized by concentric lamellar rings surrounding a single vascular channel (primary osteon) (87). The second type of primary bone, lamellar bone, is the main

constituent of trabecular bone and is characteristically very dense, lacks vascularization, and is arranged in circumferentially-oriented rings (lamellae) around the bone (Figure 4A). The final type of primary bone, plexiform bone, is often found in large, rapidly growing animals such as cows and occasionally during periods of rapid growth in humans (i.e growth spurts). Since it is primary bone, a pre-existing substrate must be provided for the development of plexiform bone. This process occurs when minerals buds grow from the periosteal or endosteal bone surfaces and combine to form a dense, brick-like microstructure (87). Plexiform bone is similar to woven-fibered bone in that it is quickly deposited; however, it provides much greater mechanical strength due to its denser microarchitecture (Figure 4B).

The final type of bone, secondary osteonal bone, is structurally similar to primary osteonal bone; however, the formation process of secondary osteonal bone differs from that of primary bone. As opposed to primary bone where new bone is built up over a pre-existing substrate, secondary bone is formed by the removal of precursor mineralized tissue (resorption) and subsequent deposition of new bone around a vascular channel to form a secondary osteon (Figure 4C) (87). The majority of the human skeleton is comprised of secondary osteonal bone.

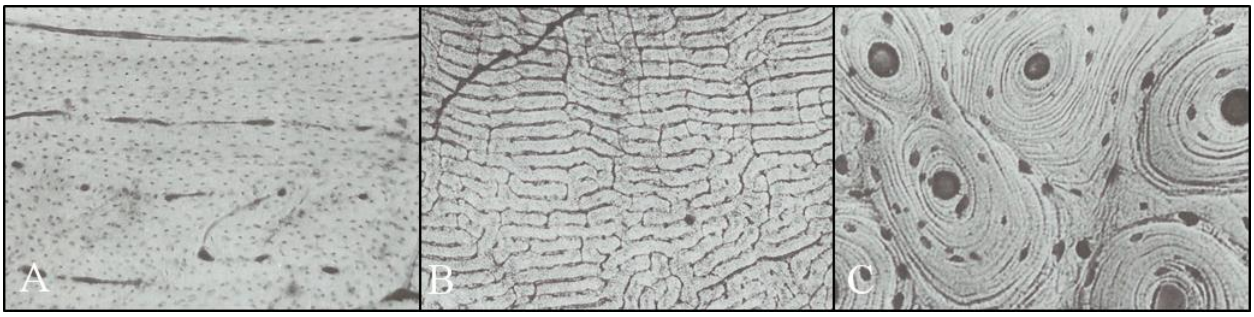

Figure 4. Diagram of the types of primary and secondary bone. (A) primary-lamellar bone; (B) plexiform bone; and (C) secondary osteonal bone (87).

Modeling and Remodeling

Bone is a metabolically active tissue that exhibits a capacity for self-repair, continuously adapting to mechanical stimuli through the formation and resorption of mineralized tissue. Three cell types are responsible for the remodeling and maintenance of bony tissue: (1) osteoblasts, (2) osteoclasts, and (3) osteocytes. Osteoblast cells regulate bone formation by directly depositing new bone tissue (i.e. osteoid), while osteoclasts are responsible for the removal of mineralized tissue through the resorption process. Finally, osteocytes are former osteoblasts that have become encapsulated in osteoid during bone formation and serve as strain-sensitive mechanotransductors that activate cell-signaling pathways to stimulate the bone remodeling process (96, 103, 117, 118, 132, 145).

Bone achieves skeletal maturity and adapts to environmental variations through the modeling and remodeling processes, respectively. Bone modeling begins at development and continues until skeletal maturity is achieved. During gestation, long bones are formed by cartilaginous tissue (chondrocytes). These chondrocytes undergo proliferation and eventual hypertrophy through water accumulation, eventually mineralizing to become woven-fibered bone, primary osteonal bone, and finally secondary osteonal bone (17, 96).

Following its initial development, human bone exhibits a capacity for self-repair and adaptation through the remodeling process, continually adjusting to alterations in mechanical stimuli to maintain mechanical competency through the transformation of its internal microarchitecture (96, 117). This principle of functional skeletal adaptation is known as Wolff's Law (156). Variations in the mechanical environment of mineralized tissue are detected through local

mechanotransductors that serve to activate cell-signaling pathways to initiate the removal and replacement of discrete packets of bone to optimize structural efficiency (18, 19, 117).

Remodeling is a coupled process in which bone resorption and deposition are performed in tandem, executed cooperatively by osteoblasts and osteoclasts in basic multicellular units (BMUs) within the cortical and trabecular bone (Figure 5).

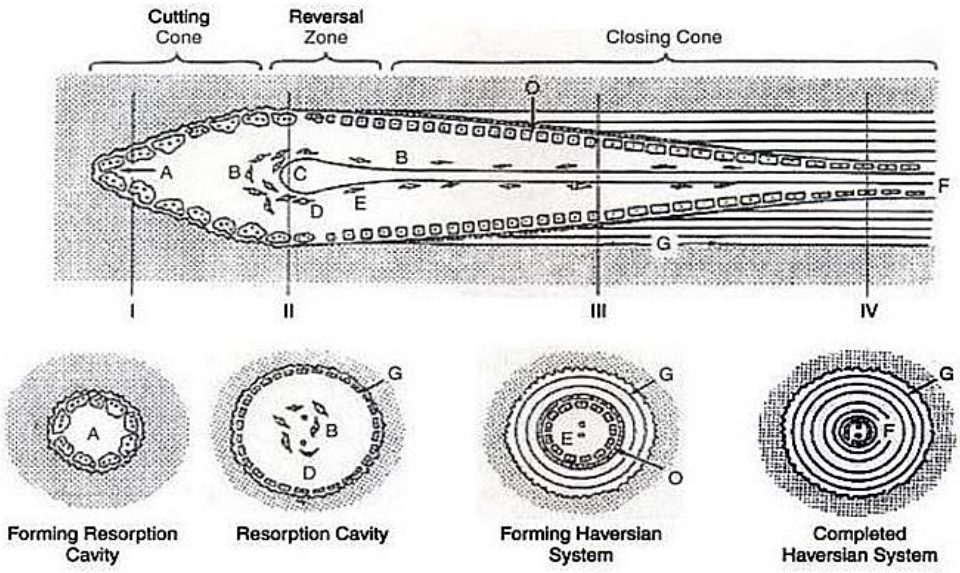

Figure 5. Longitudinal cross-sectional illustration of a cortical Basic Multicellular Unit (BMU) and corresponding transverse cortical bone cross-sections (21).

The geometric structure differs between cortical and trabecular BMUs, however, the physiologic function does not. Cortical BMUs possess a cylindrical shape approximately 2,000 µm long and 200 µm wide. The leading region of the BMU is composed of osteoclasts that burrow through the bone (cutting cone), while the tailing region of each BMU is filled with osteoblasts that deposit osteoid (closing cone), filling the tunnel and creating a secondary osteon (Haversian

system) (96, 117). The remodeling process of trabecular bone is similar to that of cortical bone, however, the execution of the process differs in that trabecular BMUs scrape and deposit bony tissue from the trabecular surfaces rather than perform a tunneling action (96, 117).

Effects of Microgravity on the Skeletal System

Microgravity and the inherent lack of mechanical loading encountered during spaceflight have been shown to produce a variety of deleterious effects on important human physiological processes. One of the most drastic alterations due to prolonged microgravity involves a negative shift in calcium balance followed by a concomitant loss of bone mass (31, 51, 60, 143, 148, 149). The weightlessness of spaceflight has been shown to induce alterations in human body mineral metabolism consistent with increased bone resorption. Astronauts consistently display decreased intestinal calcium absorption and serum calcitonin levels combined with increased urinary calcium excretion (113, 143, 154). Decreases in cortical bone mineral density (BMD) of 1-2% per month have been reported for astronauts on long-duration spaceflights (Figure 6) (60, 148). These alterations in BMD are most pronounced in mineralized tissues that are considered weight-bearing on Earth such as the femur, tibia, and calcaneus (lower extremity) with preferential losses of trabecular bone (148). Alternatively, upper extremity bones such as the radius and ulna experience relatively small alterations in BMD (31, 149). Despite the elevated rate of bone loss during mechanical unloading, recovery of bone mineral density to baseline values is delayed upon restoration of mechanical loading (148).

The human bone loss encountered during spaceflight is predominately facilitated through increased levels of bone resorption and, to a lesser extent, decreased bone formation (13).

Astronaut blood serum markers have demonstrated increased osteoclast activation during skeletal unloading as well as decreased bone formation markers. It has been postulated that the mechanical unloading of spaceflight induces uncoupling of the skeletal resorption/formation processes, leading to a net loss in bone formation (20, 96, 143).

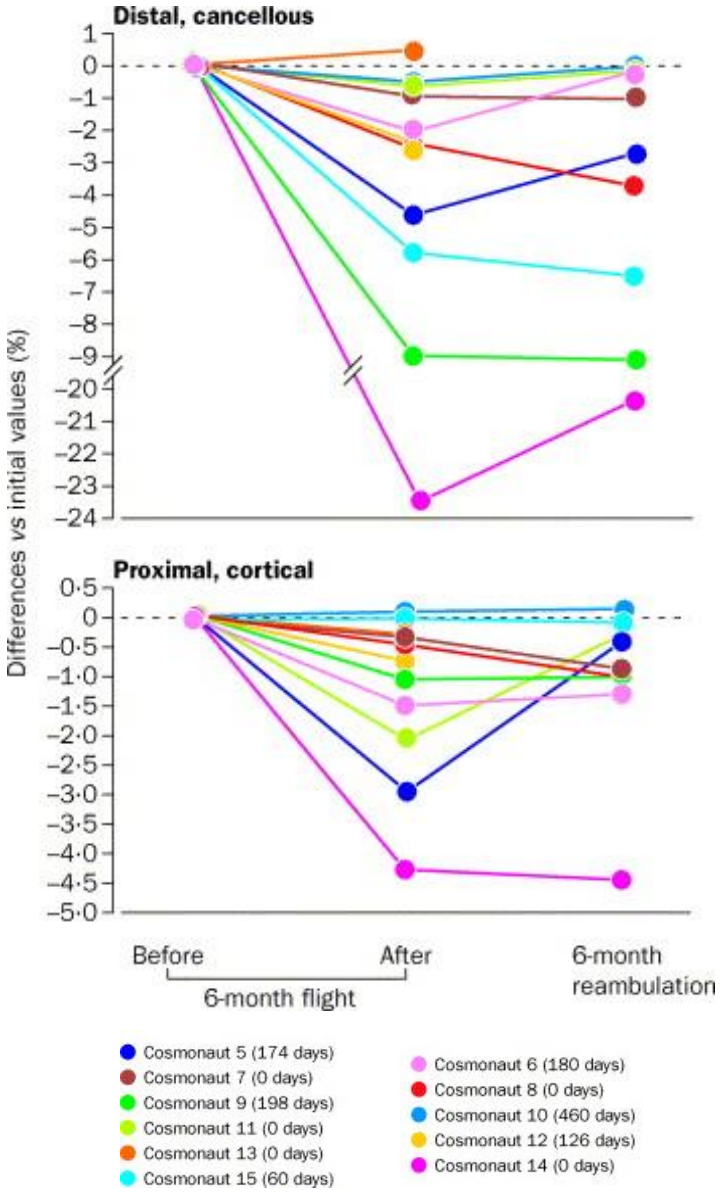

Figure 6. Astronauts experienced a 5.4% mean reduction in tibial trabecular bone mineral density and a 1.8% mean reduction in tibial cortical bone mineral density following a 6-month space station mission. Bone mineral density did not return to baseline values following the 6-month reambulation period for most astronauts (148).

Ground-Based Models of Microgravity

There are numerous technical and logistical difficulties to overcome with spaceflight research studies, such as limited specimen number and study frequency. Ground-based models are often utilized to elucidate the mechanisms behind changes of isolated physiologic systems associated with microgravity environments without the limitations of actual spaceflight animal model experimentation. Numerous human and animal ground-based models have been developed to further investigate the effects of weightlessness.

Head-Down Bed Rest

Head-down bed rest is a technique in which human subjects are immobilized in a supine position for an extended period of time while the lower extremities are elevated above the upper torso at an angle of 6 degrees, replicating the weightlessness and cephalad fluid shift experienced during spaceflight. Human head-down bed rest studies are performed to assess changes in the musculoskeletal, cardiovascular, respiratory, nervous, and metabolic systems in response to altered mechanical loading and fluid balance (28, 46, 50, 84, 126, 127, 139) and vary in length from weeks to years (13, 51, 52, 80, 81, 134, 144, 147, 161).

Despite the advantage of using human subjects, there are a multitude of shortcomings associated with the technique. Most notably, the overall physiologic alterations associated with head-down bed rest studies are comparatively subtle. Despite relatively small changes in density, alterations in bone volume in head-down bed rest studies are consistent with spaceflight measurements in that the greatest losses in BMD are observed in weight-bearing limbs (13). Further, alterations in

mineral balance mimic those associated with spaceflight such as increased urine calcium excretion and decreased intestinal calcium absorption (80, 81, 147).

Rodent Hindlimb Unloading

Rodent hindlimb unloading (HU) is the most widely-used ground-based microgravity model and extensive analyses of the relevant tissue samples has elucidated many of the microarchitectural and cellular alterations associated with weightlessness (1-3, 14, 35, 91, 138). This technique was developed to address shortcomings of earlier attempts to model microgravity (and, in the limit, full weightlessness) with protocols such as human head-down bed rest. HU rodents are suspended by their tails at an angle of 30° for the duration of the study such that their hindlimbs do not contact the ground and no longer fulfill a weight-bearing role and a cephalad fluid shift is obtained (Figure 7). Rodents are advantageous over other models due to their small size, low cost of the experimental setup, ease of accommodation and care, a well-defined genetic background, and short lifespan allowing the study of age-related changes (51, 102).

The rodent HU model has been used in an extensive spectrum of studies to investigate issues such as the effects of weightlessness on the physiology of the intervertebral disc (62), the effect of gender on bone turnover (58), how weightlessness alters ligament healing (88, 110), the effect of reloading on bone cellular detail (12), how whole body vibration affects bone during weightlessness (160), and how simulated weightlessness affects both cortical bone healing and callus formation (93, 137). Other researchers have gone on to use this model to demonstrate that resistance training is capable of reducing disuse bone loss and maintaining muscle strength (138).

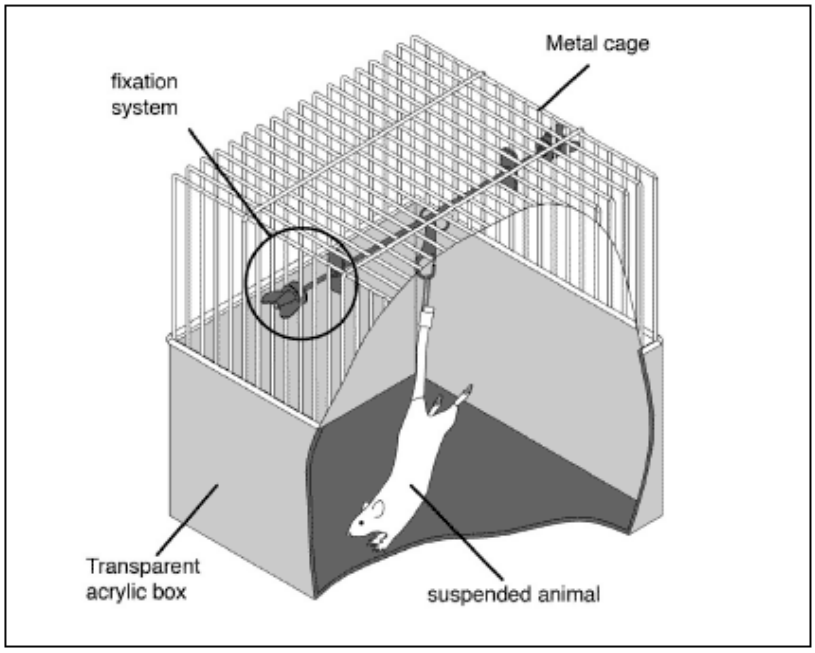

Figure 7. Diagram of the rodent hindlimb unloading experimental setup. The rodent is suspended from the ceiling of the cage such that the hindlimbs no longer fulfill a mechanical role (131).

Most relevant to the current study, rodent HU studies have elucidated many of the microarchitectural alterations associated with mechanical unloading. Rodent HU induces highly accelerated bone loss at a rate of approximately 21% per month (14). Similar to humans, rodents consistently lose trabecular bone at a greater rate than cortical bone as a result of weightlessness. These losses in trabecular bone are reflected as decreased thickness and number of individual trabeculae, increased spacing between trabeculae, and overall diminished bone volume (11, 12, 91, 95). Specifically, trabecular thickness and trabecular number have been documented to decrease between 20% and 50%, while increases in trabecular spacing nearing 180% have been reported following a 3-week unloading regimen (11, 12, 91). These modifications in trabecular microarchitecture are accompanied by diminished mechanical strength, with losses in ultimate

torque and flexural rigidity of 47% and 32%, respectively, having been reported following 3 weeks of HU (1).

At the cellular level, reduced bone formation has been identified as the underlying mechanism of the diminished skeletal health associated with the mechanical unloading of rodent HU. The total amount of active bone, referred to as the mineralizing surface (MS), has been reported to decrease by 70% in rodents as a result of weightlessness (2, 35). Mineral apposition rate (MAR), a measurement how rapidly bone is formed over a finite time interval, has been shown to decrease 30% to 90%, while bone formation rate (BFR), a calculation of the total amount of bone formed during a finite time interval, has been reported to decrease by as much as 80% following rodent HU (2, 35, 91). These alterations in bone formation are largely due to the disruption (i.e. uncoupling) of osteoblastic and osteoclastic activity. Diminished osteoblast recruitment has been widely accepted as the primary mechanism of bone deterioration in rodents exposed to weightless environments, with reductions in osteoblast numbers between 30% and 70% often associated with skeletal unloading in rodents. However, osteoclast activity and number are often unaltered following rodent HU studies (11-13, 35).

Shortcomings of Current Ground-Based Models

While there have been significant advancements using the aforementioned ground-based microgravity models to investigate unloading-related changes on various physiological systems, these models suffer from numerous shortcomings. The most notable limitation involved with human head-down bed rest investigations is that the body is not entirely removed from the gravitational loading environment, confounding the results obtained from these studies. Further,

the data obtained via human head-down bed rest studies are limited due to the ethical boundaries associated with human research.

While investigations utilizing the rodent HU technique have produced valuable information with regard to how simulated microgravity affects various physiologic systems, numerous studies have shown that there are distinct differences with regard to skeletal maintenance and fracture healing using this ground-based model and the actual mechanism through which bone heals during spaceflight. Hindlimb unloading animals generally display systemic alterations in metabolic functions that do not parallel those seen during spaceflight. Specifically, Kerchin et al. showed that suspended animals exhibit a significantly greater weight loss that those that have been sent into space (72). In addition, it has also been shown that HU animals display a baroreflex suppression of thirst in response to a cephalad fluid shift that occurs with elevation of the hindlimbs, resulting in depressed water consumption by 15% to 25% during the first week of suspension (33, 34, 97). The resulting inadequate hydration and associated changes in vascular profusion can have adverse effects on biological function and could influence bone remodeling and healing.

The ultimate goal of using an animal model is to transfer the experimental results to clinical and operational practice. Thus, the suitability of an animal model in bone research is closely related to the degree of similarity between the results obtained in the model as compared with the human condition. Results derived from rodent studies are difficult to directly translate to the human condition due to major anatomic and physiologic differences between the two species. Most importantly, the basic microstructure of rodent bone can be observed as a primary lamellar

structure and lacks the osteonal (Haversianal) systems that are the main micro-architectural feature of human cortical bone (37, 102). As such, rodent bone does not resemble the secondary osteonal structure of human mineralized tissue. These microstructural differences have a significant effect on the translatability of the rodent model to the human condition. Additionally, the rate of bone healing is known to be inversely related to the position of the species on the phylogenetic scale. Specifically, it has been extensively shown that rodents have a higher capacity to regenerate bone than humans. Accordingly, the osteogenic and healing potential of rodent bone far exceeds that of adult human tissue (37, 89), and it is believed that the increased surface area of rodent bone relative to human Haversian systems is responsible for these elevated rates of bone formation (89). Within the sequelae of various research questions, the use of the rodent model is generally accepted in the early stages of these research endeavors because these animals are generally smaller and less costly than large animal models. However, with particular regard to bone healing, the healing characteristics of the animal should approximate those of humans during the later stages of the research progression. Thus, there is critical need for a large animal-based model of microgravity that more-closely approximates the human condition.

Sheep in Orthopaedic Research

Sheep have emerged as a viable experimental model in the study of musculoskeletal conditions such as limb lengthening, osteoporosis treatment, fracture and cartilage healing, and spinal instrumentation (30, 57, 68, 86, 89, 122, 135). Adult sheep are advantageous in that they are relatively easy to handle, generally docile in nature, and relatively inexpensive. The large size of sheep makes them ideal for implantation studies as well as blood and urine sampling. They are available in large numbers, and, due to their flock nature, tend to experience the least amount of

stress when housed in groups (101). Sheep and humans share similar bodyweights, and the large size of sheep allows for multiple experimental procedures (89). Further, sheep are more similar to humans with regard to age-related changes than rodents, reaching skeletal maturity after approximately 4-5 years versus the 3-6 months required of rodents (89).

Most importantly and germane to the current study, from a microstructural perspective, adult sheep bone displays a secondary osteonal microarchitecture (Haversian systems) and undergoes remodeling in a similar fashion to humans (Figure 8) (25, 108). It has been shown that the ovine bone mineral composition and healing rate closely approximates that of humans (37). Further, sheep are commonly used as a preclinical model for new treatments or devices that seek Food and Drug Administration (FDA) approval (41).

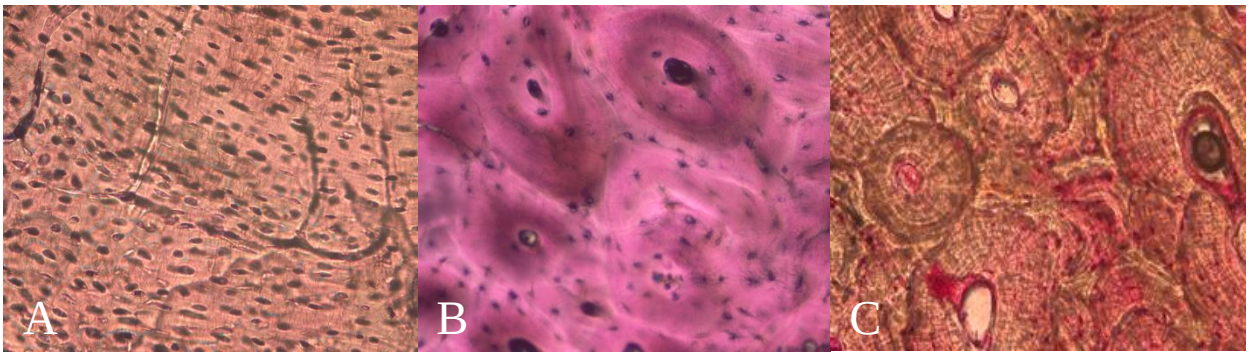

Figure 8. (A) Histological section of rodent bone demonstrating a lack of secondary osteons. (B) A transverse section of mature cortical sheep bone demonstrating numerous osteons clearly distinguished with distinct cement lines separating neighboring osteons. (C) Histological section of human compact bone demonstrating similar osteonal architecture as ovine bone.

Summary

The effects of microgravity on human physiologic systems in microgravity environments, especially with regard to skeletal maintenance and fracture healing, are not fully understood.

Limited specimen numbers and study frequency are only two of the numerous technical and logistical difficulties that must be overcome with spaceflight research studies. Numerous ground-based models of microgravity have been developed to elucidate the mechanisms behind the physiologic alterations associated with spaceflight, with the most widely used ground-based model being rodent HU. However, results obtained from these studies are difficult to translate to the human condition due to inherent differences in skeletal microarchitecture between the two species. This is especially relevant with regard to studying orthopaedic issues related to bone maintenance and fracture healing during spaceflight.

The goal of this dissertation project is to overcome the shortcomings associated with current ground-based models of microgravity and investigate the effect of microgravity environments on fracture healing in Haversian systems. In order to meet these objectives, this project is focused on: (1) the development of a ground-based, large animal model that more closely approximates the human condition; (2) interrogation of the effects of a simulated microgravity environment on bone fracture healing in the aforementioned animal model; and (3) the characterization of the localized mechanical environment of the fracture site and its subsequent role in fracture healing through computational techniques. It is hypothesized that the inherent lack of mechanical loading associated with microgravity will have a negative impact on the ability of fractured bone to heal, and, ultimately, impair the nature and quality of the osseous repair. Finally, therapeutic interventions will be evaluated in the case of impaired fracture healing in microgravity environments.

Specific Aims

In order to address the aforementioned criteria, the following specific aims are proposed:

Specific Aim 1: Develop a ground-based large animal model of bone unloading in order to simulate weightlessness.

Rodent hindlimb unloading models represent the current state-of-the-art technique for simulating the absence of gravity; however, these models suffer from limitations associated with fundamental differences in bone microstructure, the time course and extent of healing between human and rodent bone, and the inability to vary the degree of the microgravity environment. An isolated ovine metatarsus model will be utilized to overcome these shortcomings and produce a model which is more translatable to the human condition. *In vitro* and *in vivo* experiments will be performed to fully characterize the model.

Specific Aim 2: Interrogate the effects of a simulated microgravity environment on bone fracture healing in a large animal model.

In this set of experiments, the effect of weightlessness on fracture healing using biomechanical, radiographic, and histological outcome parameters will be characterized using the ovine metatarsus model developed in Specific Aim 1.

Specific Aim 3: Develop a computational model of weightbearing in ovine bone under different experimental conditions in order to characterize the loads experienced by the fracture site.

While Aims 1 and 2 will utilize strain data as the primary mechanical parameter to characterize the loading environment, this aim will develop an inverse dynamics model that will predict hindlimb muscle force generation and use these predictions as input for a high fidelity finite element model of the ovine lower extremity in order to predict what forces are being experienced by the fractured metatarsi. These data will be correlated with the *in vivo* data collected in Aim 2 to delineate how variations in the local mechanical environment lead to differential bone healing.

Specific Aim 4: Develop therapeutic countermeasures that enhance bone fracture healing in the presence of simulated microgravity.

It is well known that healing is impaired in the presence of microgravity environments. A series of experiments on sheep with fractured metatarsi treated with either shock wave therapy or low-intensity pulsed ultrasound will be performed. Appropriate outcome measures will be assessed longitudinally via *in vivo* radiography, as well as post-sacrifice micro-computed tomography scanning, bending strength testing, and histological analyses in order to assess the time course and degree of bone healing as a function of localized fracture site treatment.

CHAPTER 2:

AN *IN VIVO* OVINE MODEL OF BONE TISSUE ALTERATIONS IN SIMULATED MICROGRAVITY CONDITIONS

Introduction

Microgravity and its associated inherent reduction in body-weight mechanical loading encountered during spaceflight has been shown to produce a variety of deleterious effects on human physiological processes. One of the most drastic alterations due to prolonged microgravity involves significant loss of trabecular bone mass (31, 51, 60, 148, 149). Decreases in cortical and trabecular bone mineral density (BMD) of approximately 1-2% and 5-6% per month, respectively, have been reported for astronauts on long-duration spaceflights (60, 148). These alterations in BMD are most pronounced in mineralized tissues that are considered weight-bearing on Earth such as the femur and tibia (lower extremity), while bones such as the radius and ulna (upper extremity) experience relatively minor alterations (31, 149). Simulations of severe bone mass losses have demonstrated a significantly elevated risk of fracture during long duration spaceflight missions and after return to Earth (70, 77, 100). Therefore, temporal reductions in skeletal strength and competency are one of the foremost limiting factors preventing long distance space exploration.

[1]This chapter has been published as a Research Article in the Journal of Biomechanical Engineering (136, 021020 (2014)). The text and figures have been adapted from the American Society of Mechanical Engineers (ASME).

Ground-based models are often utilized to elucidate the mechanisms that drive alterations in isolated physiologic systems associated with microgravity environments without the limitations of actual spaceflight experimentation. Overall, rodent hindlimb unloading (HU) is the most widely-used ground-based microgravity model (1-3, 14, 35, 91, 138) and involves the suspension of rats or mice by their tails for the duration of the study such that their hindlimbs do not contact the ground and no longer fulfill a weight-bearing role. Rodents are advantageous over other models due to their small size, low cost of experimental setup, ease of accommodation and care, well-defined genetic background, and short lifespan allowing the study of age-related changes (51, 102).

Unfortunately, results derived from rodent studies are difficult to translate to the human condition due to major anatomic and physiologic differences between the two species. The basic microstructure of rodent bone is a lamellar morphology lacking the secondary osteonal systems that are the main micro-architectural feature of human cortical bone (Figure 9A) (37, 102). In contrast, human mineralized tissue is characterized by concentric rings of compact bone surrounding a central blood vessel (Figure 9C). These microstructural differences have a significant effect on the translatability of the rodent model to the human condition. Further, the rate of bone healing is known to be inversely related to the position of the species on the phylogenetic scale, with the osteogenic healing potential of rodent bone far exceeding that of adult human tissue due to the relatively smaller size of rodents (37, 89).

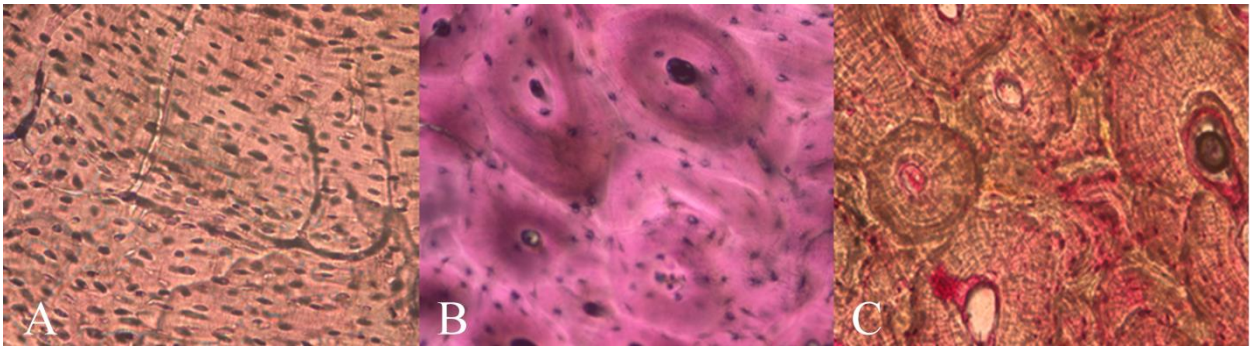

Figure 9. (A) Histological section of rodent bone demonstrating its lamellar structure and fundamental lack of secondary osteons. (B) A transverse section of mature cortical sheep bone demonstrates numerous secondary osteons. (C) Histological section of human compact bone demonstrating a similar secondary osteonal architecture as ovine bone.

Sheep have emerged as a viable experimental model in the study of musculoskeletal conditions such as osteoporosis, fracture and cartilage healing, and spinal instrumentation. As such, the ovine model has become a widely accepted preclinical model for treatments and devices seeking FDA approval (30, 41, 57, 68, 86, 89, 102, 122). Adult sheep are advantageous in that they are relatively easy to handle, generally docile in nature, and their bodyweights approximate those of adult humans (~70kg). Most importantly and pertinent to the current study, from a microstructural perspective adult sheep bone displays similar microarchitectural characteristics as human bone (Figure 9B) (108). Additionally, it has been shown that the ovine bone mineral composition and healing rate closely approximates that of humans (37).

In order to leverage the similarities between sheep and human bone microarchitecture and healing, a ground-based ovine model of microgravity was developed utilizing common external fixation instrumentation that replicates the physiologic alterations associated with weightlessness and allows direct translation of study results to the human condition.

Materials and Methods

External skeletal fixation is a commonly used technique for treating difficult (i.e. comminuted) fractures. The goal of external fixation is to stabilize the affected limb wherein the physiological loads are supported by the frame with reduced loading through the healing tissue. Typical external skeletal fixation devices utilize pins and/or wires as the bone fixation elements with external rods and rings used to connect the device. This external fixation technique was leveraged in order to specifically-unload the ovine metatarsal bone in order to simulate microgravity unloading.

The development of the ovine microgravity model involved a series of parametric *in vitro* experiments in order to determine the feasibility and effectiveness of the proposed approach. The results of these experiments provided the required rationale for the *in vivo* implementation of this technique.

In Vitro Device Characterization

A transarticular hybrid fixator was constructed using commercially-available veterinary external fixation components (IMEX, Longview, TX) to reduce the loads experienced by the metatarsal bone of the ovine hindlimb (Figure 10). A parametric benchtop study was performed wherein the measured load transmitted through the metatarsus as a function of connecting rod number, diameter, and material as well as the number, diameter, and type of fixation pins was investigated. An ovine hindlimb was dissected to include the tibia, metatarsus, and proximal phalanges. The limb was potted at the level of the phalanges and the tibia using epoxy resin (Smooth-On, Inc., Easton, Pennsylvania). An ostectomy was created at the mid-diaphysis of the

metatarsus and an in-line load cell (Honeywell International Inc., Morristown, NJ) was inserted. A servohydraulic material testing machine (MTS Systems Corporation, Eden Prairie, MN) applied a 500N load to the limb, and a non-instrumented baseline metatarsal load profile was established. The external fixation device was then attached to the hindlimb at the level of the phalanges using a large (4.0mm diameter) full (central-threaded) pin and two large (4.0mm diameter) half (end-threaded) pins.

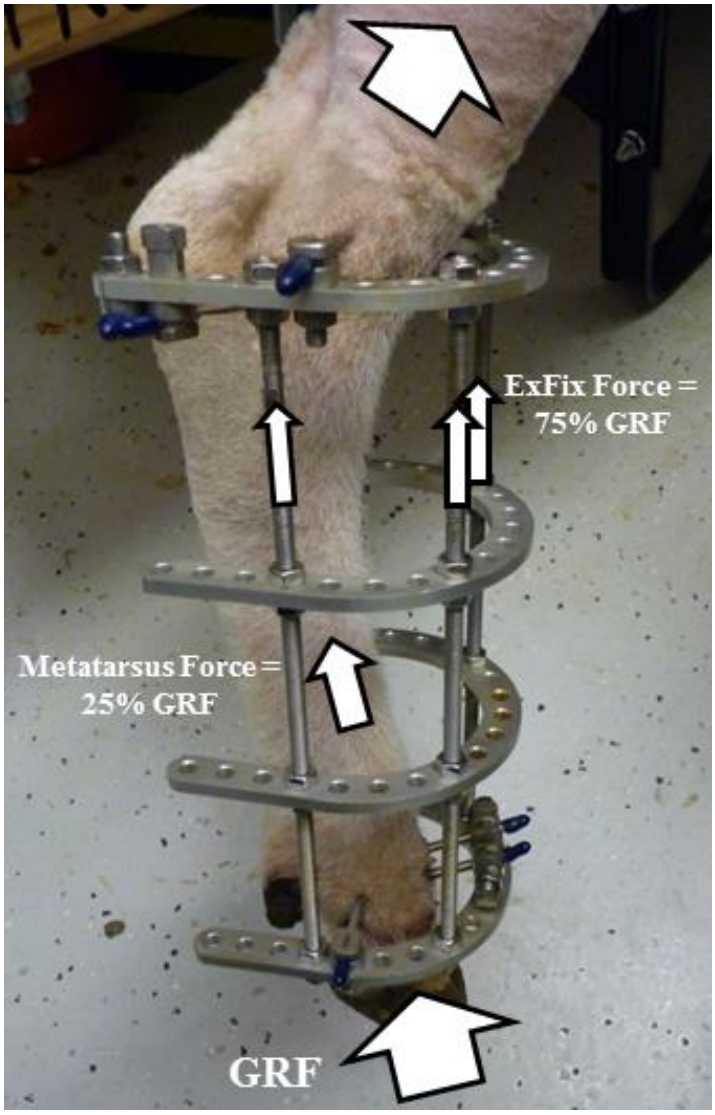

Figure 10. An external fixation unloading technique was utilized to differentially-unload the metatarsal bone of the right hindlimb. A total of 4 longitudinal connecting rods, 4 horseshoe rings, and 6 fixation

pins were utilized. In this configuration, approximately 25% of the ground reaction force (GRF) is transmitted through the metatarsal bone (0.25g), while 75% of the GRF is redirected through the external fixation device.

Combinations of medium (3.2mm diameter) and large (4.0mm diameter) half and full pins were utilized to attach the external fixation device to the tibia and calcaneus in order to investigate the resultant metatarsal unloading. Potential preload of the device incurred during installation was eliminated by adjusting the securing nuts of the proximal and distal horse-shoe attachment rings responsible for securing the fixation pins to the device. Elimination of measureable pretension imparted by the hardware to the metatarsus was confirmed via the implanted load cell. Following device installation, the loads transmitted through the metatarsus by the external fixation configurations were compared to those of the non-instrumented baseline loads in order to calculate the relative unloading of the metatarsus due to the external fixation device.

A previous pilot experiment demonstrated that direct attachment of strain gages *in vivo* cannot remain viable on living bone beyond five days post-implantation. Thus, an alternative method of collecting *in vivo* strain data was developed by reducing the central thickness of an orthopaedic locking plate (Synthes, Inc., West Chester, PA) to 500µm and instrumenting the plate with a rosette strain gage (Omega Engineering, Inc., Stamford, CT) (Figure 11). Strain measurements from the strain-measurement plates were correlated to the metatarsal surface strains during simulated hindlimb loading in a servohydraulic material testing machine (MTS Systems Corporation, Eden Prairie, MN), with the assumption that the relationship between bone and plate strain would remain consistent over time due to the dense cortical bone at the screw-bone interface. Adult ovine hindlimbs (n=10) were prepared for experimental testing as previously

described. Rosette strain gages (Omega Engineering, Inc., Stamford, CT) were attached to the mid-ventral diaphysis as well as the distal and proximal metaphyses of the dorsal face of the metatarsal bone. The strain-measurement plates were attached to the dorsal face of each metatarsus using locking screws in the proximal-most and distal-most holes. Each specimen was preconditioned 10 times to 750N at a rate of 0.25mm/sec, with data analyzed from the final cycle. A linear regression analysis was performed to correlate the principal strains measured for each strain-measurement plate to the respective principal strains at each metatarsal location. The average linear fit and respective standard error for each correlation was then calculated.

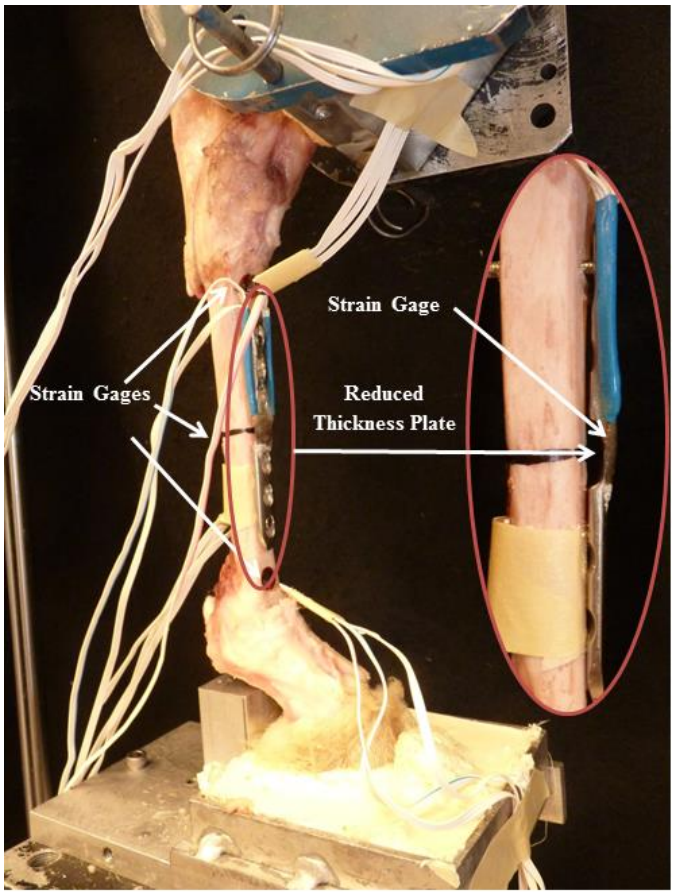

Figure 11. Ovine hindlimbs were instrumented with orthopaedic strain measurement plates and three rosette strain gages for the *in vitro* strain correlation experiments. (Inset) The central thickness of an orthopaedic locking plate was reduced to 0.50mm and instrumented with a rosette strain gage in order to increase its sensitivity to small strain fluctuations.

In Vivo Model

Ten skeletally mature Rambouillet Columbian ewes were used in this portion of the study. Approval for the surgeries performed on these animals was granted by the Colorado State University Animal Care and Use Committee (Approval #11-2938A). Under anesthesia, the strain gage wires were tunneled subcutaneously through the limb and exited near the hip joint. The strain-measurement plate was then implanted on the dorsal face of the metatarsus. An optimized transarticular hybrid fixator (IMEX, Longview, TX) was then implanted on the hindlimb of 7 sheep (Microgravity Group). The frame consisted of four 84mm stretch rings connected by four threaded longitudinal support rods (6.0mm diameter, 250.0mm length) constructed prior to surgery. Two medium (3.2mm) central-threaded full pins were placed in the distal tibia: one in a medio-lateral direction and one in a dorso-medial to plantaro-lateral oblique direction above the proximal-most horseshoe ring. A single medium (3.2mm) central-threaded full pin was placed in the medial-lateral plane through the calcaneus below the stretch ring. The distal ring was connected to 2 large (4.0mm) end-threaded fixation pins inserted proximally into the 1st distal phalanges of digits 3 and 4 and one large (4.0mm) central-threaded full pin inserted in the medial-lateral plane through the proximal portion of the same phalanges. The proximal and distal horseshoe rings were adjusted to alleviate any pretension of the longitudinal support rods incurred during the surgical procedure, allowing the reduction of compressive loading of the metatarsal bone during hindlimb use without applying any external traction forces via the external fixation device. An Earth gravity (Sham Group, n=3) test group was simulated by repeating the surgical technique of the Microgravity Group and removing the four longitudinal support rods upon completion of the procedure, allowing full load transmission through the metatarsal bone.

Uniaxial strain gages were attached to the four longitudinal support rods of each fixation system in the Microgravity Group. The *in vivo* unloading of the system was evaluated bi-weekly by testing each animal on a force measurement platform. Strain measurements from the metatarsal plate and external fixation device for single-limb ground reaction forces up to 300N were recorded for the standing animals. The strain-measurement plate correlations were utilized to calculate the corresponding metatarsus strains, and linear elastic constitutive relationships were utilized to calculate the stresses (Equation 1) and forces (Equation 2) transmitted through the metatarsal bone and external fixation device. The relative gravity of the device was calculated by taking the ratio of the metatarsus load to the total system load in order to compare the metatarsal unloading environment created by the external fixation device to other celestial (Moon, Mars, etc.) microgravities (Equation 3).

$$\sigma = E * \varepsilon \qquad \text{(Equation 1)}$$

$$F = \sigma * A \qquad \text{(Equation 2)}$$

$$\text{Relative Gravity} = \frac{\text{MetatarsalForce}}{\text{MetatarsalForce} + \text{ExFix Force}} \qquad \text{(Equation 3)}$$

Weekly radiographs were taken to monitor the bone-pin interface of each animal. Additionally, fluorochrome labels (calcein green at 20mg/kg) were administered at weeks 4 and 7 post-surgery. Dual-energy x-ray absorptiometry (DEXA) scans (Hologic, Inc., Bedford, MA) were performed on the treated and contralateral metatarsi as well as the tibia of the treated limb at the

time of surgery and every two weeks. Scans were analyzed in identical 10mm x 10mm regions of interest (ROIs) aligned with the proximal aspect of the condyle arch of the distal metaphysis of the treated and contralateral metatarsi as well as at the proximal growth plate of the ipsilateral tibia. BMD comparisons were made between the treated metatarsi and the contralateral (control) metatarsi as well as between the treated metatarsi and the ipsilateral tibia to determine if BMD changes were the result of external fixation load-shielding or generalized limb disuse. Three scans were performed per bone, and average BMD was calculated per time point for each animal.

Post-sacrifice biomechanical evaluations were performed on the treated and contralateral (control) metatarsi of the Microgravity and Sham Groups. All specimens underwent an identical testing protocol of 4-point bending followed by diametral compression in order to negate the effects of any previous testing procedure. Non-destructive four-point bending experiments were performed on whole, dissected metatarsal bones using a custom-designed, four-point bending fixture and a servohydraulic material testing machine (MTS Systems Corporation, Eden Prairie, MN). The cross-head was lowered at a rate of 1.0mm/sec to a maximum load of 500N as determined via a pilot study such that the specimen demonstrated linear material behavior without inducing permanent damage (39). The sample was preconditioned 5 times with data analyzed from the final cycle. The resultant specimen stress-strain curve and bending modulus were then calculated (39).

The normalized failure load of each specimen was determined via diametral compression experiments as described by Santoni et al (123). Three 5mm spans of cortical bone were cut from

the mid-diaphysis of each metatarsus using a diamond-chip band saw (Exakt Technologies, Oklahoma City, OK). The sections were individually placed between two smooth, stainless steel platens in a servohydraulic material testing machine (MTS Systems Corporation, Eden Prairie, MN). The orientation of each specimen was consistent between tests, with the medial and lateral aspects of the bone contacting the upper and lower platens, respectively. A compressive load was then applied at a rate of 0.5mm/min until failure was observed. The failure load of each specimen was then normalized to its respective cross-sectional area.

Micro-computed tomography (μCT) analyses were performed on distal metaphyseal sections of the treated and contralateral metatarsi from both groups (Figure 7A). Three 9mm x 9mm x 2mm ROIs were aligned with the proximal aspect of the condyle arch of the distal metaphysis such that the greatest amount of cancellous bone was included in the each ROI without overlapping ROIs. The results of the three ROIs were then averaged for each specimen. Additionally, a 2mm x 2mm x 2mm ROI was analyzed for each quadrant of the cortical shell at a distance of 50mm from the distal metatarsal condyle (within the metatarsal diaphysis) and averaged for BMD evaluation. Bone volume fraction (BV/TV), trabecular number (Tb.N), trabecular thickness (Tb.Th), trabecular separation (Tb.Sp), H2 (a measure of trabecular anisotropy), structural model index (SMI, a description of trabecular geometry), and cancellous BMD (Tb.BMD) as well as cortical BMD (C.BMD) was quantified for each μCT dataset (15, 79).

Standard histological techniques were utilized to prepare the treated and contralateral metatarsi. Sections were taken in the sagittal plane to include the distal diaphysis and metaphysis. Trabecular bone images at 10x and cortical bone images at 40x were acquired for

static and dynamic histomorphometric analyses, respectively. Additionally, trabecular bone images at 200x were acquired for static decalcified histomorphometric analyses. Measurements of cancellous bone volume fraction (B.Ar/T.Ar), diaphyseal bone diameter (B.Dm), diaphyseal cortical width (C.Wi), mineralizing surface (MS), mineral apposition rate (MAR), bone formation rate (BFR), osteoblast number (N.Ob), and osteoclast number (N.Oc) were acquired for each specimen (36, 107).

Data are reported as means $\pm$ standard deviations (SD). Statistical analysis for comparisons between groups was performed via a two-way analysis of variance (ANOVA) while a repeated measures ANOVA was used for comparisons within groups for longitudinal DEXA analysis. The Student-Newman-Keuls *post-hoc* test (α=0.05) was utilized for all statistical tests. (SigmaPlot, Systat Software, Inc., San Jose, CA).

Results

In Vitro Device Characterization

The external fixation parametric study demonstrated that the resultant simulated microgravity of the device was highly dependent on the number, material, and size of the longitudinal support rods as well as the number and size of the fixation pins (Table 1). Increasing the number of longitudinal connecting rods had a greater effect on metatarsus unloading than alterations in support rod material, while increasing the size and number of the fixation pins further increased metatarsus unloading. All mean Pearson's correlation coefficients (i.e., r^2 values) for the fracture fixation strain-measurement plate linear regression analysis were greater than 0.90, indicating a

highly linear relationship between measured plate strain and bone surface strain for all strain-measurement plates.

Table 1. An external fixation parametric study was performed by varying the number, size, and material of longitudinal support rods (left) and the number and size of fixation pins (right). The final external fixation device was comprised of four 6.35mm diameter steel rods, and three medium size full pins at the proximal interface (0.25g).

Diameter/Material of Support Rod		**Relative "g"**	**Method of Fixation with Four 6.35mm Steel Rods at Tibial/Calcaneal Interface (Number x Diameter)**		**Relative "g"**
Non-Four-Rod		1.00	**Non-Instrumented: Baseline**		1.00
	6.35mm Steel	**0.10**	**0 Half Pins**		
Three-Rod				**3 x 3.2mm Full Pins**	**0.25**
	6.35 mm Steel	0.23	**1 x 4.8mm Half Pin**		
	4.76mm Brass	0.25		2 x 4.0mm Full Pins	0.06
	4.76mm Aluminum	0.27		3 x 3.2mm Full Pins	0.20
Two-Rod				**3 x 4.0mm Full Pins**	**0.05**
	6.35mm Steel	0.57	**2 x 4.0mm Half Pins**		
	4.76mm Brass	0.65		1 x 4.0mm Full Pin	0.36
	4.76mm Aluminum	0.68	**2 x 4.8mm Half Pins**		
				1 x 4.0mm Full Pin	0.10

In Vivo Model

In vivo strain measurements revealed the average relative gravity of the external fixation system to be 0.25g (Figure 12).

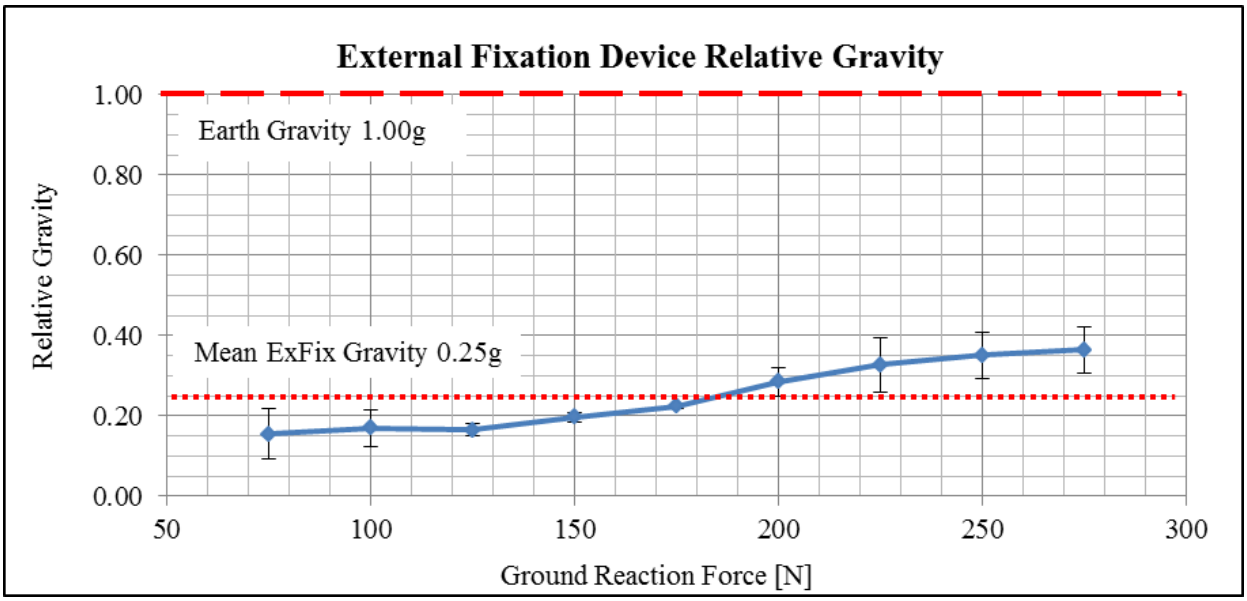

Figure 12. The *in vivo* external fixation relative gravity was quantified by calculating the metatarsus bone strains from the acquired measurement plate strains, transforming the bone and device strains into forces using linearly elastic constitutive relationships, and taking the ratio of force transmitted through the metatarsus to total force transmitted through the system.

In vivo DEXA scans demonstrated significant losses of BMD in the treated metatarsal bones of the Microgravity Group following the 8-week treatment period (Figure 13). The BMD of the treated metatarsi of the Microgravity Group displayed a linear decrease after the initial 2-week period of the study, resulting in a net loss of 29.0% ($p<0.001$) over the entire 8-week timeframe. No statistically significant alterations in BMD occurred in the contralateral metatarsi or the ipsilateral tibia of the Microgravity Group, or any scan location of the Sham Group (Figure 13).

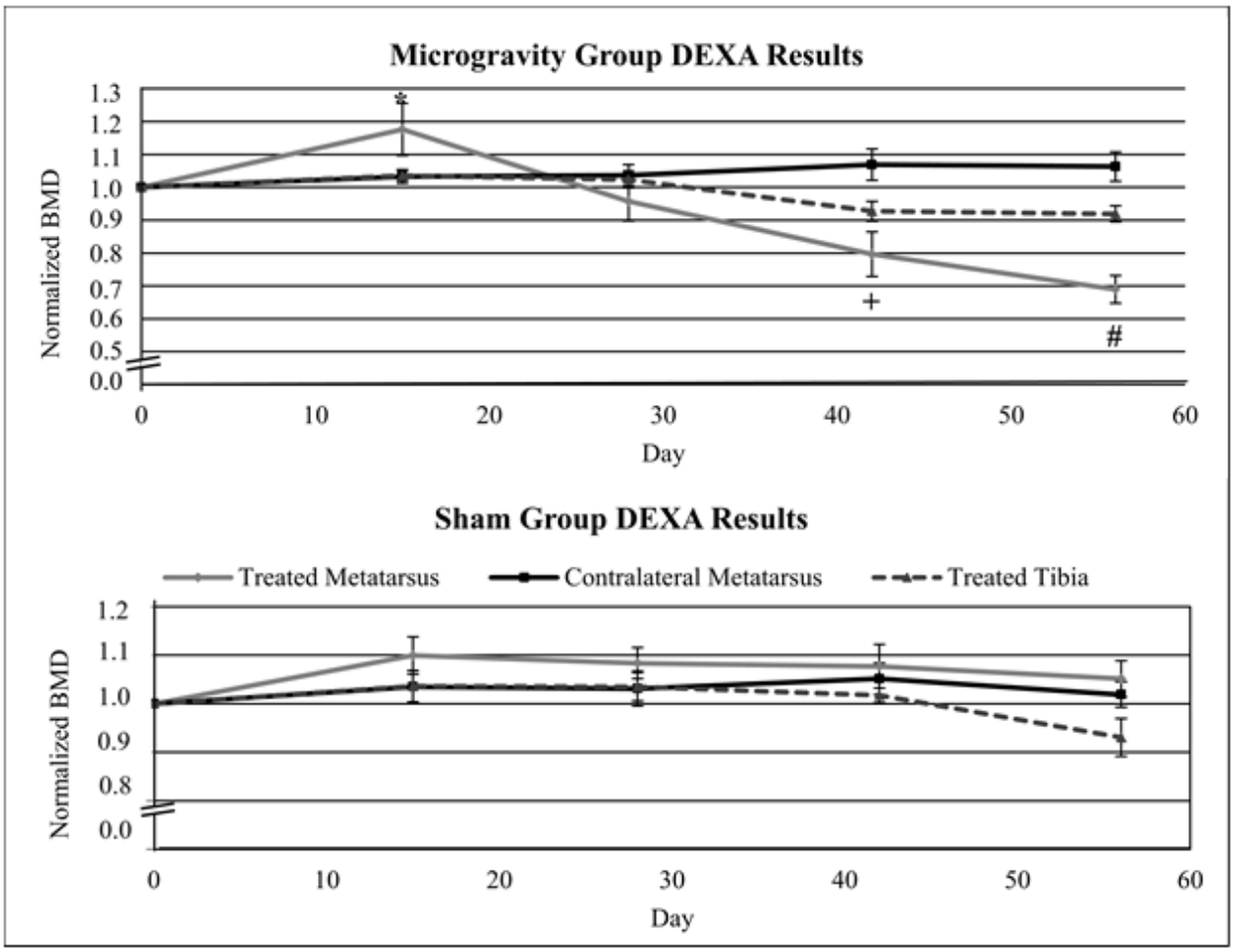

Figure 13. Normalized temporal DEXA results for the (Top) Microgravity and (Bottom) Sham Groups for the 8-week study period. The treated metatarsus displayed an acute rise in BMD after 2 weeks (* $p<0.01$) followed by a rapid, linear decline in BMD due to the microgravity treatment with significant alterations in BMD versus baseline values occurring 6 weeks (+ $p<0.01$) and 8 weeks (# $p<0.001$) post-surgery.

Statistically significant losses in four-point bending modulus were observed between the treatment and contralateral (control) metatarsi of the Microgravity Group (-25.8%, $p<0.05$) as well as between the treatment metatarsi of the Microgravity Group and the contralateral metatarsi of the Sham Group (-26.2%, $p<0.05$, Figure 14). Statistical differences in four-point bending modulus were not observed between limbs of the Sham Group metatarsi. Statistically significant differences in failure load were detected between the treated metatarsi of the

Microgravity Group and all other groups in diametral compression (Figure 14). The Microgravity Group treated metatarsal diaphyseal failure load was 27.8% ($p<0.001$) lower than that of the Microgravity Group contralateral metatarsi, 29.1% ($p<0.01$) lower than that of the Sham Group treated metatarsi, and 32.6% ($p<0.01$) lower than the failure load of the Sham Group contralateral metatarsi.

Alterations in cancellous bone microarchitecture were qualitatively apparent in three-dimensional reconstructions of the μCT ROIs (Figure 15). Statistically significant differences were observed between the treated metatarsi of the Microgravity Group and all other treatment groups for BV/TV, Tb.N, Tb.Th, SMI value, and Tb.BMD (Table 2). Specifically, BV/TV, Tb.N, Tb.Th, and Tb.BMD decreased 38.3% ($p<0.001$), 22.5% ($p<0.05$), 30.9% ($p<0.01$), 39.3% ($p<0.01$), respectively, as compared to their contralateral metatarsi. The SMI parameter increased 89.3% ($p<0.001$) in the Microgravity Group treated metatarsi as compared to their contralateral controls. No statistically significant differences were observed within the Sham Group for any measured outcome parameter.

Histomorphometry revealed statistically significant reductions in BV/TV, BFR, N.Ob, and N.Oc for the Microgravity Group treatment metatarsi versus all other groups (Table 2). BV/TV, BFR, and N.Ob were reduced 44.7% ($p<0.001$), 57.7% ($p<0.01$), and 51.5% ($p<0.001$), respectively, while N.Oc increased 269.1% ($p<0.001$) in the treated metatarsi as compared to their contralateral controls following simulated microgravity treatment. Standard and dynamic histomorphometric measures for the Sham Group did not display significant differences between the operated and contralateral metatarsi.

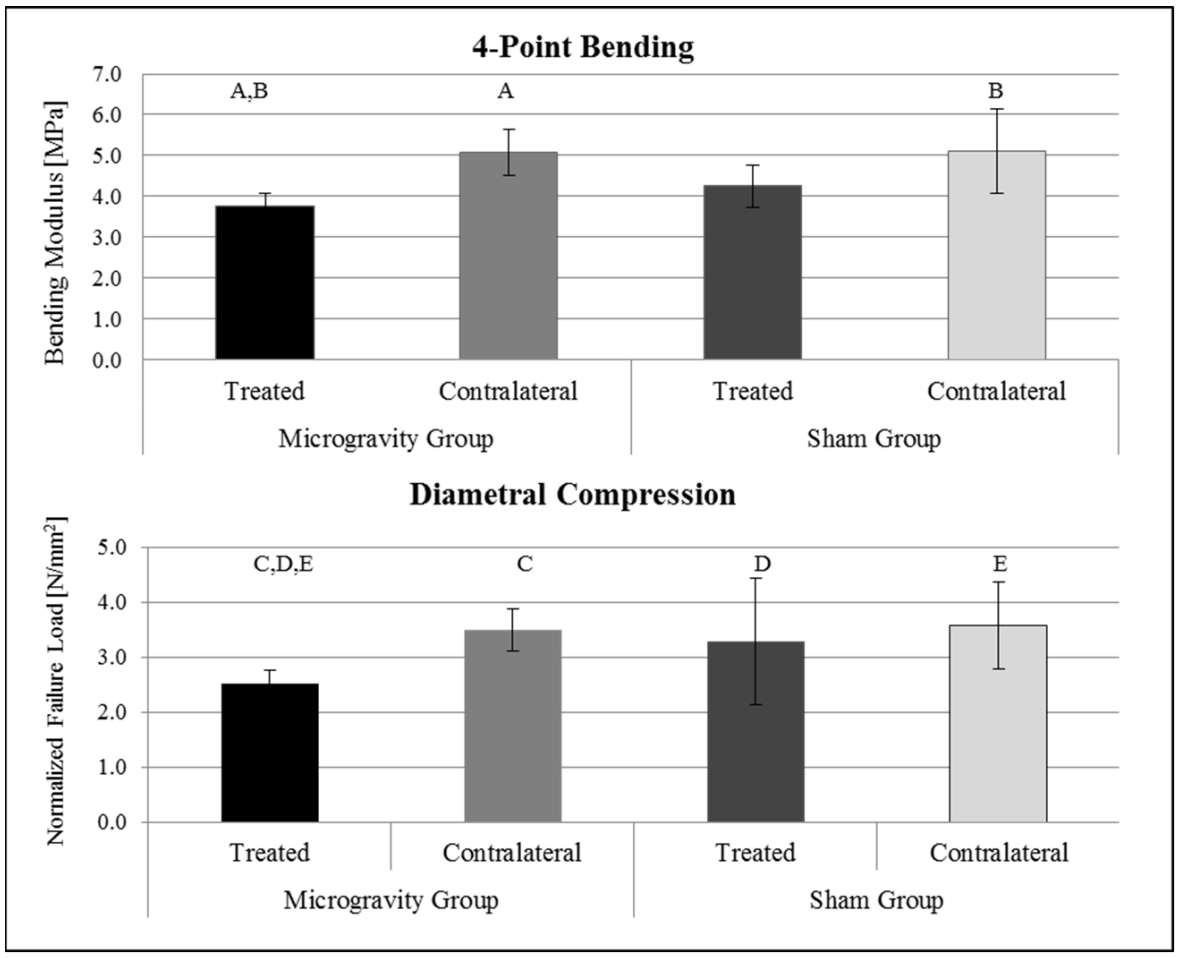

Figure 14. (Top) Four-point bending modulus decreased as a result of Microgravity unloading. Groups denoted by like-letters are statistically different from each other: (A) $p<0.05$; (B) $p<0.05$. (Bottom) Normalized diametral compression failure decreased following the Microgravity treatment while no changes were evident following the Sham treatment: (C) $p<0.001$; (D) $p<0.01$; (E) $p<0.01$.

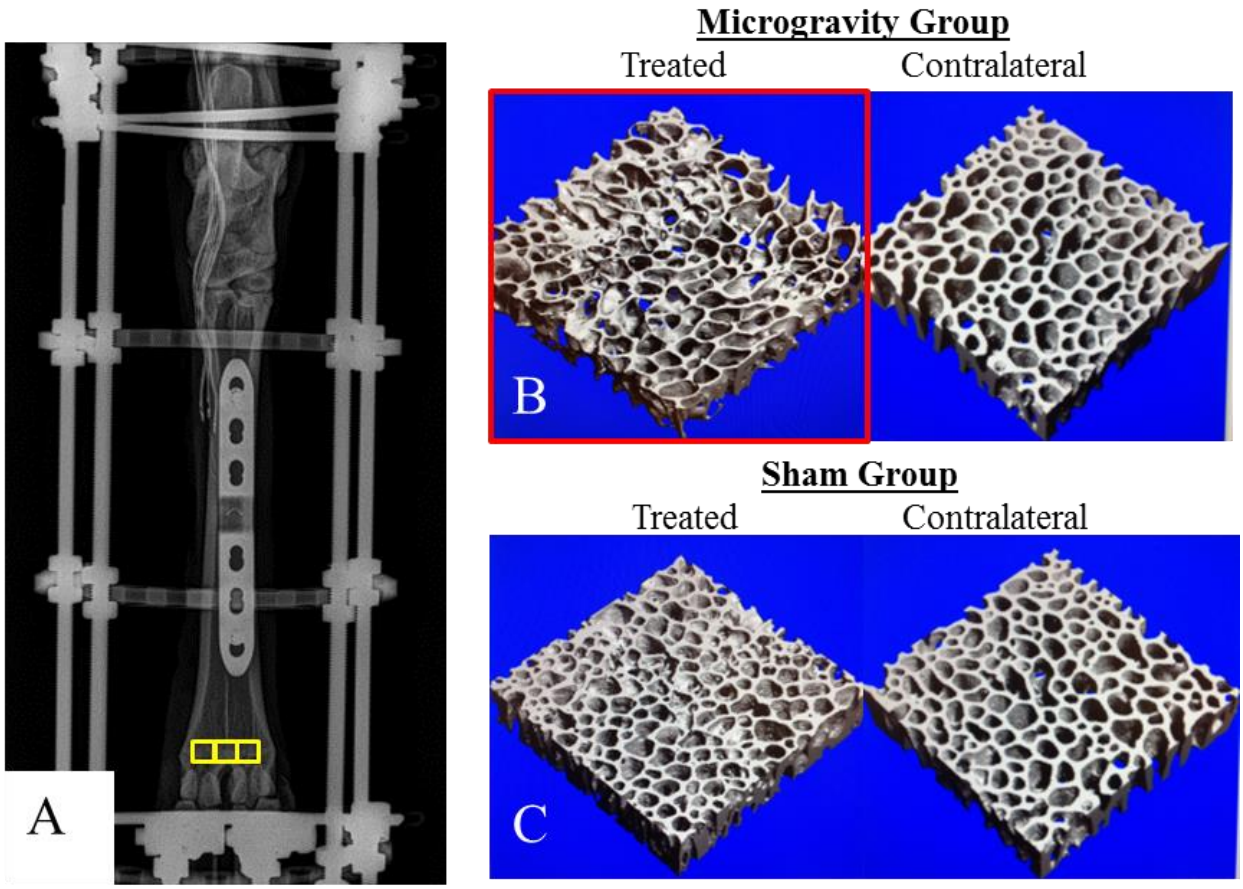

Figure 15. (A, highlighted) DEXA, µCT, and static histormorphometric analyses were performed in the distal cancellous network of the metatarsus. Three-dimensional µCT reconstructions demonstrate decreased trabecular number, thickness, and bone volume within the cancellous microarchitecture in the (B) Microgravity Group treatment metatarsi (highlighted) versus their contralateral (control) metatarsi and those of the (C) Sham Group.

Table 2. Mean (with one standard deviation) µCT and histomorphometric bone parameters of the distal metaphyseal regions of the Microgravity and Sham Groups. The majority of µCT and histomorphometric parameters demonstrated statistically significant ($p<0.05$) differences between the Microgravity Treatment Group versus the Microgravity Contralateral, Sham Treatment, and Sham Contralateral Groups. Those parameters that did not display statistical significance between groups ($p>0.05$) are denoted (*).

		Microgravity Group		**Sham Group**	
		Treated	Contralateral	Treated	Contralateral
µCT	BV/TV [%]	0.26 (0.07)	0.41 (0.06)	0.42 (0.06)	0.44 (0.06)
	Tb.N [1/mm]	2.01 (0.26)	2.59 (0.43)	2.51 (0.04)	2.56 (0.14)
	Tb.Th [mm]	0.13 (0.02)	0.19 (0.02)	0.21 (0.04)	0.22 (0.04)
	Tb.Sp [mm]*	0.53 (0.07)	0.44 (0.05)	0.41 (0.10)	0.45 (0.02)
	H2 [mm]*	0.70 (0.25)	0.67 (0.13)	0.64 (0.04)	0.63 (0.26)
	SMI	-0.13 (0.48)	-1.71 (0.65)	-1.36 (1.46)	-2.01 (0.98)
	Tb.BMD [mg/ccm]	218.48 (52.22)	359.33 (44.84)	396.56 (95.345)	373.10 (110.55)
	C.BMD [mg/ccm]*	997.13 (42.83)	1030.57 (46.13)	1048.57 (69.12)	1044.76 (70.52)
Histomorphometry	BV/TV [%]	0.21 (0.06)	0.38 (0.05)	0.37 (0.06)	0.41 (0.04)
	B.Dm [mm]*	13.22 (0.61)	12.77 (0.61)	13.04 (1.01)	12.84 (0.97)
	Ct.Wi [mm]*	2.81 (0.36)	2.68 (0.22)	2.78 (0.11)	2.69 (0.34)
	MS/BS [%]*	0.21 (0.08)	0.35 (0.11)	0.36 (0.09)	0.36 (0.07)
	MAR [µm/day]	1.09 (0.13)	1.45 (0.25)	1.42 (0.09)	1.47 (0.25)
	BFR [µm/day]	0.22 (0.11)	0.52 (0.19)	0.50 (0.11)	0.55 (0.20)
	Ob.N/BS [mm^{-1}]	11.71 (1.12)	24.47 (3.69)	18.72 (4.58)	18.73 (4.50)
	Oc.N/BS [mm^{-1}]	3.57 (1.46)	0.97 (0.10)	0.99 (0.46)	0.54 (0.24)

Discussion

A ground-based large-animal model of simulated microgravity was developed using common external fixation instrumentation that replicates the physiologic alterations associated with weightlessness. The external fixation parametric study results demonstrate that significant alterations in the local tissue mechanics can be imparted on the metatarsal bone by simply adjusting the stabilizing rod and fixation pin configurations, allowing specific planetary and celestial microgravities such as those of Mars (0.38g) and the Moon (0.16g) to be simulated. Further, the *in vivo* strain analysis corroborated these findings and demonstrated that the desired metatarsal unloading could be sustained over the course of the study.

The linear temporal loss of BMD in the treated metatarsi in the current study measured via DEXA is in agreement with previous studies that also measured rapid, linear losses in BMD following unloading due to spinal cord injury (51). The lack of significant alterations in BMD in the ipsilateral tibia and isolated losses in BMD in the treated metatarsus provides strong evidence that bone density loss was not driven by an overall limb disuse, but rather by an unloading mechanism. The maintenance of baseline values within the contralateral metatarsi further indicate that changes in weight bearing were not responsible for the observed BMD losses in the treated metatarsi, as an increase in contralateral limb loading would have resulted in increased BMD. Additionally, it has been reported that inflammatory disorders are often accompanied by bone loss (55), however, the sustained BMD values of the Sham Group suggest that density alterations were independent of the surgical technique, the application of fixation pins, and any associated inflammatory effects.

When compared to human spaceflight, the rate of bone loss experienced in the current study was relatively rapid, allowing the simulation of long-duration space travel in a relatively concise period of time. For example, the bone loss associated with a space mission to Mars, which will require approximately one year of spaceflight (or more), is expected to be upwards of 25% in weight-bearing limbs given extrapolation of known BMD loss rates, and may be simulated in approximately two months with the current ovine simulated microgravity model (148).

The current microgravity treatment was accompanied by declines in mechanical strength of the metatarsal diaphysis as evidenced by non-destructive (four-point bending) and destructive (diametral compression) biomechanical evaluations. μCT analyses revealed slight declines in diaphyseal cortical BMD. While these alterations were non-significant ($p=0.22$), it has been demonstrated that a slight 4% reduction in cortical BMD can result in a 13% reduction in ultimate stress and a 25% reduction in elastic modulus (104). These data indicate that even modest reductions in cortical BMD may result in substantial alterations in mechanical properties. The current study demonstrated cortical BMD losses of 3-5% in the treated metatarsal diaphysis following the microgravity treatment versus the other treatment groups, resulting in reductions in elastic modulus and failure load of 25-26% and 28-33%, respectively, further supporting previous findings (104).

The reported outcome parameters of the current study are in general agreement with previous HU and spaceflight studies utilizing rodents. Losses in overall BMD of 21% per month, as well as decreases in BV/TV, Tb.Th, and Tb.N of 31%, 23% and 23%, respectively, in HU rodents have been reported (12, 14). Similarly, the alterations in bone formation parameters in the

current study are characteristic of previously reported rodent studies. Declines in MS between 50% and 70% in mature female rats as well as reductions in MAR and BFR between 30% and 90% have been reported in mature male rats, similar to the 40%, 25%, and 57% reductions in MS, MAR, and BRF, respectively, reported in the current study (3, 12, 35, 91).

At the cellular level, reduced osteoblast activity has been identified as a major underlying mechanism of bone remodeling in rodent HU and spaceflight studies, while subtle or no changes in osteoclast activity are commonly reported (11, 12, 35, 91). Contradictory findings have been reported for human spaceflight in which elevated blood serum markers such as C-telopeptide (CTX), N-telopeptide (NTX), and pyridinium cross-links have provided evidence that the primary mechanism of mineralized tissue adaption to mechanical unloading is through increased osteoclast recruitment (31, 51, 105, 128, 133, 146). The external fixation unloading technique utilized in this model effectively simulated these mechanisms of osteoclastic stimulation and alterations in bone turnover parameters associated with human spaceflight. These data further demonstrate that, although previous ground-based microgravity models utilizing rodents have been able to adequately reproduce the characteristic physiologic alterations associated with mechanical unloading at the larger length scales (i.e. microarchitecture, biomechanics, etc.), the inherent differences between species produce discrepancies between models at the smaller length scales (i.e. cellular responses and molecular cascades). This last point is an important one because the data in this study have identified that, in the presence of simulated microgravity the primary physiologic mechanism behind bone remodeling of rodents and humans/sheep is fundamentally different, making the direct translation of results from small-animal models intractable.

The current model holds some inherent limitations. First, it is possible that metatarsal bone strain and strain-measurement plate readings did not remain linear and/or consistent over the course of the study. Additionally, the limited attachment area in some regions of the hindlimb for the external fixation instrumentation makes achieving zero gravity difficult, and, while the aim of the external fixation device was to limit the amount of compressive force transmitted through the bone, it is possible that the application of the external fixation frame modified the metatarsal stress state due to axial and shear stress coupling. Further, the localized nature of the unloading technique utilized in this model prevents the investigation of systemic factors involved in bone remodeling during mechanical unloading. Finally, while sheep hold certain microstructural and healing advantages over rodents for orthopaedic investigations, the relative cost and ease of implementation of ovine studies is certainly greater than that of rodents.

To conclude, the data reported herein provide strong evidence that the external fixation unloading technique utilized in this model is able to induce mechanical unloading of the metatarsus and significant alterations in the relevant radiographical, biomechanical, and histomorphometric parameters characteristic of spaceflight. Further, these findings demonstrate that the physiologic mechanisms driving bone remodeling in sheep and humans during decreased loading are more similar than previously utilized models, allowing more comprehensive investigations of microgravity-related bone remodeling as it relates to human spaceflight. The similarities between the current model and the human condition will allow future investigations in the areas of fracture healing and possible countermeasures as they relate to microgravity.

CHAPTER 3:

PARTIAL GRAVITY UNLOADING INHIBITS BONE HEALING RESPONSES IN A LARGE ANIMAL MODEL

Introduction

It is well-known that microgravity and the associated inherent reduction in mechanical loading result in substantial loss of BMD and mechanical strength. These issues are particularly important when considering fracture risk during long-duration spaceflight missions. Specifically, the mean rate of BMD loss (in lower body bones) during spaceflight has been shown to be dramatically higher than experienced on Earth, averaging losses of 1%-3% per month (76, 148). Accordingly, simulations of alterations in mineralized tissue properties as a result of microgravity loading have predicted significantly elevated risk of fracture during long-duration (i.e. Mars) missions (77, 100).

[2]This chapter has been published as a Research Article in the Journal of Biomechanics (47, 12 (2014)). The text and figures have been adapted with permission from the journal's publisher, Elsevier.

What is not as well-understood is how the mechanical unloading associated with spaceflight affects the fracture healing cascade. Fracture healing is a complex biological process with four distinct phases. The first step of the fracture healing cascade, occurring at the time of fracture, is the formation of a hematoma, preventing further blood accumulation at the fracture site (73). Subsequently, a soft callus forms as chondrocytes create new cartilage that bridges the two ends of the disjoined bone, providing initial mechanical competency (i.e. splinting) to the fracture (42). Finally, osteoblasts replace the new cartilage with woven bone, which in turn is remodeled into a compact secondary osteonal bone structure (125). It has been postulated that this reparative process represents a recapitulation of development that involves complex mechanical and chemical factors (44, 45). Further, it has been shown that the mechanical loading environment of the healing callus has a profound effect on the resultant cell differentiation and heterogeneous matrix phenotypes ("mechanobiology") (26, 78, 92, 141). *In vivo* experiments using fracture models have elucidated certain cellular and molecular scale events that are important in the repair process. However, alterations in the local mechanics induced via reduced gravitational loading in the repair process have not been rigorously described in bone tissues that have Haversian systems. Nonetheless, it is clear that the mechanical environment, which transcends many length scales (from whole body to the subcellular), plays a key role in the subsequent fracture healing pathway and, ultimately, the nature and quality of the osseous repair. This certainly has significant implications when examining how microgravity, which impacts the relevant mechanical environment on all of these length scales, may affect bone healing.

Limited research has been performed to investigate mineralized tissue healing in microgravity environments (5, 40, 69, 72). Rodent studies have elucidated distinct histological and morphometric differences in animals that heal in gravitational environments versus animals that heal during spaceflight. Using a rat model, Kirchin et al. showed that bone healing was altered during spaceflight, resulting in suppression of chondrogenesis within the periosteal reaction and angiogenesis within the osteotomy gap (72). Additionally, Durnova et al. reported decreased fracture callus size and consolidation strength resulting from inhibited osteoblast activity in rodents during a 14-day spaceflight experiment (40). While these data demonstrate that microgravity has a deleterious effect on bone healing, the direct translation of these results to human bone healing is intractable due to the numerous differences between rodent and human bone microstructure and healing. Specifically, the basic microstructure of rodent bone can be observed as a primary lamellar structure lacking the osteonal (Haversian) systems characteristic of human bone (41, 108). Further, it has been shown that the rate of bone healing is known to be inversely related to the species' ranking on the phylogenetic scale (37). Consequently, the healing potential of rodent bone far exceeds that of adult human tissue (37, 89). Due to these distinct differences between species and the limited information regarding fracture healing in Haversian systems, the objective of this study was to investigate the effects of partial gravitational unloading on long-bone fracture healing in a previously-developed large animal model using parameters derived from biomechanical, histomorphometric, and radiographic assessments.

Methods

Ten skeletally mature Rambouillet Columbian ewes (age > 6 years) were used in this study. Animal use approval was granted by the Colorado State University Animal Care and Use Committee (Approval #11-2938A). Hindlimb metatarsal unloading was accomplished using the technique described by Gadomski et al (48). Briefly, a trans-biarticular external skeletal fixation device (IMEX, Longview, TX) was implanted on the right hindlimb of 5 skeletally mature female ewes such that the metatarsal bone was partially isolated from mechanical loading (PU Group, Figure 16). Previous *in vivo* experiments demonstrated that this external fixation unloading system was able to reduce metatarsal bone loading by 75% (a relative gravity environment of 0.25g; Gadomski, 2014). The animals of the PU Group were exposed to partial unloading of the metatarsal bone via external fixation for a period of 3 weeks (21 days). An ostectomy procedure was performed at the 3-week time point by removing a 3.0mm section of bone from the mid-diaphysis of the metatarsus. The ostectomy was stabilized via a laterally-attached orthopaedic locking plate (Synthes, Inc., Westchester, PA) instrumented with a rosette strain gage (Vishay Precision Group, Malvern, PA). This fracture method was deemed most appropriate for this study due to its high level of repeatability (i.e. measurability) and its ability to allow investigation of the healing cascade inside of the fracture gap. Additionally, this model allowed for the interrogation of the healing response of the body following an orthopaedic surgical procedure in a partially unloaded environment, which will be clinically relevant in the future as spaceflight duration increases.

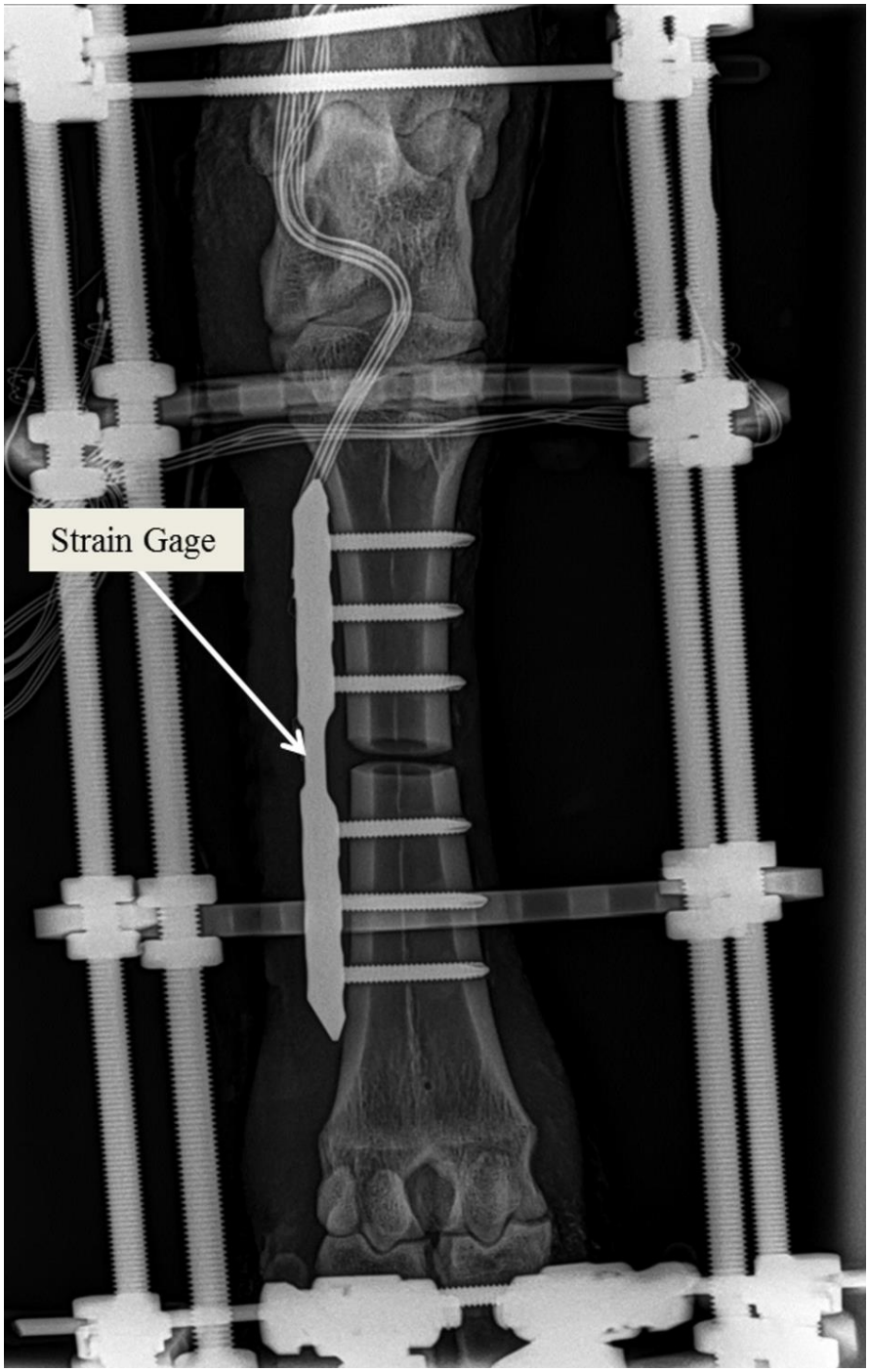

Figure 16. A mid-metatarsal ostectomy was created and stabilized with an orthopaedic locking plate instrumented with a rosette strain gage in order to monitor *in vivo* fracture healing and mechanical competence.

An additional full loadbearing Earth gravity group (FL Group, n=5) was included in which an identical 3.0mm ostectomy was created, plated, and secured via a fiberglass cast from the proximal tibia to the phalanges, allowing full loading to be transmitted through the metatarsal bone. Following the ostectomy procedure, both groups were subjected to a 4-week (28-day) healing period.

In Vivo Testing

Dual-energy x-ray absorptiometry (DEXA) scans (Discovery A, Hologic, Inc., Bedford, MA) were performed on the treated metatarsi of the PU Group at the time of the external fixation surgery, the ostectomy surgery, and every two weeks until sacrifice to obtain a clinical measure of BMD. DEXA scans were performed on the FL Group at the time of the ostectomy surgery and every two weeks until sacrifice. Longitudinal BMD values were normalized to the baseline BMD value for each animal for comparisons between groups (48).

In vivo mechanical competency of the healing fracture was evaluated bi-weekly via strain measurements of the orthopaedic plate by testing each animal on a force sensing platform. Strain measurements from the metatarsal plate for single-limb ground reaction forces up to 200N were recorded for the standing animals. The strains measured in the orthopaedic plates were correlated to ground reaction forces between 50N and 200N, and the resultant construct stiffness slope magnitude ($\mu\varepsilon$/N) per testing day was calculated and normalized to the peak magnitude to characterize the change in load burden for each group over the course of the study. Utilizing the experimentally measured strains of the orthopaedic fixation plate, and assuming that the longitudinal strains of the fracture site and fixation plate were equivalent, simplified linear elastic

constitutive relationships were utilized to calculate the resultant stresses (Equation 4) and forces (Equation 5) acting on the fixation plate and fracture callus.

$$\sigma = E * \varepsilon \quad \text{(Equation 4)}$$

$$F = \sigma * A \quad \text{(Equation 5)}$$

The callus modulus of rigidity (a combined term consisting of elastic modulus (E) multiplied by cross-sectional area (A), EA) was calculated using the previously determined callus stresses. Additionally, weekly radiographs were taken to monitor the bone-pin interface of each animal. Fluorochrome labels were administered 21 and 7 days (calcein green at 20 mg/kg, Sigma-Aldrich Co., LLC, St. Louis, MO) prior to sacrifice.

Biomechanical Evaluation

Following sacrifice, biomechanical evaluations were performed on the treated metatarsi of the PU and FL Groups. Non-destructive four-point bending experiments were performed on whole, dissected metatarsal bones using a custom-made four-point bending fixture coupled to a servohydraulic testing machine (MTS Systems Corporation, Eden Prairie, MN). The test frame's actuator was lowered at a rate of 1.0mm/sec to 200N or to the specimen's maximum deflection prior to inducing damage (i.e. a sharp, observable decrease in the monotonically increasing force profile) (39). The sample was preconditioned 5 times to the previously determined load and the load-displacement data from the final cycle were utilized to calculate the specimen bending stiffness.

Micro-Computed Tomography

Post-sacrifice micro-computed tomography (μCT) analyses were performed at the mid-diaphyseal fracture of the treated metatarsi from the PU and FL Groups using the following parameters: voltage: 70kVp, current: 114μA, integration time: 500ms (Scanco μCT 80, Scanco Medical AG, Bruttisellen, Switzerland). A 1.5mm thick region of interest (ROI) was created within the fracture gap and centered between the superior and inferior bone surfaces, and bone volume fraction (BV/TV, %) as well as BMD (mg HA/cm^3) were quantified for each specimen. Additionally, the periosteal fracture callus was segmented between the inner-most screw holes of the metatarsal diaphysis (23.0mm length) to include all external callus while excluding diaphyseal bone, and total bone volume (mm^3) as well as BMD (mg HA/cm^3) were quantified for each specimen.

Histomorphometric Analysis

Following μCT analysis, the treated metatarsi were processed for decalcified and undecalcified histological analyses. Histological sections were taken in the transverse (mediolateral) plane to include the fracture site and associated callus of the diaphyseal region of the metatarsus. Two undecalcified sections from each specimen were stained with Sanderson's Rapid Bone Stain and counter-stained with Van Gieson, while the other two sections were left unstained for dynamic histomorphometric analysis. Two 8 micron decalcified sections from each specimen were cut on a Leica RM2255 rotary microtome (Leica Microsystems, Inc., Nussloch, Germany) and stained with Hematoxylin and Eosin.

For static histomorphometric analysis, high resolution digital images (at 10x magnification) were acquired. Fracture gap height as well as area fractions of mineralized and fibrocartilagenous tissue were calculated in the periosteal callus, diaphyseal cortices, and intramedullary canal (Figure 17).

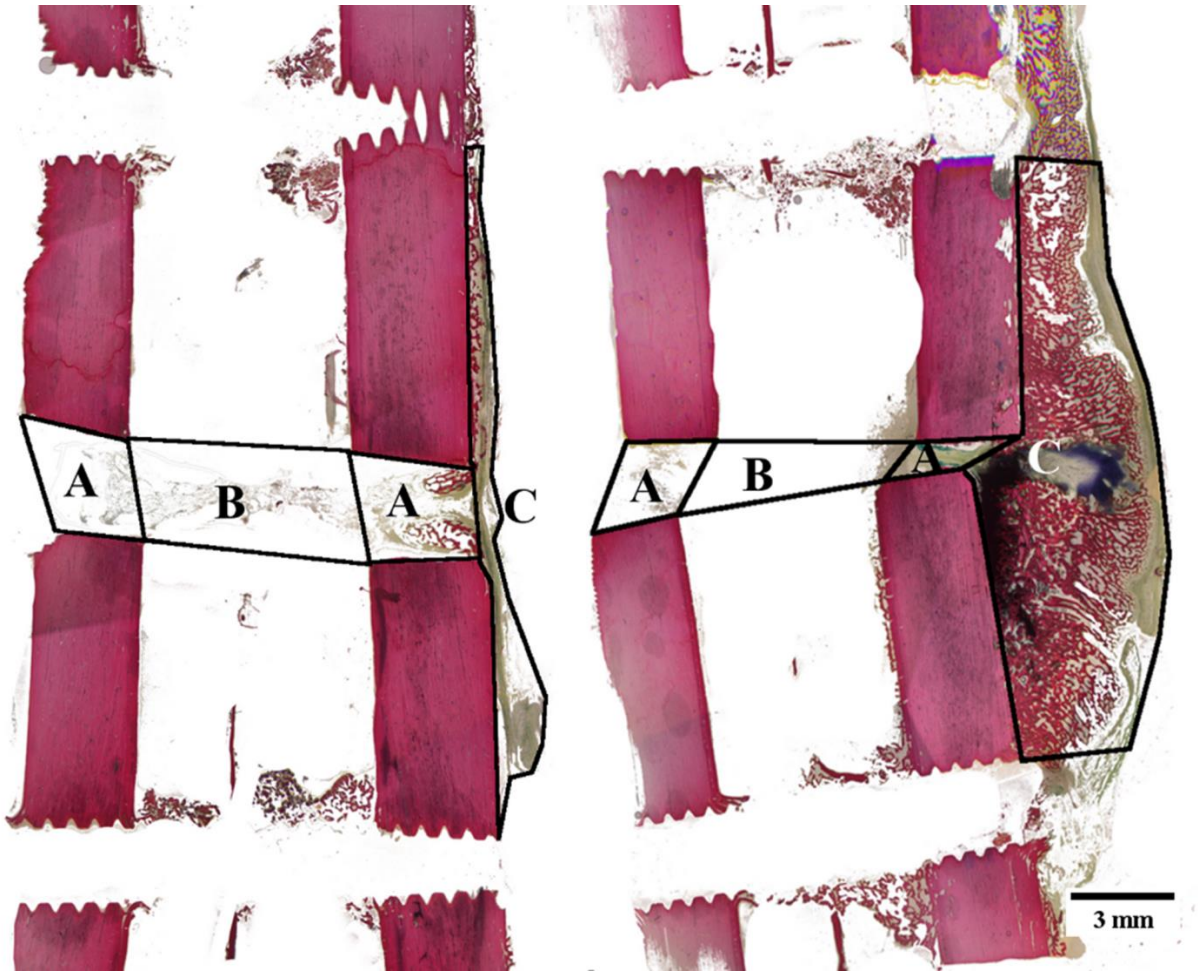

Figure 17. Representative histology images demonstrate significantly reduced periosteal callus (Region C) formation in the (left) PU Group as compared to (right) FL Group specimens. Sections were stained with Sanderson's Rapid Bone Stain and counter-stained with Van Gieson. Bone and fibrous tissue area fractions (%) were calculated for (A) cortex, (B) intramedullary canal, and (C) periosteal callus ROIs.

Segmentation was performed semi-automatically via pixel intensity using Image Pro (Media Cybernetics, Silver Spring, MD). Total periosteal callus bone and fibrocartilage area (mm^2) were determined by selecting and segmenting callus material contralateral to the orthopaedic plate on the exterior surface of the bone within 11.5mm of the fracture centrum. Bone and fibrocartilage area fractions were calculated within the periosteal callus, diaphyseal cortex, and intramedullary canal. In order to account for inter-specimen variations in fracture site geometry, the ratio of segmented tissue area to the total area of the respective ROI was calculated. Diaphyseal cortex bone and fibrocartilage fractional area (%) were selected within the mediolateral confines of the diaphyseal cortical shell and craniocaudal edges of the fracture gap and calculated by taking the ratio of respective tissue area within the ROI to total ROI area. Intramedullary canal bone and fibrocartilage fractions (%) were similarly determined by segmenting the images within the confines of the intramedullary canal and within the boundaries of the cranial and caudal fracture gap edges. For dynamic histomorphometry, three fluorescent images were acquired per specimen (at 40x magnification) within the periosteal callus and mineralizing surface (MS), mineral apposition rate (MAR), and bone formation rate (BFR) were calculated (48). Analyses were not performed on the endosteal surface due to the consistent absence of endosteal bone formation. Decalcified cellular histomorphometry was performed on digital images (at 200x magnification) for three ROIs within the periosteal callus and on the endosteal surface per specimen to determine osteoblast (Ob.N) and osteoclast (Oc.N) number.

Statistical Analysis

Statistical analyses were performed using standard Student's t-tests for comparisons between groups or a repeated measures one-way analysis of variance (ANOVA) for longitudinal DEXA

and strain comparisons within groups with Student-Newman-Keuls *post-hoc* tests (α=0.05). In the event that data were not normally-distributed, a Mann-Whitney U test was performed (SigmaPlot, Systat Software, Inc., San Jose, CA).

Results

All data are presented as the mean ($\pm$ standard deviation).

In Vivo Testing

In vivo DEXA scans demonstrated a statistically significant (p=0.002) loss of BMD in the treated metatarsal bone of the PU Group following the initial 3-week unloading period (Day 0 - Day 21, 0.63 ± 0.15 – 0.50 ± 0.13 g/cm^2, respectively), resulting in a mean net loss of 17.6% at the time of the ostectomy surgery (Figure 18).

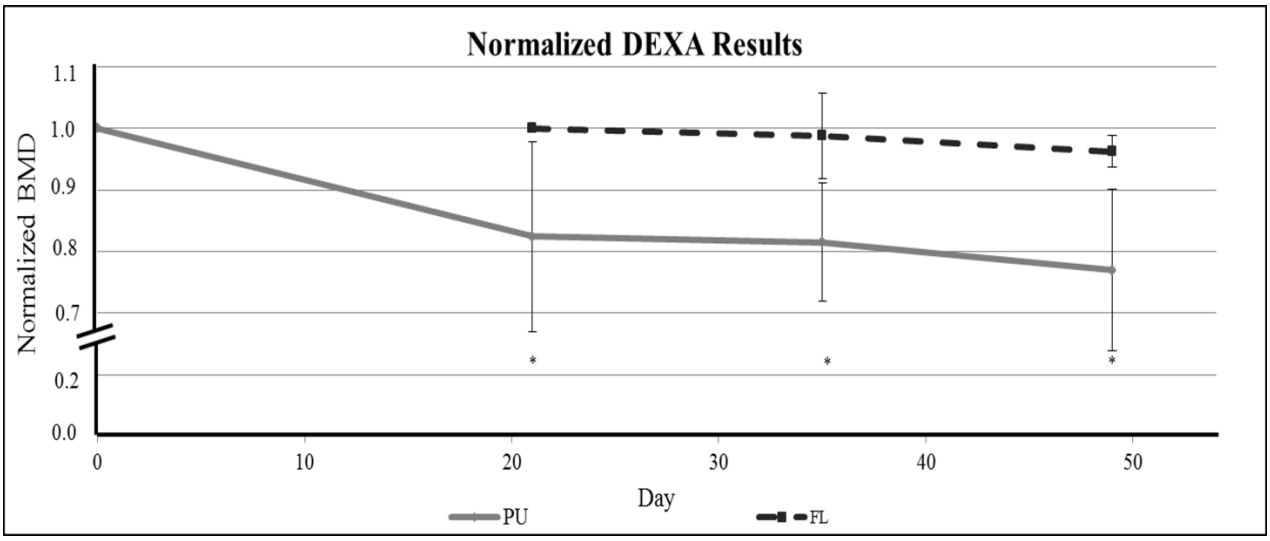

Figure 18. Normalized temporal DEXA results for the PU and FL Groups. The treated metatarsus of the PU Group demonstrated statistically significant reductions in BMD versus baseline (Day 0) values at the 21, 35, and 49-Day timepoints following the application of the external fixation device (* p<0.001). No statistically significant alterations were detected in the FL Group.

The rate of BMD loss of the PU Group was reduced following the ostectomy surgery, resulting in an additional average loss of 5.4% between the time of the ostectomy surgery and sacrifice (Day 21 - Day 49, 0.50 ± 0.13 – 0.43 ± 0.15 g/cm^2, respectively). No statistically significant alterations in BMD occurred in the treated metatarsus of the FL Group (Day 21 – Day 49, 0.63 ± 0.04 – 0.61 ± 0.03 g/cm^2, respectively).

The PU Group displayed limited reduction in orthopaedic plate construct stiffness during the course of the 28-day fracture healing period as compared to the FL Group (Figure 19).

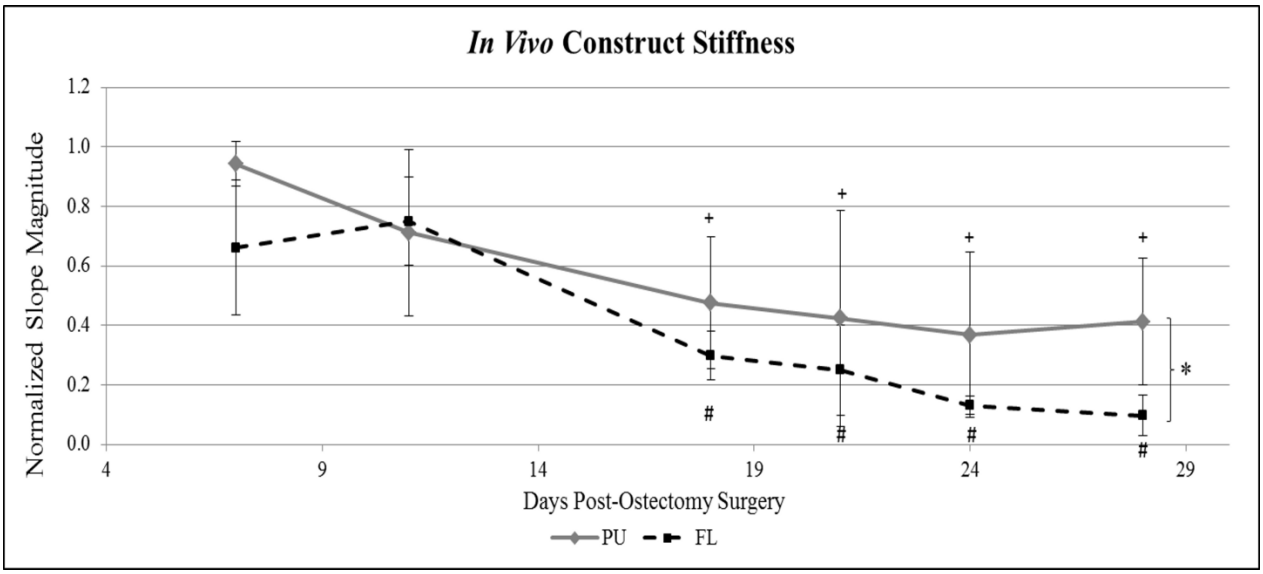

Figure 19. *In vivo* measurements demonstrated decreased construct stiffness with healing (slope magnitude) of the orthopaedic fixation plates in both the PU (* $p<0.01$) and FL (# $p<0.001$) Groups versus baseline values (Day 7) beginning at Day 18 and continuing through the remainder of the study. The PU Group demonstrated reduced mechanical competency at the fracture site as compared to the FL Group as evidenced by a higher slope magnitude of the orthopaedic plate in the FL Group at the conclusion of the healing period (* $p<0.05$).

The PU Group experienced a 49.6% decrease in slope magnitude between day 7 and day 18 of the 28-day healing period ($p<0.01$); however, the subsequent 5.5% decrease in slope magnitude that occurred during the final 10 days of healing demonstrates that the rate of healing was attenuated. A greater level of healing was experienced by the FL Group, with a net reduction in orthopaedic plate construct stiffness magnitude of 573.0% between day 7 and day 28 ($p<0.001$). Further, a statistically significant difference in orthopaedic fixation plate construct stiffness was observed between groups at the completion of the 28-day healing period ($p<0.05$).

Biomechanical Evaluation

Visual inspection of the PU and FL specimens at the time of dissection qualitatively revealed noticeable differences in the level of tissue healing. Reduced callus formation was observed in PU Group specimens as compared to the FL Group specimens, which demonstrated more fully-bridged fracture gaps and substantial callus growth on the periosteal surface around the circumference of the fracture (Figure 20). Results of the 4-point bending test demonstrated statistically significant differences in stiffness between the PU and FL Groups ($p<0.01$), with mean ($\pm$ standard deviation) FL and PU Group four-point bending stiffnesses of 213.3 ($\pm$ 36.3) N/mm and 48.9 ($\pm$ 47.8) N/mm, respectively.

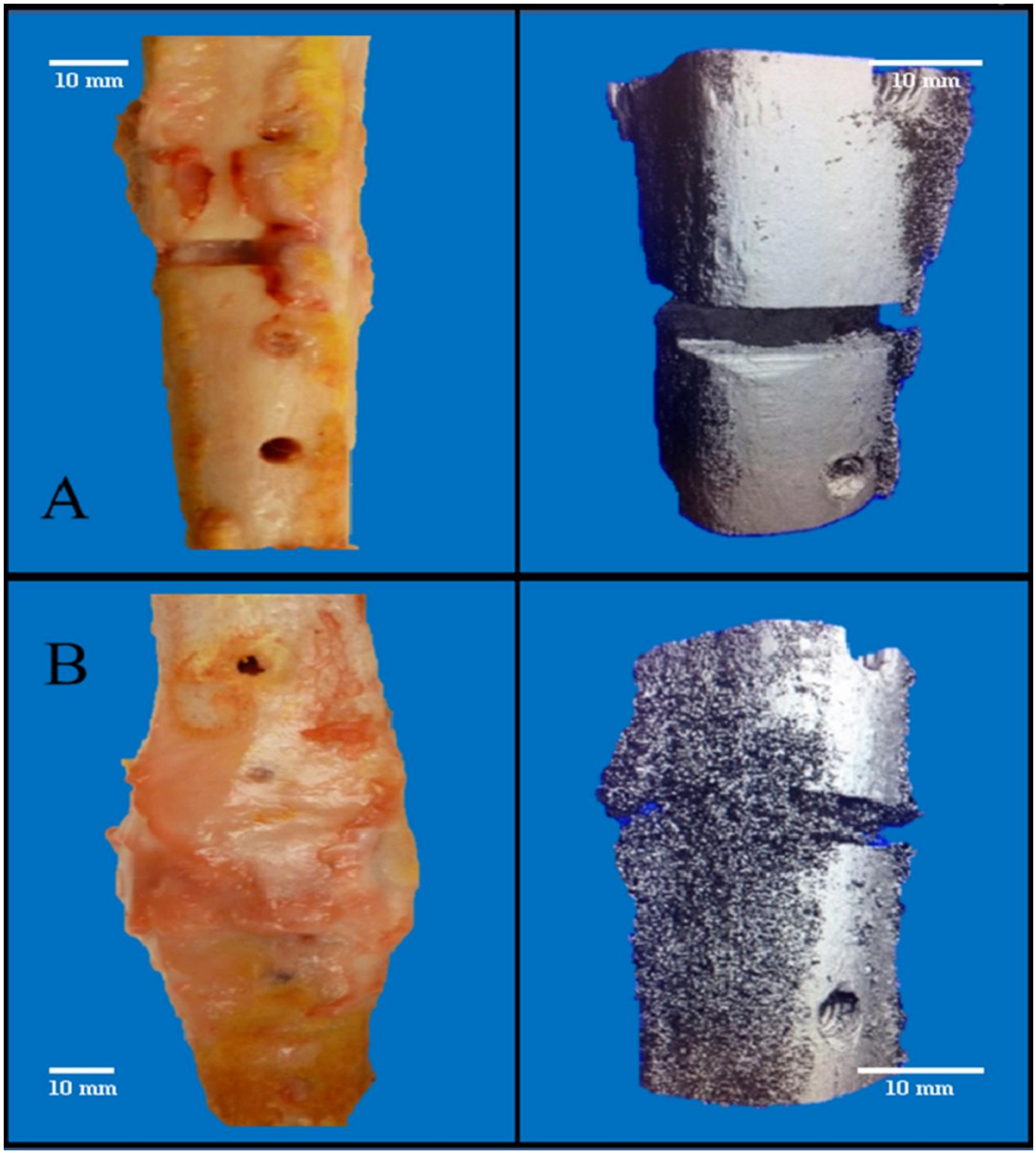

Figure 20. Representative (left) gross necropsy images of the mid-diaphyseal fracture callus and (right) respective μCT three-dimensional reconstructions demonstrated reduced mineralization and callus formation for the (A) PU Group as compared to the (B) FL Group.

Micro-Computed Tomography

Bone volume fraction and BMD within the fracture gap were reduced by 10.4% and 7.8%, respectively, in the PU Group as compared to the FL Group (Table 3). Bone volume within the fracture callus was reduced by nearly 9-fold ($p<0.01$) in the PU Group (71.270 ± 23.261 mm^3) as compared to the FL Group (637.144 ± 177.498 mm^3). No statistically significant differences in callus BMD were measured.

Histomorphometric Analysis

Static histomorphometric analyses revealed no significant difference in fracture gap height at the time of sacrifice between the FL and PU Groups (3.1 ± 0.4 mm and 2.7 ± 1.0 mm, respectively). FL specimens demonstrated greater callus area (19.3 ± 8.3 mm^2) as compared to PU specimens (2.0 ± 1.6 mm^2, $p<0.05$, Table 3). No differences in total mineralized area were observed between groups within the cortical and intramedullary ROIs, nor were significant differences in bone or fibrocartilage area fractions within any ROI between the two groups observed. Mineralizing surface (MS), mineral apposition rate (MAR), and bone formation rate (BFR) were reduced by 21.5% ($p<0.05$), 37.8% ($p<0.001$), and 51.1% ($p<0.001$), respectively, in the PU Group as compared to the FL Group. Decalcified histomorphometric analyses revealed 54.9% ($p<0.001$) and 46.7% ($p<0.01$) reductions in osteoblast numbers between the PU Group and the FL Group on the periosteal and endosteal surfaces, respectively. Additionally, periosteal osteoclast number increased 45.5% ($p<0.05$) following partial unloading. No differences were detected on the endosteal surface.

Table 3. Mean (standard deviation) histomorphometric and micro-CT parameters for the PU and FL Groups. Letter superscripts denote statistically significant differences between groups: (A) $p<0.01$; (B) $p<0.05$; (C) $p<0.05$; (D) $p<0.001$; (E) $p<0.001$; (F) $p<0.001$; (G) $p<0.05$; (H) $p<0.01$.

		PU	FL
µCT	Callus Bone Volume [mm^3]^{A}	71.270 (23.261)	637.144 (177.498)
	Gap Bone Volume Fraction [%]	0.057 (0.045)	0.064 (0.033)
	Callus BMD [$mgHA/cm^{3}$]	783.550 (95.601)	709.817 (71.217)
	Gap BMD [$mgHA/cm^{3}$]	681.403 (19.604)	738.964 (162.825)
Histomorphometry	Callus Area [mm^2]^{B}	2.1 (1.6)	19.3 (8.3)
	Callus Bone Area Fraction [%]	22.3 (15.6)	25.0 (7.5)
	Callus Fibrocartilage Area Fraction [%]	6.0 (4.2)	17.5 (14.1)
	Cortex Bone Area Fraction [%]	5.7 (2.8)	6.1 (4.4)
	Cortex Fibrocartilage Tissue Fraction [%]	14.5 (16.3)	14.4 (4.0)
	Intramedullary Bone Area Fraction [%]	0.3 (0.4)	2.9 (4.1)
	Intramedullary Fibrocartilage Tissue Fraction	0.5 (0.4)	10.4 (9.1)
	Periosteal MS/BS [%]^{C}	0.4 (0.1)	0.5 (0.0)
	Periosteal MAR [µm/day]^{D}	2.8 (0.7)	4.5 (0.3)
	Periosteal BFR [µm/day]^{E}	1.2 (0.4)	2.4 (0.3)
	Periosteal Ob.N/BS [mm^{-1}]^{F}	14.4 (2.0)	26.9 (5.7)
	Periosteal Oc.N/BS [mm^{-1}]^{G}	0.4 (0.3)	0.0 (0.1)
	Endosteal Ob.N/BS [mm^{-1}]^{H}	11.7 (2.4)	25.8 (7.4)
	Endosteal Oc.N/BS [mm^{-1}]	0.7 (0.7)	0.0 (0.0)

Discussion

The 3-week simulated microgravity treatment utilized in this study was performed prior to inducing the ostectomy (i.e. fracture) in order to model the expected loss of BMD encountered by the typical astronaut during a 6-month spaceflight to Mars. There is compelling evidence to indicate that the BMD loss experienced during a Mars mission will significantly alter the mechanical integrity of mineralized tissue and increase the risk of bony fracture (71). Specifically, on average, losses in BMD (in lower body bones) of astronauts occur at a rate of approximately 1-3% per month (76, 148). Extrapolation of these data to 6 months, the expected minimum transit time to Mars, results in anticipated declines in BMD between 6-18%. Based on

previous simulations, concomitant reductions in skeletal strength of as much as 5.0% per month can be expected due to these BMD alterations, producing a heightened risk of fracture during a Mars mission (71). The current study produced a mean 17.6% loss in BMD at the completion of the 3-week partial unloading exposure period, which represents the upper envelope of anticipated mineralized tissue alterations associated with a mission to Mars (76). It is believed that the high level of osteoclast recruitment previously described for this model is responsible for the observed high rate of bone loss (48). It is interesting to note that the rate of BMD loss was attenuated in the PU Group following the ostectomy procedure at the 3-week time point. Previous investigations utilizing this model have shown metatarsal BMD to decrease linearly for at least 8 weeks (48). Taken together, the results seem to indicate that the creation of the ostectomy may have induced an important systemic reaction in which mineralized tissue resorption in the bone compartments remote to the fracture site was attenuated in order to facilitate fracture healing.

Over the course of the healing period, i*n vivo* strain measurements indicated increased callus strength under Earth gravitational loading as compared to the 0.25g loading experienced by the PU Group. The results of the strain analyses demonstrated that the increase in callus strength under Earth gravitational loading conditions was due to an increase in callus cross-sectional area, elastic modulus, or a combination of these two parameters and corroborate the data generated by the μCT and histomorphometric analyses. Further, changes in construct stiffness slope magnitude of the PU Group were attenuated during the final week of the study, indicating that the majority of callus mechanical strength was established during the early stages of the healing process. This phenomenon was not evident in the FL Group where a continuous, linear decrease in construct stiffness slope magnitude was observed over the final three weeks of the study.

These *in vivo* measurements of callus mechanical strength were further reflected in the post-sacrifice 4-point bending experiments, with the FL Group specimens demonstrating significantly greater bending stiffness. Given these findings, it is evident that the rate of fracture repair is greatly reduced under partial unloading conditions with respect to full Earth gravitational loading.

Histomorhpometric measurements demonstrated no significant difference in fracture gap height between the two groups at the time of sacrifice. This is an important point because it would be anticipated that smaller fracture gap height would lead to an increased rate of fracture healing whereas larger gap sizes would diminish healing rates. The histomorphometric and μCT analyses further supported the results of the *in vivo* strain analysis in which it was revealed that diminished callus area is associated with decreased loading during the healing period. However, no significant differences in mineralized or fibrous tissue area fraction for either group were measured. It appears that the ratio in which the two tissue types were formed was unaltered between the treatment groups while the rate of tissue formation was reduced by the partial unloading environment. These data indicate that the underlying mechanism driving the observed alterations in tissue healing was largely a decrease in the rate of osteoblast cell recruitment/differentiation and resultant mineralized tissue apposition combined with, to a lesser degree, increased osteoclast activity. Additionally, no differences in BMD were detected in the mineralized tissue of the periosteal callus or within the fracture gap between treatment groups, indicating that the quantity, not the quality, of the mineralized tissue formed during the repair process was responsible for determining the resultant callus strength. Previous work has shown BMD of native cortical bone following 8 weeks of mechanical unloading in sheep to be upwards

of 1000 mg HA/cm^3 (48). Based on these data, it can be seen that the BMD of the early-stage callus of this study had not yet reached that of the native cortical bone. It is not yet known what the baseline BMD of native cortical bone is following prolonged exposure to unloading. It is possible that following prolonged unloading the native cortical bone BMD could decrease to the levels seen in this work and that the mineralizing callus had formed at the appropriate physiologic baseline for the amount of unloading induced by the current model.

It has been suggested that the mechanoregulation of the healing fracture as a function of weight bearing is derived from alterations in the micromechanical environment of the fracture site (16, 23, 29, 64, 106). Claes et al. demonstrated that the amount of strain and hydrostatic pressure on the callus surface are determinant factors in the healing process, and that within a certain envelope of these parameters successful differentiation of callus tissue will occur, with excessively low or high strains and/or fluid pressure being detrimental to the healing cascade (29). It has also been shown that increased vascularization and interstitial fluid flow are critical components in the healing process, likely due to increased filtration of fluid across capillaries and more efficient osteoblast nutrition (106). Thus, the decreased callus formation observed under the partial unloading conditions of the current study was likely due to a reduction in these factors. It could be postulated that methods to supply exogenous (i.e. countermeasure) loading within a microgravity environment could be used to return these regulatory factors to within the homeostatic range whereby normal micromechanical regulation is achieved and fracture healing is enhanced.

There are several limitations associated with this study. First, the time span of this study allowed the investigation of the acute stages of healing in which signs of aberrant fracture healing would be most critical; however, the long-term healing characteristics were not investigated. Further, the localized nature of the unloading technique utilized in this model did not allow the investigation of systemic alterations associated with full microgravity unloading such as changes in fluid balance. Finally, the angiogenic response associated with early-stage fracture healing was not characterized.

To conclude, the data reported herein provide strong evidence that the mechanical loading environment dramatically affects the fracture healing cascade and resultant mineralized tissue strength. Therefore, it is imperative to study and develop techniques and technologies that counteract the deleterious effects of reduced loading environments on mineralized tissue healing.

CHAPTER 4:

COMPUTATIONAL CHARACTERIZATION OF FRACTURE HEALING UNDER SIMULATED MICROGRAVITY LOADING CONDITIONS

Introduction

The literature is deficient with regard to the specific alterations in the localized mechanical environment of skeletal tissue during microgravity unloading and how these alterations affect bone remodeling. Additionally, investigations that have attempted to link the direct role of these reduced gravitational forces to fracture healing have been limited (5, 40, 49, 69, 72). The few *in vivo* studies that have been reported have consistently demonstrated that weight-bearing maintains skeletal integrity, and ultimately, accelerates the healing of long bone fractures by promoting rapid callus formation (120). However, the lack of mechanical loading experienced during weightlessness leads to the inhibition of fracture healing (6, 40, 49, 69, 72). More specifically, these studies have demonstrated decreased chondrogenesis, mechanical strength, callus size, osteoblast activity, and bone formation rates in animals that healed in reduced loading environments as compared to those that healed in a full Earth gravity loading condition (5, 40, 49, 69, 72).

Despite the aforementioned findings, alterations in the localized mechanical environment within mineralized tissues due to microgravity unloading remain inadequately described due to the experimental limitations associated with such tasks. However, the use of computational techniques may aid in elucidating the mechanical underpinnings of skeletal adaptation and healing in microgravity environments. Computational models provide insight into mechanical

phenomena that are either too invasive, time intensive, or intractable to quantify experimentally. Localized tissue mechanical metrics such as internal stresses, strains, and forces may be reliably predicted through the use of high-fidelity computational techniques. Due to these advantages, computational methods such as the finite element (FE) method and musculoskeletal modeling have aided orthopaedic research efforts on a broad range of length scales (8-10, 111, 155, 157).

A number of studies have utilized the FE method to investigate the local mechanical environment of healing fractures under normal (Earth) gravity conditions in order to delineate the specific mechanical stimuli responsible for successful healing. Claes and Heigele utilized a FE model to interrogate fracture healing at various stages and reported a specific envelope of strain and hydrostatic pressure as being critical for healing, with strains and pressures outside of that envelope responsible for the formation of fibrous tissue (and eventual non-union) rather than bone (29). Other groups have similarly investigated fracture healing via FE analyses, however, many of these studies have produced qualitative descriptions rather than quantitative results (23). Further, the localized mechanical environment of fracture healing in a simulated microgravity environment has not been rigorously developed and described. Thus, the purpose of this study was to develop a FE model to characterize the local mechanical environment responsible for the inhibited fracture healing observed under experimental simulated microgravity conditions.

Methods

Animal Model

The effects of simulated microgravity on bone remodeling and fracture healing were previously investigated in two large animal (sheep) studies (48, 49). Animal use approval was granted by

the Colorado State University Animal Care and Use Committee (Approval #11-2938A). In the first study, a trans-biarticular fixator (IMEX, Longview, TX) was applied to the hindlimb of five skeletally mature sheep for 8 weeks (ExFix group). This unloading technique was shown to simulate a 0.25g environment (i.e. equivalent to a 75% reduction in loading). An orthopaedic locking plate instrumented with a rosette strain gage (Vishay Precision Group, Malvern, PA) was applied to the dorsal face of the metatarsal bone to quantify bony strains. *In* vivo principal strains of the orthopaedic fixation plates were monitored using a force platform and correlated to measured ground reaction forces (GRFs) of the limb. The second experiment investigated fracture healing using this simulated microgravity model. Following a 21 day simulated microgravity period and a resultant loss of cancellous bone mineral density of approximately 18%, a 3.0mm mid-metatarsal ostectomy was performed and stabilized with an orthopaedic locking plate instrumented with a rosette strain gage. An Earth gravity (Control, n=5) group was included in the study in which an ostectomy was created, plated, and casted, allowing full loading to be transmitted through the bone. *In vivo* principal strains of the orthopaedic fixation plates were once again monitored using a force platform and correlated to measured GRFs of the right hindlimb. Both groups were euthanized after 28-days. Following sacrifice, non-destructive four-point bending experiments were performed on the whole, dissected metatarsal bones using a custom-made fixture coupled to a servohydraulic testing machine (MTS Systems Corporation, Eden Prairie, MN) and the resultant bending stiffness was calculated. Additionally, micro-computed tomography (μCT) and histomorphometric analyses were performed to quantify fracture healing.

Model Generation

A high fidelity FE model of the ovine hindlimb extending from the tibia to proximal phalanges was constructed in order to quantify the localized stresses and strains experienced under simulated microgravity unloading. The bony geometry of the FE model was prepared from CT imagery data of a fully mature Rambouillet Columbian ewe with no known diseases or abnormalities. A series of 1,467 two-dimensional images were imported using AMIRA visualization software (ver. 5.0, VSG, Burlington, MA). The resultant in-plane resolution was 0.35mm isotropic, with an out-of-plane dimension of 0.5mm. The proximal phalanges; metatarsus; centroquartal bone; first, second, and third tarsal bones; talus; and tibia were segmented based on Hounsfield attenuation values, and surface representations of each bone were generated. The three-dimensional mesh for each bone of the hindlimb was generated using TrueGrid software (XYZ Scientific Applications, Inc., Livermore, CA), and rectangular-shaped blocks consisting of 8-noded hexahedral elements were morphed to the surface geometry of each bone to create a preliminary mesh consisting of 215,799 elements.

Articular cartilage was modeled as a 0.5mm, three-element thick layer extruded from the osteochondral surfaces of the phalanges, distal metatarsus, calcaneus, talus, and distal tibia. Transversely isotropic, linearly elastic material properties were assigned to the cortical and cancellous bone, while a hyperelastic Mooney-Rivlin material definition was assigned to the articular cartilage (75, 85, 94, 98, 99, 130). A total of 8 ligaments of the metatarsophalangeal and hock joints were represented using spring elements (130). The overall modeling process is illustrated in Figure 21, while the material properties chosen for all tissues are summarized in Table 4.

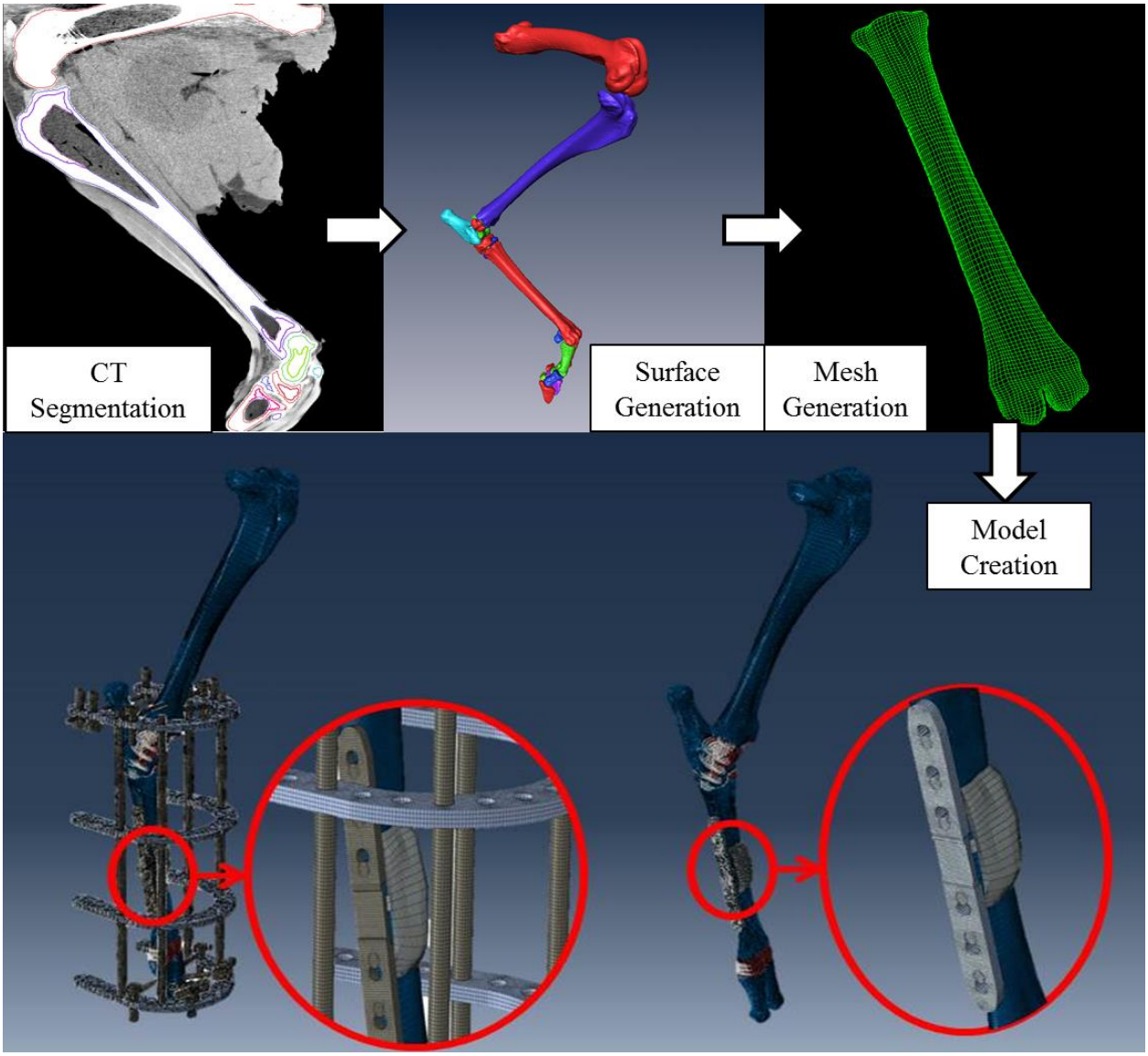

Figure 21. The FE model generation process. Surface geometry was segmented from a CT scan of a mature ewe before being meshed with 8-node hexahedral elements and imported into the finite element software. (Bottom) The (left) ExFix and (right) Control FE fracture models were generated by creating a 3mm ostectomy and callus (red insets) at the mid-diaphysis of the metatarsus.

Table 4. Summary of the mechanical properties used in the FE models. Subscript 1 denotes the longitudinal directions while subscripts 2 and 3 represent the transverse directions.

Material	Elastic Modulus	Poisson Ratio	Reference
Cortical Bone	E_1=22GPa E_2=E_3=11.3GPa	υ_1=0.482 υ_2= υ_3=0.397	(75, 85)
Trabecular Bone	E_1=542MPa E_2=E_3=406MPa	υ_1=0.381 υ_2= υ_3=0.104	(94, 98, 99)
Articular Cartilage	Mooney-Rivlin C_{10}=0.22 C_{01}=2.5 D_1=0.06		(130)
Ligaments	Force-displacement curves		(130)

Parametric Convergence Sensitivity

Mesh refinement of the FE model was verified in order to ensure that model predictions were not influenced by mesh resolution. Three separate models with identical geometric features but differing mesh resolutions were created and labeled LOW (209,201 elements, 736,629 degrees of freedom (DOF)), MEDIUM (305,071 elements, 1,027,182 DOF), and HIGH (434,446 elements, 1,489,620 DOF) according to the respective mesh density of each model.

Each model was constrained at the level of the proximal phalanges via an encastre boundary condition while a 750N (110% body weight) compressive load was applied to the proximal tibia with a kinematic coupling constraint. All solutions were obtained using ABAQUS Standard (ver 6.11, SIMULIA, Providence, RI). The mean strain energy density (SED) corresponding to each constituent tissue was calculated. Additionally, range of motion (ROM) of the hock and metatarsophalangeal joints was compared, as well as contact area, force, and pressure of the hock joint. Predictions from the three models were compared, and those within $\pm$10.0% were deemed to be converged.

In Vitro Validation

Given that the model was intended to predict the loading-motion response and relevant internal mechanical parameters (such as principal strains and stresses) of the hindlimb, a thorough validation process of the model could not be based solely on kinematic data. Hence, model predictions of metatarsal surface strains were compared to experimentally obtained strain data under identical loading conditions. Boundary conditions for the model simulations were imposed as previously described. Experimental metatarsal surface strain and kinematic measurements were taken during simulated hindlimb loading in a servohydraulic material testing machine (MTS Systems Corporation, Eden Prairie, MN). Ovine hindlimbs (n=4) were dissected to include the tibia, metatarsus, phalanges, and associated ligamentous structures. The limbs were potted at the level of the phalanges and proximal tibia using epoxy resin (Smooth-On, Inc., Easton, Pennsylvania), and stacked rosette strain gages (Omega Engineering, Inc., Stamford, CT) were attached to the ventral/dorsal diaphyses and the distal/proximal metaphyseal surfaces of the dorsal face. Three-dimensional stereophotogrammetry was utilized to measure joint rotations (Motion Analysis Corportation, Santa Rosa, CA). Each specimen was loaded to 750N at a rate of 0.25mm/sec, and principal strains were calculated using a custom-written Matlab code (The MathWorks, Inc., Natick, MA). The experimental strain and ROM results were then compared to model predictions.

In Vivo Validation

Following the *in vitro* model validation, a rigorous secondary validation analysis was performed to ensure that the parameters of interest predicted by the model corresponded with experimentally-obtained *in vivo* measurements of bone strain from the first animal experiment.

The external fixation device detailed previously was created in the FE model to shield the metatarsal bone from mechanical loading. Additionally, a Control FE model was utilized in which the external fixation components were omitted. The horseshoe rings of the external fixation device were modeled as linearly elastic aluminum (E=69.0 GPa, υ=0.34) while the remaining components were modeled as linearly elastic stainless steel (E=193GPa, υ=0.29) and secured via tie constraints (21).

Hindlimb muscles were created in both ExFix and Control FE models using a kinematic coupling constraint between a single reference node and a previously-developed 7-segment musculoskeletal model of the ovine hindlimb. The latter model, with 13 degrees of freedom and 31 muscle-tendon units, was scaled to the anthropometrics of the specimen and used to predict the muscle and stifle joint contact forces utilized in the FE analysis during standing with vertical GRFs of 100N, 200N, and 300N (83). The GRF for each model was confirmed at a reference node placed at the base of the model.

The predictions of the models were validated with experimentally-obtained *in vivo* metatarsal bone strains for known hindlimb GRFs in the previously-described animal study plate for single-limb vertical GRFs up to 300N (49). Correlations between bone and orthopaedic plate strain were utilized to calculate the corresponding strains of the proximal and distal sites of the dorsal face as well as the diaphyseal surface of the ventral face of the metatarsus for each group (48). Linear regression analyses were performed (α=0.05) to demonstrate the level of agreement between model predictions and experimental strain data for 100N, 200N, and 300N standing GRFs (SigmaPlot, Systat Software, Inc., San Jose, CA).

Diaphyseal Fracture Modeling

In order to investigate the effects of mechanical unloading on the local mechanical environment of a healing bone fracture, a 3mm mid-diaphyseal ostectomy was created in the ExFix and Control models (Figure 21). The mid-diaphyseal fracture and callus of each specimen were processed for histological analyses wherein callus dimensions were utilized to create a callus of equivalent mesh density for the ExFix and Control FE models. A four-point bending procedure was modeled in identical fashion to the previous experimental method and a range of linearly elastic Young's moduli values from 1MPa to 15MPa were utilized in the computational model to calibrate the model's predicted bending stiffness to experimental results (22, 29, 65, 74, 129). Using the acquired Young's moduli values, each model was then subjected to 100N and 200N GRF standing muscle forces, and the principal strains of the orthopaedic fixation plates were compared to experimental data.

Finally, each model was loaded with muscle and stifle joint contact forces corresponding to 100N, 200N, and 300N GRF standing loads as well as a gait speed of 0.75m/s (corresponding to the maximum speed of the housed animals, or 600N). The local maximum and minimum strain components and hydrostatic pressure within the fracture gap and periosteal callus predicted by the model were then compared with histological results obtained from the *in vivo* animal study.

Results

Animal Experiment

The *in vivo* study demonstrated inhibited healing in animals exposed to simulated microgravity as compared to those that healed in a 1g Earth gravitational environment (49). μCT results indicated decreased callus bone volume while histological examination similarly demonstrated decreased callus cross-sectional area in simulated microgravity specimens versus 1g specimens following 4 weeks of healing. 1g specimens routinely displayed endochondral ossification bone formation in the periosteal callus, as well as lower levels of intramembranous bone formation around the periosteal callus perimeter. The limited healing of simulated microgravity specimens appeared to be mediated directly through intramembranous bone formation without evidence of endochondral ossification (Figure 22).

Parametric Convergence Sensitivity

Mesh density demonstrated the greatest FE model predictive sensitivity with respect to cartilage SED, ligament strain, and joint contact parameters. Differences in these parameters were all reduced to less than 10.0% between the MEDIUM and HIGH resolution models. ROM predictions at the hock joint were least affected by changes in mesh resolution. In all cases, the differences in predictions between the MEDIUM and HIGH resolution models were less than 10.0%, with the highest difference being 6.3% for cartilage SED. Therefore the MEDIUM resolution model was considered converged and used for all subsequent FE analyses.

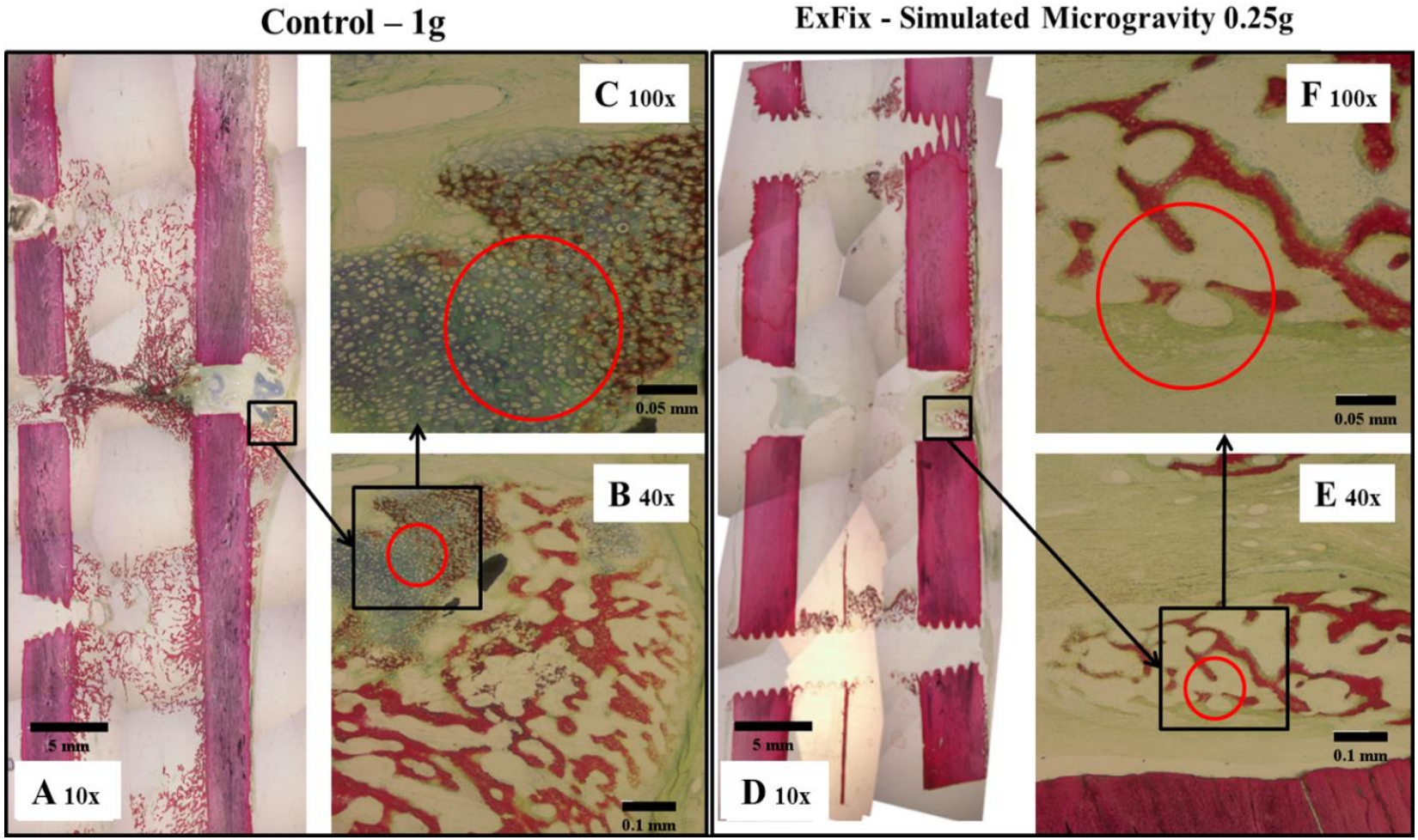

Figure 22. (Images A, B, and C) Experimental 1g control specimens routinely displayed endochondral ossification bone formation in the periosteal callus as well as reduced intramembranous bone formation around the callus perimeter. A combination of mineralized callus and hypertrophied chondrocytes (circled) can be seen within the healing callus. (Images D, E, and F) The simulated microgravity specimens appeared to heal directly through intramembranous bone formation (circled) within the opposing cortices of the fracture gap. Histology slides were stained with Sanderson's Rapid Bone Stain and counter-stained with Van Gieson.

In Vitro Validation

The load-displacement response of the hindlimb model was in reasonable agreement with experimental data. Joint rotations of 5.0° and 1.9° for the hock and metatarsophalangeal joints, respectively, predicted by the model fell within one standard deviation of the experimentally-derived data (hock ROM=6.9°$\pm$2.4°, metatarsophalangeal ROM=1.6°$\pm$0.5°). Principal strain predictions of the model typically fell within one standard deviation of experimental data, with a median difference between experimental data and model predictions of 13.7%.

In Vivo Validation

The *in vivo* principal strain predictions of the ExFix and Control models demonstrated high levels of agreement with the experimental data. Results of the linear regression analyses are presented in Figure 23. The regression analysis of the ExFix model data resulted in a linear slope of 1.05, an r^2 value of 0.86, and a p-value of <0.001, demonstrating a high level of agreement between the experimental data and model predictions. Similarly, results of the Control model analysis yield a linear slope of 1.02, an r^2 value of 0.87, and a p-value of <0.001. Additionally, the ventral diaphysis, an area of high importance due to its relevance in this fracture healing investigation, predicted strains within one standard deviation of the experimental data for most loading conditions for both models.

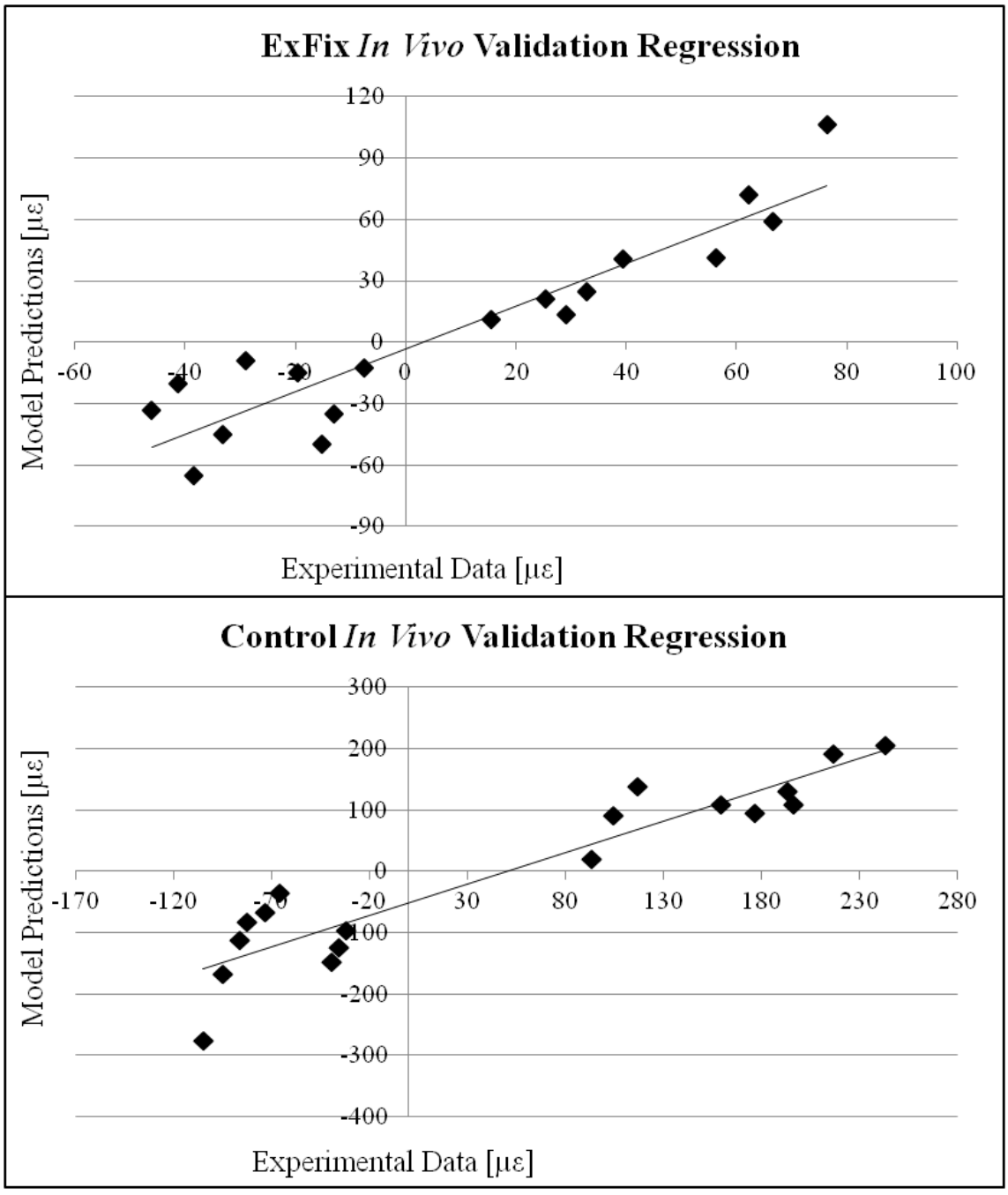

Figure 23. Metatarsal experimental principal strains were plotted against model predictions of the (Top) ExFix and (Bottom) Control models under 100N, 200N, and 300N static GRF loading. The data of the ExFix and Control models were fitted with linear slopes of 1.

Diaphyseal Fracture Modeling

Results of the 4-point bending experiment demonstrated mean (±standard deviation) ExFix and Control group four-point bending stiffnesses of 48.9N/mm (±47.8N/mm) and 213.3N/mm (±36.3N/mm), respectively. Based on the 4-point bending FE analysis, the corresponding moduli of elasticity for the ExFix and Control fracture gaps were computed to be 1.69MPa and 8.45MPa, respectively. These callus material properties fell within the envelope of previously-reported values utilized in similar FE fracture healing studies (22, 23, 29, 82). All subsequent orthopaedic plate strain predictions fell within one standard deviation of the experimental data for all loading scenarios (Figure 24).

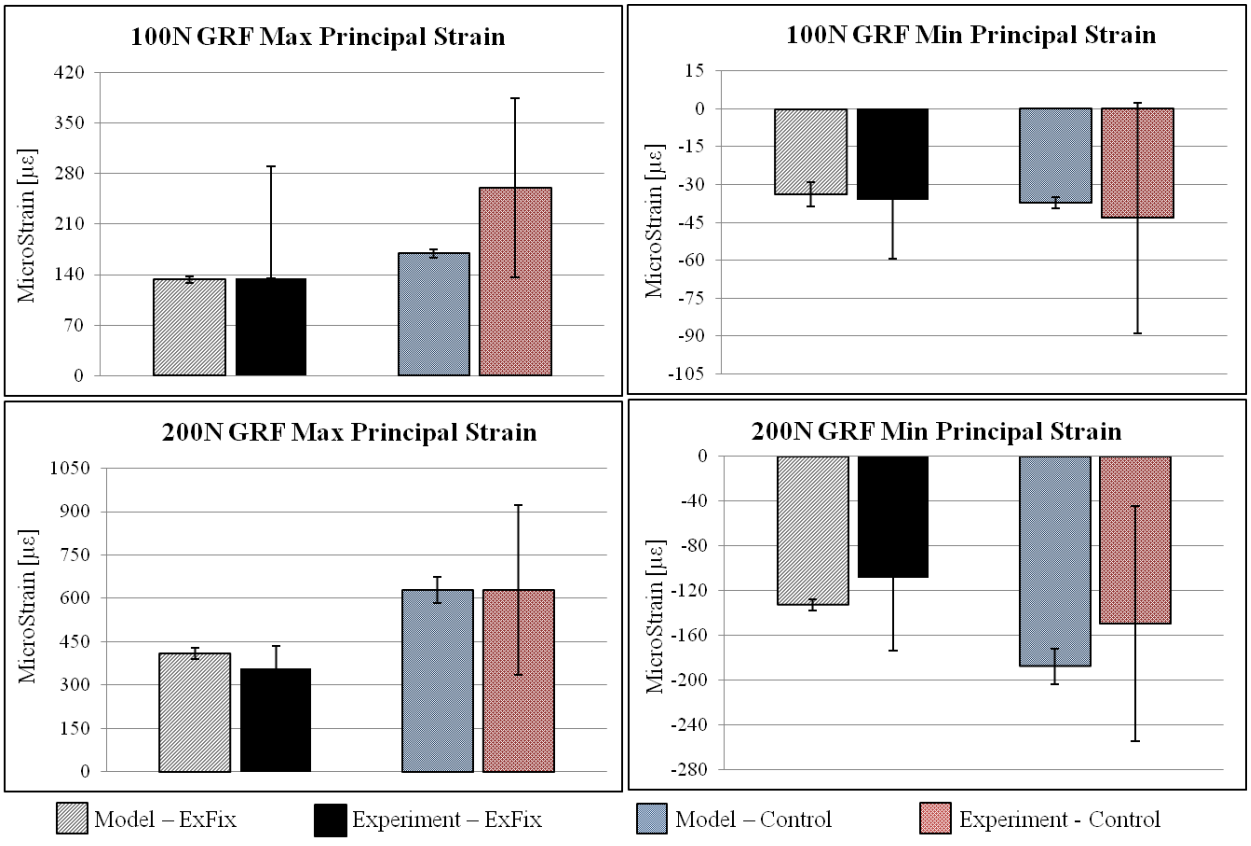

Figure 24. Orthopeadic fixation plate strain predictions for the ExFix and Control models subjected to 100N and 200N GRF loading fell within one standard deviation of experimental data. Model predictions indicate the mean and standard deviation of nodal predictions within the area of interest.

As expected, hydrostatic pressure and strain predictions were greatest when a GRF of 600N (corresponding to a 0.75m/s gait speed) was imposed on both FE models and decreased as a function of GRF. Both models predicted peak hydrostatic pressures and principal strains within the cortices of the fracture gap contralateral to the orthopaedic fixation plate, with both parameters decreasing radially toward the callus periphery (Figure 25). The Control model predicted a peak hydrostatic pressure of -0.59MPa (compressive) within the fracture gap and maximum and minimum principal strains of 5.0% and -10.9%, respectively. The ExFix model predicted a peak hydrostatic pressure of -0.1MPa within the fracture gap and peak maximum and minimum principal strains of 3.7% and -7.6%, respectively.

Discussion

To date, limited work has been done to characterize the local mechanical environment of healing fractures as it relates to simulated microgravity and potential long duration human space travel. This study sought to quantitatively characterize this healing environment and relate the findings to *in vivo* histological results. Comparisons between the local mechanical environment of the ExFix and Control Models demonstrated large differences in hydrostatic pressure and strain over the range of loading scenarios. These differences became more profound as GRF loading increased. Hydrostatic pressure was more sensitive to the decreased mechanical loading of the ExFix Model as compared to the Control Model. It has been suggested that hydrostatic pressure and strain in the fracture and surrounding callus are the key mechanical signals that drive the fracture healing sequelae (29).

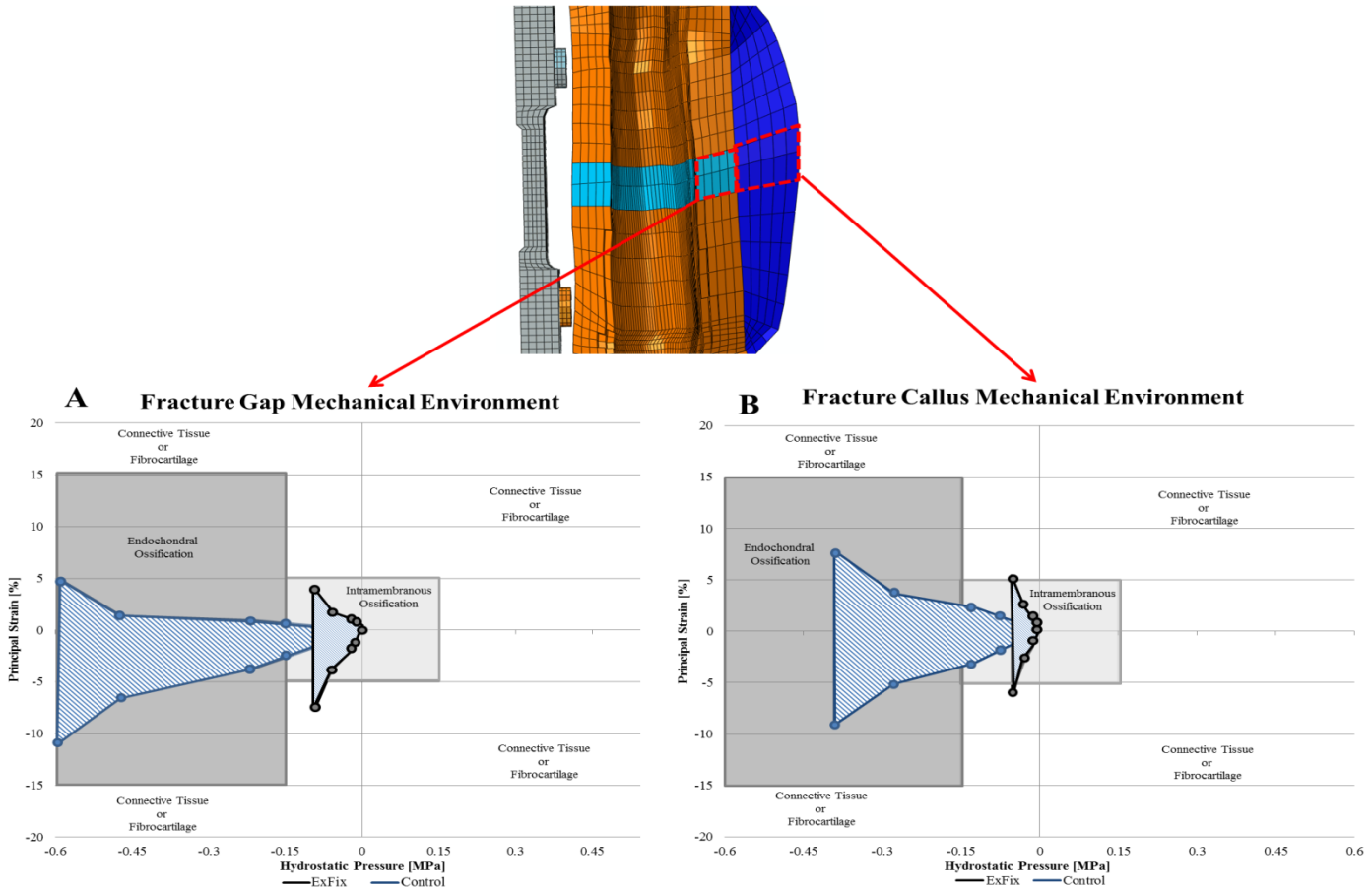

Figure 25. Specific hydrostatic and principal strain envelopes have been previously reported to initiate intramembranous ossification, connective tissue/fibrocartilage formation, and endochondral ossification by Claes and Heigele (29). Plotting the data of the current study over these previous results demonstrate the hypothesized course of healing for each model. (A) Both models predicted the greatest levels of hydrostatic pressure and principal strain in the fracture gap contralateral to the fixation plate. The Control model predicted peak hydrostatic pressure and principal strains within the endochondral ossification envelope for GRFs greater than 100N while all hydrostatic pressure and strain predictions fell within the intramembranous ossification zone for the ExFix model. (B) Hydrostatic pressure and strain predictions were decreased within the fracture callus. The lower bound of each curve corresponds to the hydrostatic pressure and respective minimum principal strain while the upper bound corresponds to the hydrostatic pressure and respective maximum principal strain for GRFs from 0N to 600N.

Previous work by Claes and Heigele investigated fracture healing in a large animal model and correlated histological data with FE strain and pressure predictions, concluding that intramembranous bone formation occurs within hydrostatic pressure ranges of $\pm$0.15MPa and principal strains of $\pm$5%, while compressive hydrostatic pressures in excess of 0.15MPa would lead to a different healing pathway in which endochondral ossification dominates (29, 65). In their work, peak hydrostatic pressures and strains were observed within the cortices of the fracture gap, with pressure decreasing radially toward the callus periphery. Similarly, in the current study, strains were predicted to be highest within the fracture gap and substantially reduced within the callus. The results of our complementary animal studies further support these findings. The values reported for the Control model fall within the reported range for endochondral ossification healing for standing GRFs as well as higher GRFs experienced during daily ambulation by the test animals. Further, endochondral ossification was determined to be the primary form of healing in histological sections obtained for animals of the Control group. The peak hydrostatic pressure and strain values predicted for the ExFix model fell within the range of previously reported values that are hypothesized to stimulate intramembranous bone formation, and did not elevate to the level of values that have been reported to initiate endochondral ossification. These findings were confirmed histologically from the experimental ExFix group specimens wherein intramembranous ossification between the cortices of the fracture gap was commonly observed with minimal fracture callus. Predictions of principal strains outside of the intramembranous bone formation range may have contributed to the growth of fibrous tissue within the healing fracture. Altogether, these findings indicate that the reduction in mechanical loading during simulated microgravity is related to a clinically important decrease in hydrostatic pressure and strain, resulting in overall diminished levels of healing bone tissue that formed via

intramembranous bone formation rather than the endochondral ossification experienced during normal healing in a 1g Earth gravitational environment.

The current knowledge gap regarding the characterization of the local mechanical environment of fracture healing in a simulated microgravity environment may be attributed to the experimental limitations associated with such tasks. However, computational methods provide the ability to gain further insight into these phenomena. Reliable models must first be successfully validated to ensure high levels of fidelity (4, 67). The current model underwent a rigorous parametric convergence study to ensure that model reliability was not altered by element density. The results demonstrate that soft tissue model predictions are highly dependent on mesh resolution. However, ROM predictions were only slightly affected by mesh resolution, providing evidence that it is necessary to validate the specific outcome parameters of interest rather than relying on global kinematics when developing a dependable model. The successful completion of the rigorous validation process demonstrates the capability of this model to accurately predict the parameters of interest in this study.

There were several limitations associated with this study. First, the modeling of the fracture callus included several simplifications, most notably the implementation of linearly elastic material properties to model soft tissue mechanical behavior. While we did not explicitly model the non-linear behavior of soft tissues, this implementation has been widely used in numerous FE studies that have modeled a healing fracture (74, 129). Also, tissue types within the fracture callus were not differentiated; however, the parametric analysis performed in determining callus properties negated this simplification by evaluating the global callus stiffness as a gestalt. Fluid

flow contributions that may influence fracture healing were also not explicitly modeled. Accordingly, time-dependent alterations such as remodeling, callus growth, and changes in bone mineral density were not investigated in the current modeling attempt.

In conclusion, the mechanical unloading experienced during simulated microgravity resulted in inhibited fracture healing by inducing fundamental changes in the bone formation processes. The FE model predictions suggest that reduced hydrostatic pressure and strain of the healing fracture contributed to alterations in the healing process, with animals exposed to a simulated microgravity environment subsequently healing via intramembranous bone formation rather than the typical endochondral ossification process experienced by animals healing in an Earth gravitational environment. Further work should concentrate on candidate countermeasures that may be able to restore the natural loading milieu to fractures healing in microgravity environments.

CHAPTER 5:

SHOCK WAVE THERAPY AND LOW-INTENSITY PULSED ULTRASOUND ACCELERATE BONE FORMATION RATES UNDER SIMULATED MICROGRAVITY LOADING CONDITIONS

Introduction

The inherent reduction in mechanical loading associated with microgravity has been shown to result in dramatic decreases in the bone mineral density (BMD) and mechanical strength of skeletal tissue (48, 76). Previous astronaut spaceflight data have demonstrated mean losses in BMD of 1%-3% per month in weight bearing skeletal locations (76). This issue becomes particularly important when considering the implications involved with long-duration spaceflight missions (i.e. to Mars) and the expected resultant declines in skeletal mechanical competency and anticipated increase in fracture risk (77, 100). In addition to this elevation in fracture risk, previous work has demonstrated that skeletal fracture healing is severely inhibited by the microgravity environment experienced during spaceflight (49, 69, 72). Using a rat model, Kerchin et al. showed that bone healing was altered during spaceflight, resulting in suppression of chondrogenesis within the periosteal reaction and angiogenesis within the osteotomy gap (72). Additionally, Kaplansky et al. reported decreased fracture callus size and consolidation strength resulting from inhibited osteoblast activity in rodents during a 14-day spaceflight experiment (40). Similarly, Gadomski et al. demonstrated decreased fracture healing rates resulting in diminished callus size and strength due to decreased osteoblast numbers in a ground-based large animal (sheep) model (49). Based on these findings, it is important to investigate possible

countermeasures to the inhibited fracture healing experienced in reduced gravity environments for future long-duration spaceflight missions.

Shock wave therapy (SWT) and low-intensity pulsed ultrasound (LIPUS) have been used to treat soft and hard tissue pathologies by utilizing focused supersonic acoustic waves directed across the affected tissue, with the main difference between the two therapies being the relatively high energy level of SWT as compared to LIPUS. Studies detailing the use of SWT and LIPUS have shown that the administration of supersonic acoustic pulses directly to soft and hard musculoskeletal tissues provides beneficial healing characteristics when applied to chronic conditions such as tendinopathy, plantar fasciitis, calcaneal spurs, and lateral epicondylitis of the elbow. Most germane to the current work, LIPUS and SWT have been used to treat nonunion and delayed healing of bony fractures in humans by generating low-level mechanical stresses at the fracture site and inducing subsequent cellular and molecular responses involved in the healing cascade (27, 61, 63, 66, 109, 121, 151, 152). Further, due to its noninvasive nature, ease of administration, low complication rate, and high efficacy, SWT and LIPUS have become well-accepted and commonly used clinical therapeutic techniques (43, 56, 63, 124, 150, 159).

The literature is replete with human clinical studies investigating the use of SWT and LIPUS for the delayed healing of bony fractures. Xu et al. reported a 75.4% success rate in the healing of previous bony nonunions using SWT in various locations including the femur, tibia, radius, and ulna in otherwise healthy middle-aged men and women (159). A comparative study performed by Furia et al. in which chronic fracture nonunion of the fifth metatarsal in humans was treated with either SWT or intramedullary screw fixation revealed that both therapeutic interventions

were effective for the treatment of fracture nonunions, however, a lower complication rate and fewer additional surgical procedures were associated with the use of SWT (47). Human clinical trials have further established the efficacy of LIPUS treatment. A study by Heckman et al. demonstrated a 38% reduction in time to overall clinical and radiographic healing of grade-I open tibial fractures with the use of LIPUS as compared to a control group (56).

At the cellular level, it appears that the beneficial effects of SWT and LIPUS as therapeutic interventions to aberrant fracture healing is a result of increased osteoblast differentiation combined with decreased pro-osteoclastogenic factors (53, 140). A study utilizing SWT to treat fracture healing in rabbits found the treatment to stimulate an increase in endothelial nitric oxide synthase (eNOS), bone morphological protein (BMP-2), vessel endothelial growth factor (VEGF), and proliferating cell nuclear antigen (PCNA) to be responsible for the resultant increase in fracture healing (151). Other studies have demonstrated that SWT administration leads to increased fibroblast, chondroblast, and osteoblast differentiation as well as enhanced angiogenesis and increased fluid flow to the fracture site (53, 114, 119). Thus, the objective of this study was to interrogate the efficacy of these two therapies as countermeasures to the inhibited fracture healing experienced during simulated microgravity in a previously-developed large animal (sheep) model (48).

Methods

Twenty eight skeletally mature Rambouillet Columbian ewes (age > 6 years) were used in this study. Animal use approval was granted by the Colorado State University Animal Care and Use Committee (Approval #11-2938A). Fourteen animals were allocated to the 0.25g Group and

underwent hindlimb metatarsal unloading as described by Gadomski et al (48). Briefly, a trans-biarticular external skeletal fixation device (IMEX, Longview, TX) was implanted on the right hindlimb such that the metatarsal bone was isolated from mechanical loading. Previous *in vivo* experiments demonstrated that this external fixation unloading system was able to reduce metatarsal bone loading by 75%, creating a mean relative gravity environment of 0.25g (48). These animals were then exposed to mechanical unloading of the metatarsal bone for a period of 3 weeks (21 days). An ostectomy procedure was performed at the 3-week time point by removing a 3.0mm section of bone from the mid-diaphysis of the metatarsus in order to simulate a mid-mission fracture. The ostectomy was then stabilized via a laterally-attached orthopaedic locking plate (Synthes, Inc., Westchester, PA) instrumented with a rosette strain gage (Vishay Precision Group, Malvern, PA). An additional Earth gravity group of 14 animals (1G Group) was included in which an identical 3.0mm ostectomy was created, plated, and casted, allowing full loading to be transmitted through the metatarsal bone. SWT was administered to five animals from each of the two groups (0.25G-SWT and 1G-SWT, Figure 26) 6 days following the creation of the ostectomy with an applied energy of 0.63 mJ/mm^2, a frequency of 5Hz, and a total shock count of 4,000 (Storz Medical AG, Tägerwilen, Switzerland). LIPUS was administered to four animals from each group (0.25G-LIPUS and 1G-LIPUS, Figure 27) two days following surgery for 20 minutes per day, five days per week for the remainder of the four-week healing period by receiving a 200-µsec burst of 3.3MHz sine waves repeated at 1 kHz with an average intensity of 20 mW/cm^2. The remaining ten animals were divided into microgravity (0.25G-C) and Earth gravity (1G-C) control groups in which both groups underwent the surgical and testing protocols detailed previously but did not receive treatment. All groups were euthanized after a 28-day healing period.

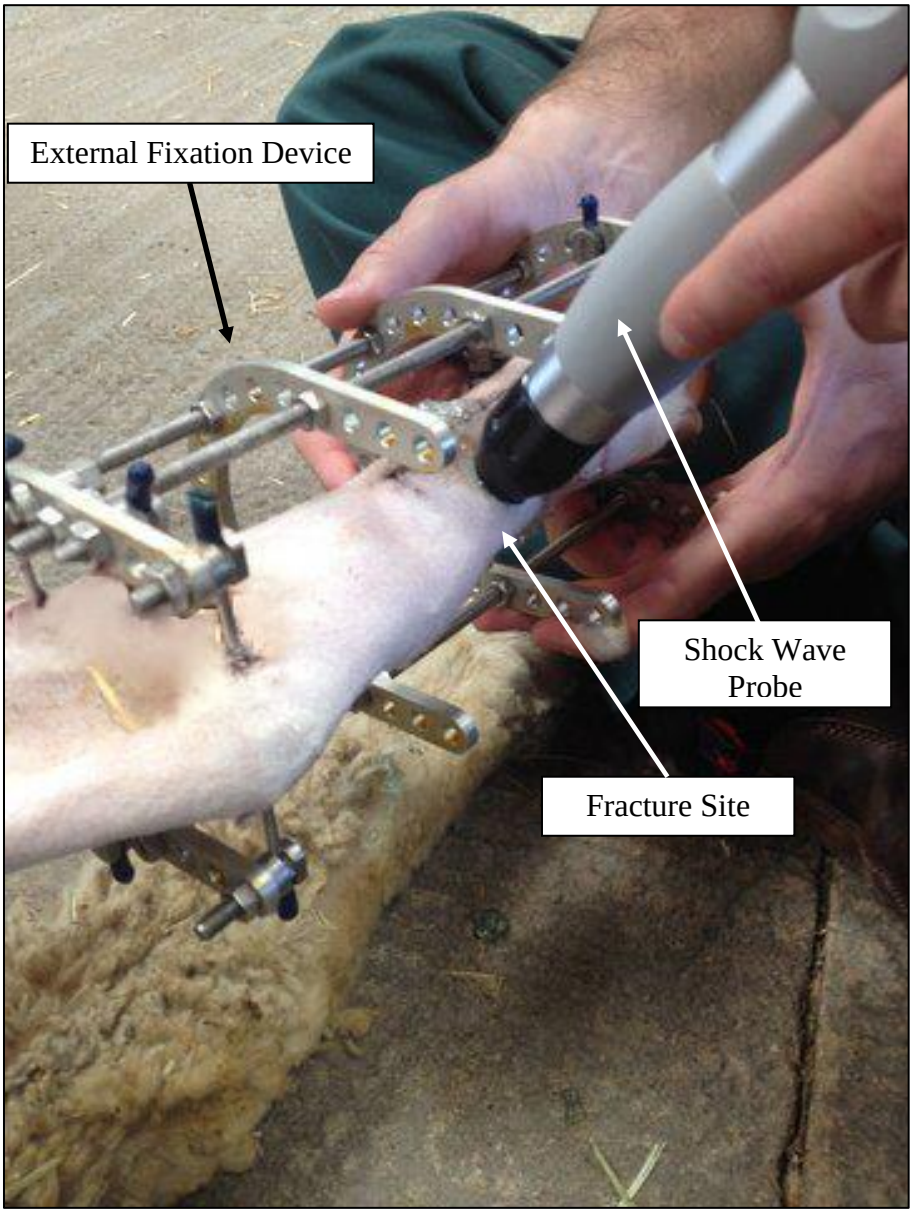

Figure 26. SWT was administered around the circumference of the fracture site of the 0.25G-SWT and 1G-SWT groups 6 days following the creation of the ostectomy.

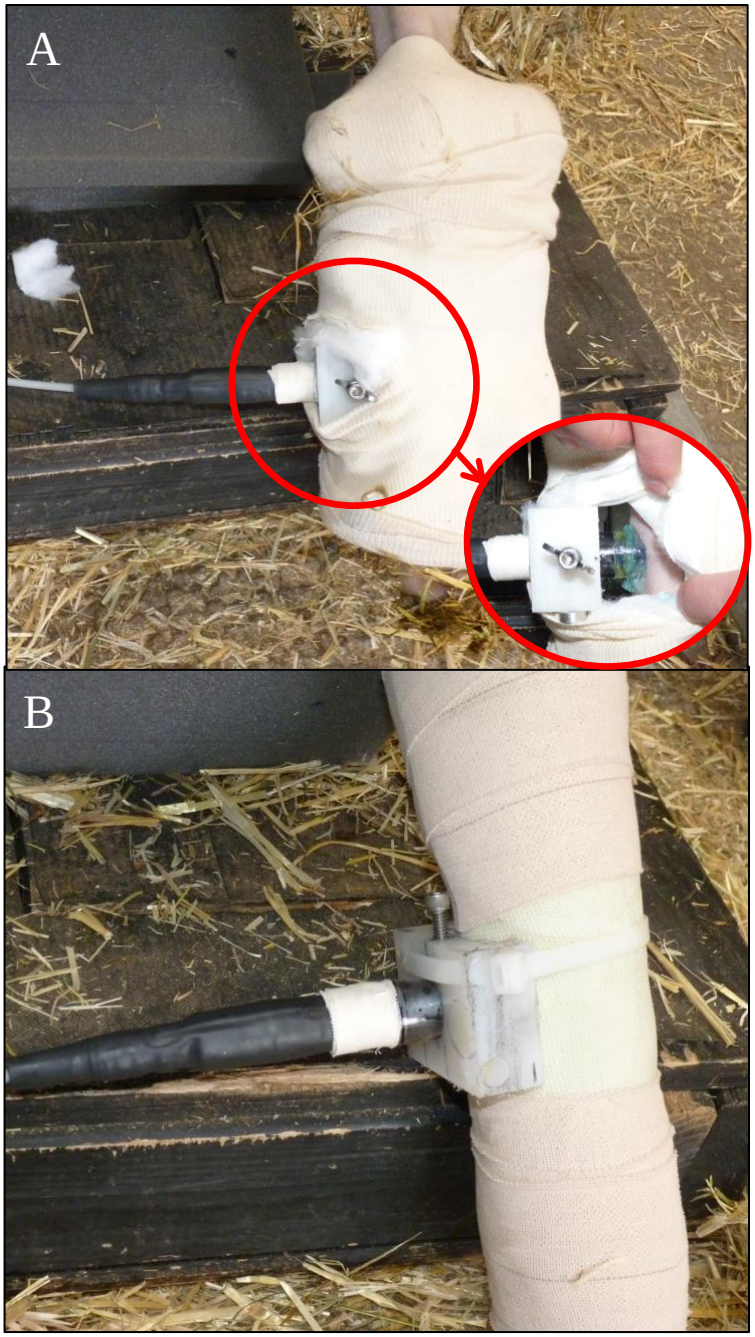

Figure 27. (A) The ultrasound probe was secured to the external fixation frame via a polyethylene fixture to ensure identical placement against the skin overlaying the metatarsal diaphysis between treatment sessions for 0.25G-LIPUS animals. (B) The ultrasound probe was inserted through a pre-drilled hole in the fiberglass cast of 1G-LIPUS animals to attain skin contact and secured via a polyethylene fixture.

In Vivo Testing

Dual-energy x-ray absorptiometry (DEXA) scans (Discovery A, Hologic, Inc., Bedford, MA) were performed on the treated metatarsi of the 0.25G groups at the time of the external fixation surgery, the ostectomy surgery, and every two weeks until sacrifice to obtain a clinical measure of BMD. DEXA scans were performed on the 1G groups at the time of the ostectomy surgery and every two weeks until sacrifice. Scans were analyzed in identical 10mm x 10mm regions of interest (ROIs) aligned with the proximal aspect of the condyle arch of the distal metaphysis of the treated metatarsi (48). Three scans were performed per bone, and the average BMD was calculated per scan time point for each animal. Longitudinal BMD values were normalized to the baseline BMD value for each animal for comparisons between groups.

In vivo mechanical competency of the healing fracture was evaluated bi-weekly via strain measurements of the orthopaedic plate by testing each animal on a force sensing platform. The instrumented hindlimb of each animal was first suspended to establish a zero load baseline. Strain measurements from the metatarsal plate for single-limb ground reaction forces up to 200N were then recorded for the standing animals. The strains measured in the orthopaedic locking plates were correlated to ground reaction forces between 50N and 200N, and the resultant slope magnitude (με/N) per testing day was calculated to characterize the change in load burden for each group over the course of the study. Additionally, weekly radiographs were taken to monitor the bone-pin interface of each animal. Fluorochrome labels were administered 21 and 7 days (calcein green at 20 mg/kg) prior to sacrifice.

Biomechanical Evaluation

Following sacrifice (four weeks post-operative), biomechanical evaluations were performed on the treated metatarsi of each group. Non-destructive four-point bending experiments were performed on whole, dissected metatarsal bones using a custom-made four-point bending fixture coupled to a servohydraulic material testing machine (MTS Systems Corporation, Eden Prairie, MN). The test frame's actuator was lowered at a rate of 1.0mm/sec to 200N or to the specimen's maximum deflection prior to inducing damage (39). The sample was preconditioned 5 times and the load-displacement data from the final cycle were utilized to calculate the specimen bending stiffness.

Micro-Computed Tomography

Post-sacrifice micro-computed tomography (μCT) analyses were performed at the mid-diaphyseal fracture of the treated metatarsi of each group using the following parameters: voltage: 70kVp, current: 114μA, integration time: 500ms (Scanco μCT 80, Sanco Medical AG, Bruttisellen, Switzerland). A 1.5mm thick region of interest (ROI) was created within the fracture gap and centered between the superior and inferior bone surfaces, and bone volume fraction (BV/TV, %) as well as BMD (mg HA/cm^3) were quantified for each specimen. Additionally, the periosteal fracture callus was segmented between the inner-most screw holes of the metatarsal diaphysis (23.0mm length) to include all external callus while excluding diaphyseal bone, and total bone volume (mm^3) as well as BMD (mg HA/cm^3) were quantified for each specimen.

Histomorphometric Analysis

Following µCT analysis, the treated metatarsi were processed for decalcified and undecalcified histological analysis. Samples were fixed in 70% ETOH for 2 weeks. For undecalcified preparation, samples were dehydrated in graded solutions of ETOH on a tissue processor (Tissue-Tek VIP, Sakura, Torrance CA). The samples were cleared with acetone and infiltrated with a series of three solutions containing Acrylosin and a catalyst of Percodox 16 (Dorn and Hart Microedge, Villa Park, IL). Samples were placed in solution 1 (100% acrylosin), solution 2 (Acrylosin + 1/2 catalyst), and solution 3 (Acrylosin + full catalyst) over the course of approximately 20 days. Once infiltration was complete, the specimens were polymerized into a hardened plastic block. For decalcified preparation, separate samples were placed in Formical 4 decalcifying solution (Decal Chemical Corporation, Tallman, NY) following the initial fixing period until fully decalcified as verified via radiographic examination. Samples were subsequently dehydrated in graded solutions of ETOH, infiltrated with paraffin on a tissue processor (Tissue-Tek VIP, Sakura, Torrance CA), and embedded using standard paraffin histology techniques (Thermo Shandon Inc, Pittsburgh, PA).

Histological sections were taken in the transverse (mediolateral) plane to include the fracture site and associated callus of the diaphyseal region of the metatarsus. Four sections were cut from each specimen. Undecalcified sections were taken using an Exakt diamond blade bone saw (Exakt Technologies, Oklahoma City, OK) at a thickness of 300-400 microns, and ground using an Exakt micro grinder to a thickness of approximately 50 microns. Two sections from each specimen were stained with Sanderson's Rapid Bone Stain and counter-stained with Van Gieson, while the other two sections were left unstained for dynamic histomorphometric analysis. The

decalcified paraffin blocks were faced and two 8 micron sections were cut on a Leica RM2255 rotary microtome (Leica, Nussloch, Germany) and stained with Hematoxylin and Eosin.

High-resolution digital images were acquired for histomorphometric analysis using a Spot Imaging system (Diagnostic Instruments, Sterling Heights, MI), a Nikon E800 microscope (AG Heinze, Lake Forest, CA), and analyzed with an Image Pro imaging system (Media Cybernetics, Silver Spring, MD). For static histomorphometric analysis, images (at 10x magnification) were acquired and area fractions of mineralized tissue were calculated in the periosteal callus, diaphyseal cortices, and intramedullary canal. Bone tissue area fractions were calculated within the periosteal callus, diaphyseal cortex, and intramedullary canal. In order to account for inter-specimen variations in fracture site geometry, the ratio of segmented tissue area to the total area of the respective ROI was calculated. Bone tissue area fractions (%) were calculated for the periosteal callus in the ROI determined by selecting and segmenting callus material contralateral to the orthopaedic plate on the exterior surface of the bone within 11.5mm of the fracture centrum. Diaphyseal cortex bone tissue fractional areas (%) were selected within the mediolateral confines of the diaphyseal cortical shell and craniocaudal edges of the fracture gap and calculated by taking the ratio of respective tissue area within the ROI to total ROI area. Intramedullary canal bone tissue fractions (%) were similarly determined by segmenting the images within the confines of the intramedullary canal and within the boundaries of the cranial and caudal fracture gap edges. For dynamic histomorphometry, three fluorescent images were acquired per specimen (at 40x magnification) within the periosteal callus and mineralizing surface (MS), mineral apposition rate (MAR), and bone formation rate (BFR) were calculated (48). Analysis was not performed on the endosteal surface due to the consistent absence of

endosteal bone formation. Decalcified cellular histomorphometry was performed on digital images (at 200x magnification) for three ROIs within the periosteal callus and on the endosteal surface per specimen to determine osteoblast (Ob.N) and osteoclast (Oc.N) number.

Statistical Analysis

Statistical analyses were performed using a two-way analysis of variance (ANOVA) for comparisons across groups and a repeated measures one-way analysis of variance (ANOVA) for longitudinal DEXA and strain comparisons within 1G and 0.25G groups with Student-Newman-Keuls *post-hoc* tests (α=0.05). A Kruskal-Wallis ANOVA on ranks was performed in the event that data were not normally distributed (SigmaPlot, Systat Software, Inc., San Jose, CA).

Results

In Vivo Testing

In vivo DEXA scans displayed statistically significant losses in metatarsal BMD in all 0.25G groups between day 0 and day 21 (Figure 28). There were no statistically significant differences between the 0.25G-SWT, 0.25G-LIPUS, or 0.25G-C groups during the course of the study nor were there significant differences between 1G groups. *In vivo* strain measurements demonstrated no significant alteration in plate strain between 0.25G or 1G groups at the conclusion of the healing period (Figure 29).

Biomechanical Evaluation

Results of the 4-point bending test demonstrated no statistically significant differences in stiffness between the 0.25G groups or 1G groups, with mean ($\pm$ standard deviation) four-point

bending stiffnesses of 98.65 (±87.85) N/mm, 77.26 (±27.00) N/mm, and 48.9 (± 47.8) N/mm for 0.25G-SWT, 0.25G-LIPUS, and 0.25G-C groups, respectively, and 349.30 (±259.50)N/mm, 214.12 (±167.30)N/mm, and 213.3 (± 36.3) N/mm for 1G-SWT, 1G-LIPUS, and 1G-C groups, respectively (Figure 28).

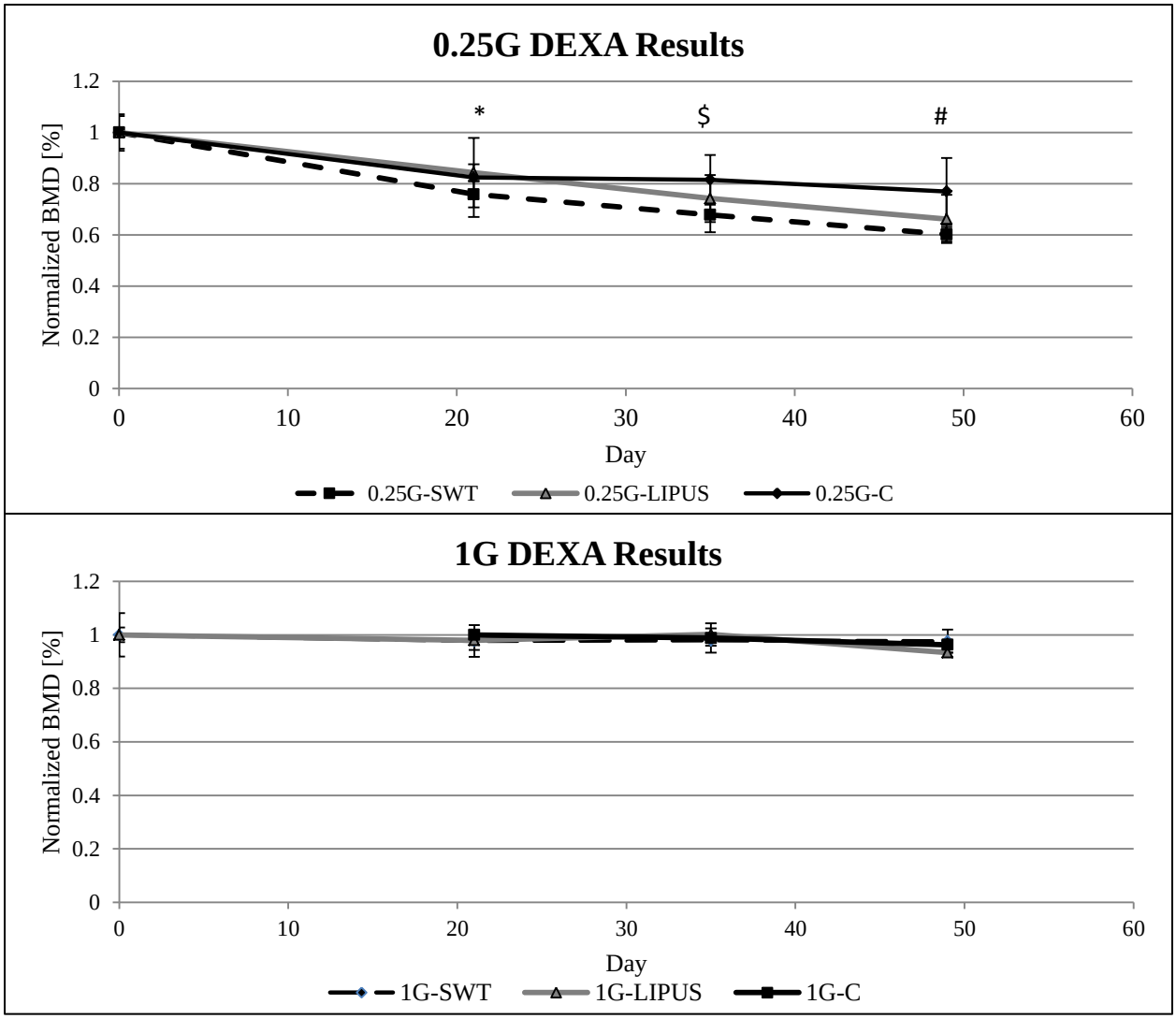

Figure 28. (Top) *In vivo* DEXA scans demonstrated statistically significant losses in metatarsal BMD in all 0.25G groups following the initial 3-week unloading period ($p<0.05$); however, final BMD was not significantly different between 0.25G groups. (Bottom) 1G groups did not display significant alterations in BMD over the course of the study.

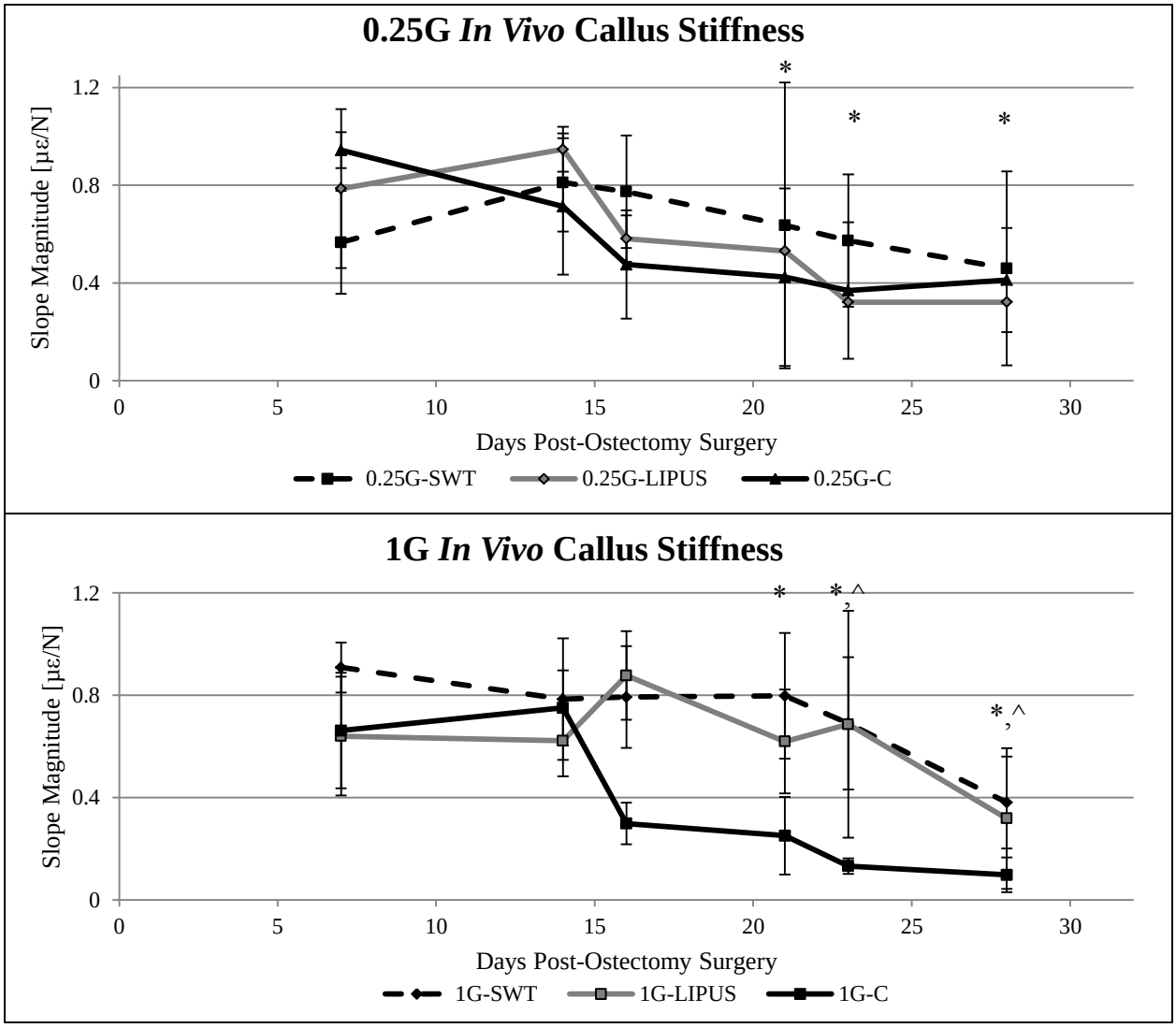

Figure 29. (Top) *In vivo* measurements demonstrated increased callus stiffness (i.e. decreased slope magnitude of the orthopaedic fixation plate) in the 0.25G-C group versus baseline values (Day 7) beginning at Day 21 and continuing through the remainder of the study (*, $p<0.05$). No significant alterations in callus stiffness were observed over the course of the healing period for the 0.25G-SWT or 0.25G-LIPUS groups. Additionally, no significant alterations in final callus stiffness (Day 28) were observed between 0.25G groups. (Bottom) Significantly elevated callus stiffnesses were observed in the 1G-SWT (^, $p<0.05$) and 1G-C (*, $p<0.05$) groups beginning at Day 23 and 21, respectively, as compared to their respective baseline values of Day 7. No significant alterations were observed in the 1G-LIPUS group over the course of the healing period. Significant differences between 1G groups at Day 28 were not observed.

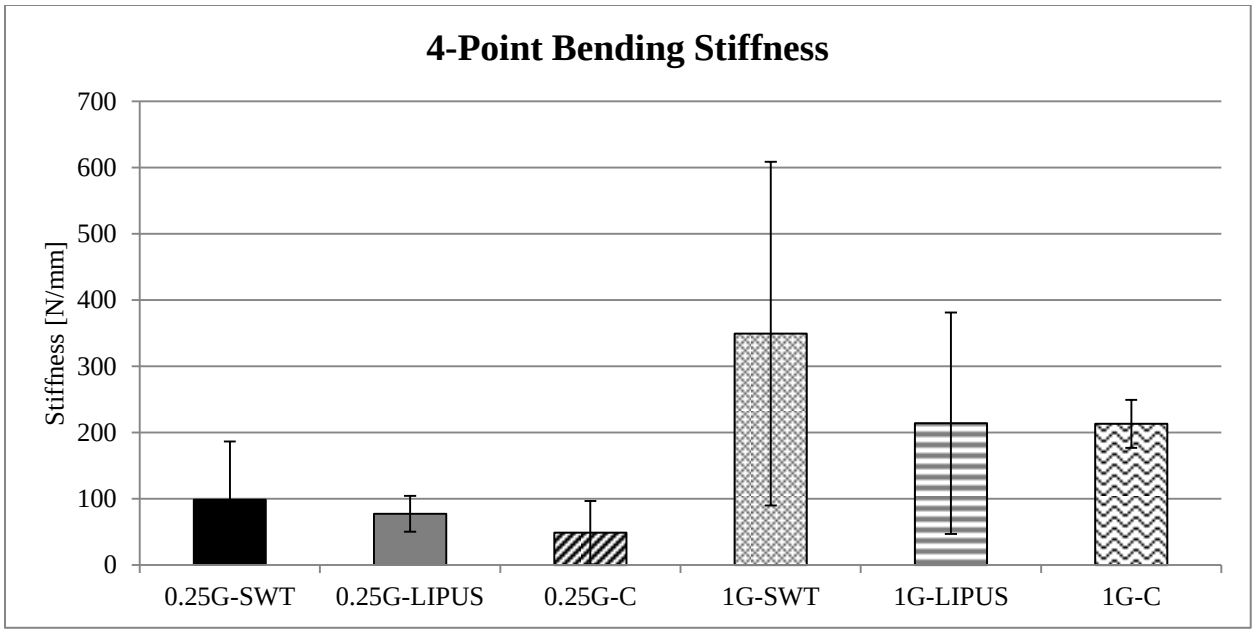

Figure 30. 4-point bending stiffness was not significantly altered in 0.25G or 1G specimens following SWT or LIPUS treatment.

Micro-Computed Tomography

Significant alterations in bone volume fraction (BV/TV) and BMD within the fracture gap were not observed following SWT or LIPUS treatment as compared to control specimens for the 0.25G or 1G gravitational groups (Table 5). Additionally, no significant changes in callus BMD were experienced between groups. Callus bone volume (BV) was not significantly elevated in 0.25G-SWT or 0.25G-LIPUS groups as compared to 0.25G-C specimens; however, callus BV was significantly reduced in 1G-LIPUS specimens as compared to 1G-C and 1G-SWT specimens ($p<0.05$).

Histomorphometric Analysis

Histomorphometric analyses demonstrated significantly elevated callus BV/TV values in 0.25G and 1G specimens treated with LIPUS as compared to those that received SWT or no treatment

($p<0.05$, Table 5). Intracortical and intramedullary BV/TV values were elevated in 1G and 0.25G specimens treated with SWT and LIPUS as compared to their respective control groups; however, these alterations were not significant. Cellular numbers as well as bone formation parameters were significantly elevated in the 0.25G-SWT and 0.25G-LIPUS groups as compared to the 0.25G-C group. Osteoblast numbers were increased 87% and 120% in 0.25G-SWT and 0.25G-LIPUS specimens as compared to 0.25G-C specimens on the periosteal surface, respectively, and 152% and 244% on the endosteal surface, respectively ($p<0.05$). Osteoblast numbers were significantly elevated in 1G-LIPUS specimens as compared to altered 1G-SWT and 1G-C groups, with increases of 18% and 23% in 1G-SWT and 1G-LIPUS specimens as compared to 1G-C specimens, respectively ($p<0.050$). Endosteal osteoblast numbers were not significantly altered in 1G groups following treatment, with observed increases of 2% and 18%, respectively. Periosteal osteoclast numbers were significantly reduced by 82% and 86%, respectively, in 0.25G-SWT and 0.25G-LIPUS specimens as compared to 0.25G-C specimens ($p<0.05$). No significant changes in osteoclast numbers were observed in the periosteal callus of 1G specimens, and no significant alterations in osteoclast numbers were observed between any group on the endosteal surface. MS was significantly increased by 53% and 92%, respectively, in 0.25G-SWT and 0.25G-LIPUS specimens, while BFR was significantly elevated 88% and 80%, respectively, as compared to 0.25G-C specimens ($p<0.05$). Significant changes in MAR were not observed between 0.25G groups, nor were alterations in MS, MAS, and BFR observed for 1G-SWT and 1G-LIPUS specimens as compared to 1G-C specimens.

Table 5. Mean (standard deviation) μCT and histological results for 0.25G specimens. Statistical significance between groups is denoted by like letters ($p<0.05$).

Experimental Parameter	0.25G-SWT	0.25G-LIPUS	0.25G-C	1G-SWT	1G-LIPUS	1G-C
μCT						
Callus BV [mm^3]	45.22 (31.39)^{A,B}	109.34 (65.36)^{C,D}	71.27 (23.26)^{E,F}	422.04 (208.36)^{A,C,E,G,H}	167.84 (131.42)^{G,I}	637.14 (177.50)^{B,D,F,H,I}
Fracture Gap BV/TV [%]	0.03 (0.02)	0.04 (0.03)	0.06 (0.05)	0.08 (0.04)	0.10 (0.12)	0.06 (0.03)
Callus BMD [mgHa/ccm]	844.29 (69.39)^{A}	797.58 (86.65)	783.55 (95.60)	654.78 (15.29)^{A}	706.62 (42.66)	709.82 (71.22)
Fracture Gap BMD [mgHa/ccm]	725.59 (74.92)	766.46 (93.86)	681.40 (19.60)	649.56 (34.19)	697.67 (73.92)	738.96 (162.83)
Histomorphometry						
Callus BV/TV [%]	22.76 (17.98)^{A,E}	59.98 (3.28)^{A,B,C,D}	23.32 (15.56)^{B,F}	28.93 (9.38)^{C,G}	55.42 (7.65)^{E,F,G,H}	24.98 (7.48)^{D,H}
Intracortical BV/TV [%]	8.89 (7.22)	10.44 (5.54)	5.72 (2.82)	10.40 (9.18)	11.97 (5.76)	6.11 (4.41)
Intramedullary BV/TV [%]	7.13 (13.53)	7.99 (12.61)	0.30 (0.36)	20.25 (12.29)	11.52 (18.85)	11.15 (17.14)
Mineralizing Surface [%]	0.64 (0.04)^{A,B}	0.80 (.014)^{A,C,D,E,F}	0.42 (0.08)^{B,C,G}	0.62 (0.06)^{D}	0.63 (0.06)^{E}	0.53 (0.02)^{F,G}
Mineral Apposition Rate [μm/d]	3.50 (0.61)	2.83 (0.58)	2.78 (0.65)^{A}	3.51 (0.64)	3.82 (0.74)	4.47 (0.33)^{A}
Bone Formation Rate [μm/d]	2.20 (0.35)^{A}	2.10 (0.12)^{B}	1.17 (0.41)^{A,B,C}	2.15 (0.25)	2.36 (0.33)	2.39 (0.28)^{C}
Periosteal Ob.N [mm^{-1}]	26.91 (3.98)^{A,B}	31.63 (5.01)^{C}	14.37 (2.01)^{A,C,D,E,F}	29.59 (3.61)^{D,G}	35.38 (5.48)^{B,E,G,H}	26.89 (5.68)^{F,H}
Periosteal Oc.N [mm^{-1}]	0.01 (0.03)^{A}	0.07 (0.09)^{B}	0.37 (0.32)^{A,B,C}	0.12 (0.16)	0.18 (0.22)	0.01 (0.05)^{C}
Endosteal Ob.N [mm^{-1}]	29.38 (8.41)^{A,B}	40.08 (4.76)^{A,C,D,D,E,F}	11.66 (2.44)^{B,C,G,H,I}	27.14 (3.79)^{D,G}	30.50 (5.10)^{E,H}	25.83 (7.39)^{F,I}
Endosteal Oc.N [mm^{-1}]	0.12 (0.11)	0.09 (0.16)	0.65 (0.73)^{A}	0.04 (0.06)	0.04 (0.07)	0.03 (0.02)^{A}

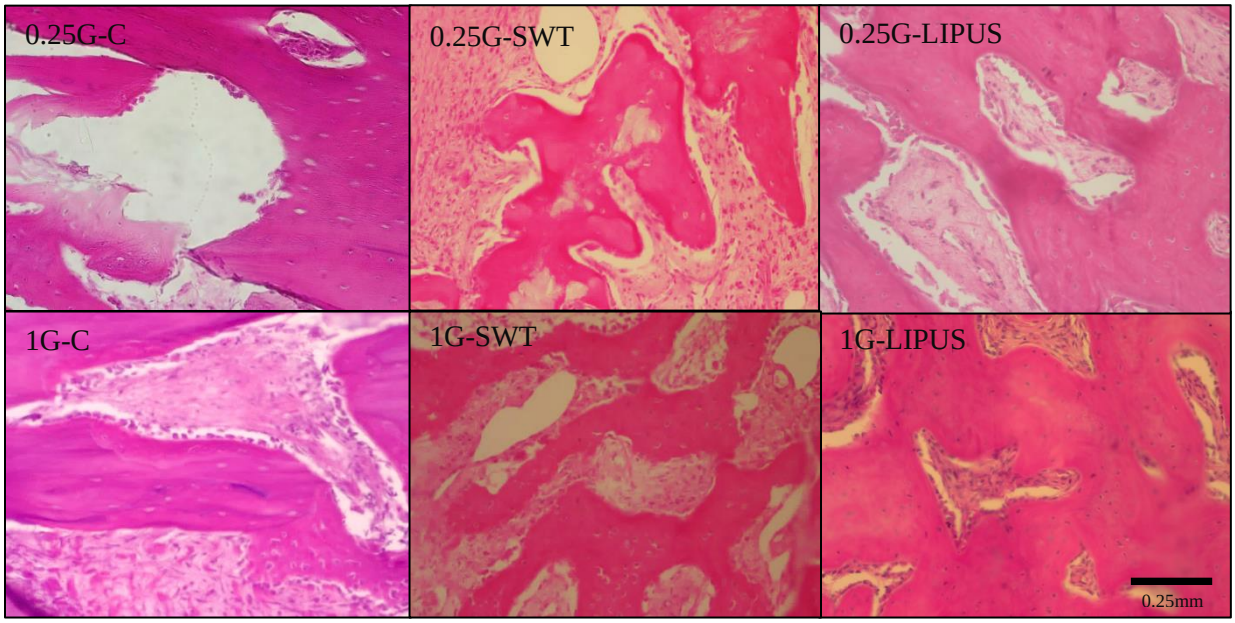

Figure 31. Osteoblast numbers within the periosteal callus were significantly elevated ($p<0.05$) in 0.25G specimens treated with SWT (0.25G-SWT, top middle) and LIPUS (0.25G-LIPUS, top right) as compared to those that received no treatment (0.25G-C,top left). (Bottom) No significant alterations were observed between 1G groups.

Discussion

Due to the increasing duration of space exploration missions and delayed fracture healing experienced during weightlessness, it is imperative to develop feasible countermeasures that may be employed in the event that bony fracture occurs. This study investigated the effect of SWT and LIPUS on the acute phase of fractures healing in a simulated microgravity environment. The treatment parameters utilized in the current investigation were in accordance with those previously reported for other animal studies for the treatment of delayed fracture healing (54, 61, 66, 142, 152).

The results of the *in vivo* DEXA scans demonstrated no relationship between SWT or LIPUS and regional metatarsal BMD under 1G or 0.25G loading conditions, indicating that any effects of the two treatments were localized to the healing fracture and did not result in any systemic catabolic or anabolic osteogenic alterations. *In vivo* measurements of orthopaedic fixation plate strain did not result in statistically discernible differences in fracture healing during the course of the study following treatment within either the 0.25G or 1G groups. Similar results were observed in the four-point bending experiment wherein no statistically significant alterations in bending stiffness were observed following SWT or LIPUS treatment under 1G or 0.25G loading. Further, SWT and LIPUS treatment failed to alter the BMD of the healing callus and fracture gap for both loading conditions. While callus bone volume was not affected by SWT treatment under 1G and 0.25G loading conditions, callus bone volume was significantly decreased in 1G specimens treated with LIPUS. This change was not reflected in in 0.25G specimens treated with LIPUS. Histomorphometric analyses demonstrated an increase in callus BV/TV in 1G-LIPUS specimens, resulting in a more-condensed callus than the 1G-SWT and 1G-C groups, and may explain why the overall loss of callus volume did not significantly alter the mechanical competency of 1G-LIPUS specimens as compared to the other 1G groups.

Despite limited changes in mechanical fracture strength, SWT and LIPUS significantly increased periosteal and endosteal osteoblast numbers while decreasing periosteal osteoclast numbers in 0.25G specimens. These results reflect those observed when SWT and LIPUS were utilized to stimulate murine osteoblast cells, inducing increased osteoblast differentiation and decreased pro-osteoclastogenic factors (140, 158). Similarly, this study demonstrated significantly elevated MS and BFR within the periosteal callus of 0.25G specimens as a result of both treatments, while

not significantly altering MAR values. These data, taken together, indicate that the overall amount of osteoblast activity and resulting increase in net active surface area and not overall mineralization rate following LIPUS and SWT were responsible for an overall elevation of bone formation. These findings are particularly important as they demonstrated a return in cellular numbers in reduced loading specimens to those experienced in an Earth 1G gravitational environment. Although mechanical strength of the 0.25G-SWT and 0.25G-LIPUS specimens was not enhanced at the time of sacrifice, it is possible that mechanical integrity would be elevated with respect to 0.25G-C specimens for longer duration fracture healing given the increased differentiation of osteoblast cells and subsequent increase in BFR. It is interesting to note that cellular numbers and mineralization rates were unchanged in 1G-SWT and 1G-LIPUS specimens as compared to 1G-C specimens, indicating that SWT and LIPUS treatment may be beneficial in situations involving aberrant fracture healing but elicit minimal modifications to the normal healing sequelae.

It is possible that the high energy levels of the shock waves delivered during treatment induced trauma at the fracture site, further delaying the proliferation of osteogenic tissue. It has been previously reported that SWT can initiate damage, producing cortical cracking at high powers (136). However, over 10,000 shocks were necessary to observe cracking in cortical bone. The few *in vivo* studies investigating the dose-dependent relationship between SWT power and healing advocate relatively high energy levels to observe distinguishable enhancements in fracture healing, indicating that the relationship between treatment power, overall fracture healing rate, and bone damage threshold is not currently well-understoood (7, 142, 152). While major cortical defects were not observed in this study, it is possible that unnoticed damage was

induced by SWT to induce a delay in fracture healing. It is not believed that microdamage occurred following LIPUS treatment due to the relatively low energy level used in LIPUS as compared to SWT.

There were several limitations associated with this study. First, the time span of this study allowed the investigation of the acute stages of healing in which signs of aberrant fracture healing would be most critical; however, long-term alterations in fracture healing due to SWT and LIPUS in simulated microgravity remain unknown. Further, the localized nature of the unloading technique utilized in this model did not allow the investigation of systemic alterations associated with simulated microgravity unloading such as changes in fluid balance. Finally, the fracture healing angiogenic response was not characterized.

The data reported herein provides strong evidence that SWT and LIPUS elevate osteoblast numbers and bone formation rates as well as decrease osteoclast numbers in a large animal model of simulated microgravity. Although no increase in 4-week mechanical strength was observed, it is possible that an increase in fracture healing (i.e. callus mechanical competence) would be experienced at longer timepoints under simulated microgravity conditions given the up-regulation of osteoblast numbers and bone formation parameters following SWT and LIPUS. Further investigation of the dose-dependent relationship of SWT and LIPUS in a large animal model as well as their effects on longer duration fracture healing will provide valuable information regarding their efficacy as a countermeasure to the inhibited fracture healing encountered during spaceflight.

CHAPTER 6:

CONCLUSION

Summary of Findings & Future Work

Simulated microgravity-related alterations in fracture healing were investigated in this study. The employed methodology was based on (1) *in vivo* experimentation on skeletally mature female ewes to interrogate fracture healing and possible therapeutic countermeasures, and (2) finite element modeling of the ovine hindlimb under simulated microgravity and Earth gravity loading conditions to characterize the micromechanical environment of healing fractures.

In Chapter 2, a ground-based, ovine model of skeletal unloading was developed in order to simulate a microgravity loading condition. The external fixation unloading technique utilized in this model was able to induce mechanical unloading of the metatarsus and significant alterations in the relevant radiographical, biomechanical, and histomorphometric parameters characteristic of spaceflight. Specifically, the newly developed ovine model captured the characteristic decrease in osteoblast numbers and increase in osteoclast activity associated with human spaceflight. The unloading methodology described in Chapter 2 was extended to the investigation of fracture healing in a simulated microgravity loading environment in Chapter 3. The findings of this study revealed that the mechanical loading environment dramatically affects the fracture healing cascade and resultant mineralized tissue strength, and that animals that healed in a reduced loading environment demonstrated significant reductions in healing rate and callus mechanical competency as compared to animals healing in a 1G Earth gravitational environment.

Chapter 4 outlined the development of a finite element of the ovine hindlimb in order to characterize the localized mechanical environment of a healing fracture in simulated microgravity and Earth gravitational environments. External fixation componentry was modeled to mimic the experimental methodology detailed in Chapter 3 and correlate model predictions to experimental outcomes. The findings of this chapter indicate that simulated microgravity unloading decreases hydrostatic stress and principal strain within the callus and fracture gap, resulting in primarily intramembranous bone formation rather than the endochondral bone formation pathway characteristic of Earth-based fracture healing.

Finally, in Chapter 5, two therapeutic countermeasures to the inhibited fracture healing of simulated microgravity unloading were investigated. The methodology of Chapter 3 was replicated, and shock wave therapy and low-intensity pulsed ultrasound were administered to animals healing in simulated microgravity and Earth gravitational loading environments. While fracture mechanical competency was not significantly altered following either countermeasure, both treatments significantly elevated osteoblast numbers and bone formation rates in simulated microgravity animals. The outcome of this chapter suggests that shock wave therapy and low-intensity pulsed ultrasound may be beneficial in situations involving aberrant fracture healing but elicit minimal modifications to the normal healing sequelae.

While the results reported in this dissertation work provide an initial foundation to the understanding of fracture healing in reduced gravitational loading environments and possible countermeasures to the negative effects of reduced mechanical loading, additional investigations

are warranted. Further investigation of the dose-dependent relationship and long-term healing characteristics of shock wave therapy and low-intensity pulsed will provide valuable information regarding their efficacy as a countermeasure during long-duration spaceflight. These efforts, as well as the investigation of other countermeasures, should be part of future simulated microgravity fracture healing work.

REFERENCES

1. Abram AC, Keller TS, Spengler DM. The effects of simulated weightlessness on bone biomechanical and biochemical properties in the maturing rat. Journal of biomechanics. 1988;21(9):755-67.

2. Allen MR, Bloomfield SA. Hindlimb unloading has a greater effect on cortical compared with cancellous bone in mature female rats. J Appl Physiol. 2003;94(2):642-50.

3. Allen MR, Hogan HA, Bloomfield SA. Differential bone and muscle recovery following hindlimb unloading in skeletally mature male rats. Journal of musculoskeletal & neuronal interactions. 2006;6(3):217-25.

4. Anderson AE, Ellis BJ, Weiss JA. Verification, validation and sensitivity studies in computational biomechanics. Computer methods in biomechanics and biomedical engineering. 2007;10(3):171-84.

5. Androjna C, McCabe NP, Cavanagh P.R., Midura RJ. Effects of Spaceflight and Skeletal Unloading on Bone Fracture Healing. Clinic Rev Bone Miner Metab. 2012(10):61-70.

6. Androjna C, McCabe, N.P., Cavanagh, P.R., Midura, R.J. Effects of spaceflight and skeletal unloading on bone fracture healing. Clin Rev Bone Miner Metab.

7. Augat P, Claes L, Suger G. In vivo effect of shock-waves on the healing of fractured bone. Clin Biomech (Bristol, Avon). 1995;10(7):374-8.

8. Ayturk UM. Development and validation of a three dimensional high resolution nonlinear finite element model of an L3/L4 functional spinal unit [M s]: Colorado State University; 2007.

9. Ayturk UM, Gadomski B, Schuldt D, Patel V, Puttlitz CM. Modeling Degenerative Disk Disease in the Lumbar Spine: A Combined Experimental, Constitutive, and Computational Approach. J Biomech Eng-T Asme. 2012;134(10).

10. Ayturk UM, Puttlitz CM. Parametric convergence sensitivity and validation of a finite element model of the human lumbar spine. Computer methods in biomechanics and biomedical engineering. 2011;14(8):695-705.

11. Basso N, Bellows CG, Heersche JNM. Effect of simulated weightlessness on osteoprogenitor cell number and proliferation in young and adult rats. Bone. 2005;36(1):173-83.

12. Basso N, Jia Y, Bellows CG, Heersche JN. The effect of reloading on bone volume, osteoblast number, and osteoprogenitor characteristics: studies in hind limb unloaded rats. Bone. 2005;37(3):370-8.

13. Bikle DD, Halloran BP. The response of bone to unloading. Journal of bone and mineral metabolism. 1999;17(4):233-44.

14. Bloomfield SA, Allen MR, Hogan HA, Delp MD. Site- and compartment-specific changes in bone with hindlimb unloading in mature adult rats. Bone. 2002;31(1):149-57.

15. Bouxsein ML, Boyd SK, Christiansen BA, Guldberg RE, Jepsen KJ, Muller R. Guidelines for assessment of bone microstructure in rodents using micro-computed tomography. Journal of bone and mineral research : the official journal of the American Society for Bone and Mineral Research. 2010;25(7):1468-86.

16. Bronk JT, Meadows TH, Kelly PJ. The Relationship of Increased Capillary Filtration and Bone-Formation. Clinical orthopaedics and related research. 1993(293):338-45.

17. Buckwalter JA, Mower D, Ungar R, Schaeffer J, Ginsberg B. Morphometric analysis of chondrocyte hypertrophy. The Journal of bone and joint surgery American volume. 1986;68(2):243-55.

18. Burger EH, Klein-Nulend J. Mechanotransduction in bone--role of the lacuno-canalicular network. FASEB journal : official publication of the Federation of American Societies for Experimental Biology. 1999;13 Suppl:S101-12.

19. Burger EH, Klein-Nulend J, van der Plas A, Nijweide PJ. Function of osteocytes in bone--their role in mechanotransduction. The Journal of nutrition. 1995;125(7 Suppl):2020S-3S.

20. Caillot-Augusseau A, Lafage-Proust MH, Soler C, Pernod J, Dubois F, Alexandre C. Bone formation and resorption biological markers in cosmonauts during and after a 180-day space flight (Euromir 95). Clinical chemistry. 1998;44(3):578-85.

21. Cardarelli F, SpringerLink (Online service). Materials handbook a concise desktop reference. London: Springer,; 2008. Available from: https://ezproxy2.library.colostate.edu/login?url=http://dx.doi.org/10.1007/978-1-84628-669-8.

22. Carter DR, Beaupre GS, Giori NJ, Helms JA. Mechanobiology of skeletal regeneration. Clinical orthopaedics and related research. 1998(355):S41-S55.

23. Carter DR, Blenman PR, Beaupre GS. Correlations between Mechanical-Stress History and Tissue Differentiation in Initial Fracture-Healing. J Orthopaed Res. 1988;6(5):736-48.

24. Carter DR, Spengler DM. Mechanical properties and composition of cortical bone. Clinical orthopaedics and related research. 1978(135):192-217.

25. Chavassieux P, Pastoureau P, Boivin G, Chapuy MC, Delmas PD, Milhaud G, Meunier PJ. Fluoride-Induced Bone Changes in Lambs during and after Exposure to Sodium-Fluoride. Osteoporosis Int. 1991;2(1):26-33.

26. Choi P, Ogilvie C, Thompson Z, Miclau T, Helms JA. Cellular and molecular characterization of a murine non-union model. J Orthopaed Res. 2004;22(5):1100-7.

27. Chow DH, Suen PK, Fu LH, Cheung WH, Leung KS, Wong MW, Qin L. Extracorporeal shockwave therapy for treatment of delayed tendon-bone insertion healing in a rabbit model: a dose-response study. The American journal of sports medicine. 2012;40(12):2862-71.

28. Christensen NJ, Heer M, Ivanova K, Norsk P. Sympathetic nervous activity decreases during head down bed rest but not during microgravity. Microgravity Sci Tec. 2007;19(5-6):95-7.

29. Claes LE, Heigele CA. Magnitudes of local stress and strain along bony surfaces predict the course and type of fracture healing. Journal of biomechanics. 1999;32(3):255-66.

30. Claes LE, Wilke HJ, Augat P, Rubenacker S, Margevicius KJ. Effect of dynamization on gap healing of diaphyseal fractures under external fixation. Clin Biomech (Bristol, Avon). 1995;10(5):227-34.

31. Collet P, Uebelhart D, Vico L, Moro L, Hartmann D, Roth M, Alexandre C. Effects of 1- and 6-month spaceflight on bone mass and biochemistry in two humans. Bone. 1997;20(6):547-51.

32. Cuppone M, Seedhom BB, Berry E, Ostell AE. The longitudinal Young's modulus of cortical bone in the midshaft of human femur and its correlation with CT scanning data. Calcified tissue international. 2004;74(3):302-9.

33. Deavers DR, Musacchia XJ. Water Metabolism and Renal-Function during Hibernation and Hypothermia. Fed Proc. 1980;39(12):2969-73.

34. Deavers DR, Musacchia XJ, Meininger GA. Model for antiorthostatic hypokinesia: head-down tilt effects on water and salt excretion. J Appl Physiol. 1980;49(4):576-82.

35. Dehority W, Halloran BP, Bikle DD, Curren T, Kostenuik PJ, Wronski TJ, Shen Y, Rabkin B, Bouraoui A, Morey-Holton E. Bone and hormonal changes induced by skeletal unloading in the mature male rat. The American journal of physiology. 1999;276(1 Pt 1):E62-9.

36. Dempster DW, Compston JE, Drezner MK, Glorieux FH, Kanis JA, Malluche H, Meunier PJ, Ott SM, Recker RR, Parfitt AM. Standardized Nomenclature, Symbols, and Units for Bone Histomorphometry: A 2012 Update of the Report of the ASBMR Histomorphometry Nomenclature Committee. J Bone Miner Res. 2013;28(1):1-16.

37. den Boer FC, Patka P, Bakker FC, Wippermann BW, van Lingen A, Vink GQ, Boshuizen K, Haarman HJ. New segmental long bone defect model in sheep: quantitative analysis of healing with dual energy x-ray absorptiometry. Journal of orthopaedic research : official publication of the Orthopaedic Research Society. 1999;17(5):654-60.

38. Donahue SW, Galley SA. Microdamage in bone: implications for fracture, repair, remodeling, and adaptation. Critical reviews in biomedical engineering. 2006;34(3):215-71.

39. Draper ER, Goodship AE. A novel technique for four-point bending of small bone samples with semi-automatic analysis. Journal of biomechanics. 2003;36(10):1497-502.

40. Durnova GN, Burkovskaya TE, Vorotnikova EV, Kaplansky AS, Arustamov OV. The Effect of Microgravity on Fracture-Healing of Rats Flown on Cosmos-2044. Kosm Biol Aviak Med+. 1991;25(5):29-33.

41. Egermann M, Goldhahn J, Holz R, Schneider E, Lill CA. A sheep model for fracture treatment in osteoporosis: benefits of the model versus animal welfare. Laboratory animals. 2008;42(4):453-64.

42. Einhorn TA. The cell and molecular biology of fracture healing. Clinical orthopaedics and related research. 1998(355):S7-S21.

43. Elster EA, Stojadinovic A, Forsberg J, Shawen S, Andersen RC, Schaden W. Extracorporeal Shock Wave Therapy for Nonunion of the Tibia. Journal of Orthopaedic Trauma. 2010;24(3):133-41.

44. Ferguson C, Alpern E, Miclau T, Helms JA. Does adult fracture repair recapitulate embryonic skeletal formation? Mech Develop. 1999;87(1-2):57-66.

45. Ferguson CM, Miclau T, Hu D, Alpern E, Helms JA. Common molecular pathways in skeletal morphogenesis and repair. Morphogenesis: Cellular Interactions. 1998;857:33-42.

46. Fortrat JO, Sigaudo D, Hughson RL, Maillet A, Yamamoto Y, Gharib C. Effect of prolonged head-down bed rest on complex cardiovascular dynamics. Auton Neurosci-Basic. 2001;86(3):192-201.

47. Furia JP, Juliano PJ, Wade AM, Schaden W, Mittermayr R. Shock Wave Therapy Compared with Intramedullary Screw Fixation for Nonunion of Proximal Fifth Metatarsal Metaphyseal-Diaphyseal Fractures. Journal of Bone and Joint Surgery-American Volume. 2010;92A(4):846-54.

48. Gadomski BC, Mcgilvray KC, Easley JT, Palmer RH, Ehrhart EJ, Haussler KK, Browning RC, Santoni BG, Puttlitz CM. An *In Vivo* Model of Bone Tissue Alterations in Simulated Microgravity Conditions. J Biomech Engr. 2014;136(2):021020 1-9.

49. Gadomski BC, McGilvray KC, Easley JT, Palmer RH, Santoni BG, Puttlitz CM. Partial gravity unloading inhibits bone healing responses in a large animal model. Journal of biomechanics. 2014;47(12):2836-42.

50. Gharib C, Custaud MA. Orthostatic tolerance after spaceflight or simulated weightlessness by head-down bed-rest. B Acad Nat Med Paris. 2002;186(4):733-49.

51. Giangregorio L, Blimkie CJ. Skeletal adaptations to alterations in weight-bearing activity: a comparison of models of disuse osteoporosis. Sports Med. 2002;32(7):459-76.

52. Grigoriev AI, Morukov BV, Oganov VS, Rakhmanov AS, Buravkova LB. Effect of Exercise and Bisphosphonate on Mineral Balance and Bone-Density during 360 Day Antiorthostatic Hypokinesia. J Bone Miner Res. 1992;7:S449-S55.

53. Hadjiargyrou M, McLeod K, Ryaby JP, Rubin C. Enhancement of fracture healing by low intensity ultrasound. Clinical orthopaedics and related research. 1998(355):S216-S29.

54. Hantes ME, Mavrodontidis AN, Zalavras CG, Karantanas AH, Karachalios T, Malizos KN. Low-intensity transosseous ultrasound accelerates osteotomy healing in a sheep fracture model. Journal of Bone and Joint Surgery-American Volume. 2004;86A(10):2275-82.

55. Hardy R, Cooper MS. Bone loss in inflammatory disorders. J Endocrinol. 2009;201(3):309-20.

56. Heckman JD, Ryaby JP, McCabe J, Frey JJ, Kilcoyne RF. Acceleration of tibial fracture-healing by non-invasive, low-intensity pulsed ultrasound. The Journal of bone and joint surgery American volume. 1994;76(1):26-34.

57. Hee CK, Dines JS, Dines DM, Roden CM, Wisner-Lynch LA, Turner AS, McGilvray KC, Lyons AS, Puttlitz CM, Santoni BG. Augmentation of a rotator cuff suture repair using rhPDGF-BB and a type I bovine collagen matrix in an ovine model. The American journal of sports medicine. 2011;39(8):1630-9.

58. Hefferan TE, Evans GL, Lotinun S, Zhang M, Morey-Holton E, Turner RT. Effect of gender on bone turnover in adult rats during simulated weightlessness. J Appl Physiol. 2003;95(5):1775-80.

59. Helgason B, Perilli E, Schileo E, Taddei F, Brynjolfsson S, Viceconti M. Mathematical relationships between bone density and mechanical properties: A literature review. Clin Biomech. 2008;23(2):135-46.

60. Holick MF. Perspective on the impact of weightlessness on calcium and bone metabolism. Bone. 1998;22(5 Suppl):105S-11S.

61. Hsu RWW, Tai CL, Chen CYC, Hsu WH, Hsueh S. Enhancing mechanical strength during early fracture healing via shockwave treatment: an animal study. Clin Biomech. 2003;18(6):S33-S9.

62. Hutton WC, Yoon ST, Elmer WA, Li J, Murakami H, Minamide A, Akamaru T. Effect of tail suspension (or simulated weightlessness) on the lumbar intervertebral disc - Study of proteoglycans and collagen. Spine. 2002;27(12):1286-90.

63. Ioppolo F, Rompe JD, Furia JP, Cacchio A. Clinical application of shock wave therapy (SWT) in musculoskeletal disorders. European journal of physical and rehabilitation medicine. 2014;50(2):217-30.

64. Isaksson H, Van Donkelaar CC, Huiskes R, Ito K. Corroboration of mechanoregulatory algorithms for tissue differentiation during fracture healing: Comparison with in vivo results. J Orthopaed Res. 2006;24(5):898-907.

65. Isaksson H, Wilson W, van Donkelaar CC, Huiskes R, Ito K. Comparison of biophysical stimuli for mechano-regulation of tissue differentiation during fracture healing. Journal of biomechanics. 2006;39(8):1507-16.

66. Johannes EJ, Sukul DMKSK, Matura E. High-Energy Shock-Waves for the Treatment of Nonunions - an Experiment on Dogs. J Surg Res. 1994;57(2):246-52.

67. Jones AC, Wilcox RK. Finite element analysis of the spine: towards a framework of verification, validation and sensitivity analysis. Medical engineering & physics. 2008;30(10):1287-304.

68. Judex S, Boyd S, Qin YX, Turner S, Ye K, Muller R, Rubin C. Adaptations of trabecular bone to low magnitude vibrations result in more uniform stress and strain under load. Annals of biomedical engineering. 2003;31(1):12-20.

69. Kaplansky AS, Durnova GN, Burkovskaya TE, Vorotnikova EV. The effect of microgravity on bone fracture healing in rats flown on Cosmos-2044. The Physiologist. 1991;34(1 Suppl):S196-9.

70. Keyak JH, Kaneko TS, Tehranzadeh J, Skinner HB. Predicting proximal femoral strength using structural engineering models. Clinical orthopaedics and related research. 2005(437):219-28.

71. Keyak JH, Koyama AK, LeBlanc A, Lu Y, Lang TF. Reduction in proximal femoral strength due to long-duration spaceflight. Bone. 2009;44(3):449-53.

72. Kirchen ME, Oconnor KM, Gruber HE, Sweeney JR, Fras IA, Stover SJ, Sarmiento A, Marshall GJ. Effects of Microgravity on Bone Healing in a Rat Fibular Osteotomy Model. Clinical orthopaedics and related research. 1995(318):231-42.

73. Kolar P, Gaber T, Perka C, Duda GN, Buttgereit F. Human Early Fracture Hematoma Is Characterized by Inflammation and Hypoxia. Clinical orthopaedics and related research. 2011;469(11):3118-26.

74. Lacroix D, Prendergast PJ. A mechano-regulation model for tissue differentiation during fracture healing: analysis of gap size and loading. Journal of biomechanics. 2002;35(9):1163-71.

75. Lang SB. Ultrasonic Method for Measuring Elastic Coefficients of Bone and Results on Fresh and Dried Bovine Bones. Ieee T Bio-Med Eng. 1970;Bm17(2):101-5.

76. Lang T, LeBlanc A, Evans H, Lu Y, Genant H, Yu A. Cortical and trabecular bone mineral loss from the spine and hip in long-duration spaceflight. J Bone Miner Res. 2004;19(6):1006-12.

77. Lang TF. What do we know about fracture risk in long-duration spaceflight? Journal of musculoskeletal & neuronal interactions. 2006;6(4):319-21.

78. Le AX, Miclau T, Hu D, Helms JA. Molecular aspects of healing in stabilized and non-stabilized fractures. J Orthopaed Res. 2001;19(1):78-84.

79. Leahy PD, Smith BS, Easton KL, Kawcak CE, Eickhoff JC, Shetye SS, Puttlitz CM. Correlation of mechanical properties within the equine third metacarpal with trabecular bending and multi-density micro-computed tomography data. Bone. 2010;46(4):1108-13.

80. Leblanc A, Schneider V, Krebs J, Evans H, Jhingran S, Johnson P. Spinal Bone-Mineral after 5 Weeks of Bed Rest. Calcified tissue international. 1987;41(5):259-61.

81. Leblanc AD, Schneider VS, Evans HJ, Engelbretson DA, Krebs JM. Bone mineral loss and recovery after 17 weeks of bed rest. Journal of bone and mineral research : the official journal of the American Society for Bone and Mineral Research. 1990;5(8):843-50.

82. Leong PL, Morgan EF. Measurement of fracture callus material properties via nanoindentation. Acta Biomater. 2008;4(5):1569-75.

83. Lerner Z, Gadomski, BG., Haussler, K., Puttlitz, CM., Browning, RC. Modulating Tibiofemoral Contact Forces in the Sheep Hindlimb via Treadmill Walking: Predictions from an OpenSim Musculoskeletal Model. J Orthopaed Res. 2014.

84. Liang XD, Zhang L, Wan YF, Yu XY, Guo YM, Chen XP, Tan C, Huang TL, Shen HJ, Chen XY, Li H, Lv K, Sun F, Chen SG, Guo J. Changes in the Diurnal Rhythms during a 45-Day Head-Down Bed Rest. PloS one. 2012;7(10).

85. Lipson SF, Katz JL. The Relationship between Elastic Properties and Microstructure of Bovine Cortical Bone. Journal of biomechanics. 1984;17(4):231-5&7-40.

86. Lyons AS, Sherman BP, Puttlitz CM, Patel VV, Abjornson C, Turner AS, Seim HB, 3rd, Burger EL, Lindley EM. Failure of resorbable plates and screws in an ovine model of anterior cervical discectomy and fusion. The spine journal : official journal of the North American Spine Society. 2011;11(9):876-83.

87. Martin RB, Burr DB. Structure, function, and adaptation of compact bone. New York: Raven Press; 1989. 275 p. p.

88. Martinez DA, Vailas AC, Vanderby R, Grindeland RE. Temporal extracellular matrix adaptations in ligament during wound healing and hindlimb unloading. Am J Physiol-Reg I. 2007;293(4):R1552-R60.

89. Martini L, Fini M, Giavaresi G, Giardino R. Sheep model in orthopedic research: a literature review. Comparative medicine. 2001;51(4):292-9.

90. Matos MA, Araujo FP, Paixao FB. Histomorphometric evaluation of bone healing in rabbit fibular osteotomy model without fixation. Journal of orthopaedic surgery and research. 2008;3:4.

91. Matsumoto T, Nakayama K, Kodama Y, Fuse H, Nakamura T, Fukumoto S. Effect of mechanical unloading and reloading on periosteal bone formation and gene expression in tail-suspended rapidly growing rats. Bone. 1998;22(5 Suppl):89S-93S.

92. Miclau T, Lu C, Thompson Z, Choi P, Puttlitz C, Marcucio R, Helms JA. Effects of delayed stabilization on fracture healing. J Orthopaed Res. 2007;25(12):1552-8.

93. Midura RJ, Su X, Androjna C. A simulated weightlessness state diminishes cortical bone healing responses. Journal of musculoskeletal & neuronal interactions. 2006;6(4):327-8.

94. Mittra E, Rubin C, Qin YX. Interrelationship of trabecular mechanical and microstructural properties in sheep trabecular bone. Journal of biomechanics. 2005;38(6):1229-37.

95. Morey-Holton ER, Globus RK. Hindlimb unloading of growing rats: a model for predicting skeletal changes during space flight. Bone. 1998;22(5 Suppl):83S-8S.

96. Mow VC, Huiskes R. Basic orthopaedic biomechanics & mechano-biology. 3rd ed. Philadelphia: Lippincott Williams & Wilkins; 2005. xvi, 720 p. p.

97. Musacchia XJ, Deavers DR, Meininger GA. Fluid/electrolyte balance and cardiovascular responses: head-down tilted rats. The Physiologist. 1990;33(1 Suppl):S46-7.

98. Nafei A, Danielsen CC, Linde F, Hvid I. Properties of growing trabecular ovine bone - Part I: Mechanical and physical properties. Journal of Bone and Joint Surgery-British Volume. 2000;82B(6):910-20.

99. Nafei A, Kabel J, Odgaard A, Linde F, Hvid I. Properties of growing trabecular ovine bone - Part II: Architectural and mechanical properties. Journal of Bone and Joint Surgery-British Volume. 2000;82B(6):921-7.

100. Nelson ES, Lewandowski B, Licata A, Myers JG. Development and validation of a predictive bone fracture risk model for astronauts. Annals of biomedical engineering. 2009;37(11):2337-59.

101. Newman E, Turner AS, Wark JD. The Potential of Sheep for the Study of Osteopenia - Current Status and Comparison with Other Animal-Models. Bone. 1995;16(4):S277-S84.

102. Newton BI, Cooper RC, Gilbert JA, Johnson RB, Zardiackas LD. The ovariectomized sheep as a model for human bone loss. Journal of comparative pathology. 2004;130(4):323-6.

103. Noble BS, Stevens H, Loveridge N, Reeve J. Identification of apoptotic changes in osteocytes in normal and pathological human bone. Bone. 1997;20(3):273-82.

104. Nonaka K, Fukuda S, Aoki K, Yoshida T, Ohya K. Regional distinctions in cortical bone mineral density measured by pQCT can predict alterations in material property at the tibial diaphysis of the Cynomolgus monkey. Bone. 2006;38(2):265-72.

105. Oganov VS, Rakhmanov AS, Novikov VE, Zatsepin ST, Rodionova SS, Cann C. The State of Human Bone Tissue during Space-Flight. Acta astronautica. 1991;23:129-33.

106. Osullivan ME, Bronk JT, Chao EYS, Kelly PJ. Experimental-Study of the Effect of Weight-Bearing on Fracture-Healing in the Canine Tibia. Clinical orthopaedics and related research. 1994(302):273-83.

107. Parfitt AM, Drezner MK, Glorieux FH, Kanis JA, Malluche H, Meunier PJ, Ott SM, Recker RR. Bone histomorphometry: standardization of nomenclature, symbols, and units. Report of the ASBMR Histomorphometry Nomenclature Committee. Journal of bone and mineral research : the official journal of the American Society for Bone and Mineral Research. 1987;2(6):595-610.

108. Pearce AI, Richards RG, Milz S, Schneider E, Pearce SG. Animal models for implant biomaterial research in bone: a review. European cells & materials. 2007;13:1-10.

109. Pounder NM, Harrison AJ. Low intensity pulsed ultrasound for fracture healing: a review of the clinical evidence and the associated biological mechanism of action. Ultrasonics. 2008;48(4):330-8.

110. Provenzano PP, Martinez DA, Grindeland RE, Dwyer KW, Turner J, Vailas AC, Vanderby R. Hindlimb unloading alters ligament healing. J Appl Physiol. 2003;94(1):314-24.

111. Puttlitz CM, Goel VK, Traynelis VC, Clark CR. A finite element investigation of upper cervical instrumentation. Spine. 2001;26(22):2449-55.

112. R.O. Ritchie JHK, J.J. Kruzic, R.K. Nall. A fracture mechanics and mechanistic approach to the failure of cortical bone. Fatigue Fract Engng Mater Struct. 2005;28:345-71.

113. Rambaut PC, Leach CS, Whedon GD. A study of metabolic balance in crewmembers of Skylab IV. Acta astronautica. 1979;6(10):1313-22.

114. Rawool NM, Goldberg BB, Forsberg F, Winder AA, Talish RJ, Hume E. Power Doppler assessment of vascular changes during fracture treatment with low intensity ultrasound. Radiology. 1997;205:1185-.

115. Rho JY, Hobatho MC, Ashman RB. Relations of mechanical properties to density and CT numbers in human bone. Medical engineering & physics. 1995;17(5):347-55.

116. Rho JY, Kuhn-Spearing L, Zioupos P. Mechanical properties and the hierarchical structure of bone. Medical engineering & physics. 1998;20(2):92-102.

117. Robling AG, Castillo AB, Turner CH. Biomechanical and molecular regulation of bone remodeling. Annual review of biomedical engineering. 2006;8:455-98.

118. Robling AG, Turner CH. Mechanotransduction in bone: genetic effects on mechanosensitivity in mice. Bone. 2002;31(5):562-9.

119. Rubin C, Bolander M, Ryaby JP, Hadjiargyrou M. The use of low-intensity ultrasound to accelerate the healing of fractures. Journal of Bone and Joint Surgery-American Volume. 2001;83A(2):259-70.

120. Rubin C, Turner AS, Muller R, Mittra E, McLeod K, Lin W, Qin YX. Quantity and quality of trabecular bone in the femur are enhanced by a strongly anabolic, noninvasive mechanical intervention. Journal of bone and mineral research : the official journal of the American Society for Bone and Mineral Research. 2002;17(2):349-57.

121. Rubin CT, Hausman MR. The Cellular Basis of Wolff Law - Transduction of Physical Stimuli to Skeletal Adaptation. Rheum Dis Clin N Am. 1988;14(3):503-17.

122. Santoni BG, McGilvray KC, Lyons AS, Bansal M, Turner AS, Macgillivray JD, Coleman SH, Puttlitz CM. Biomechanical analysis of an ovine rotator cuff repair via porous patch augmentation in a chronic rupture model. The American journal of sports medicine. 2010;38(4):679-86.

123. Santoni BG, Womack WJ, Wheeler DL, Puttlitz CM. A mechanical and computational investigation on the effects of conduit orientation on the strength of massive bone allografts. Bone. 2007;41(5):769-74.

124. Schaden W, Fischer A, Sailler A. Extracorporeal shock wave therapy of nonunion or delayed osseous union. Clinical orthopaedics and related research. 2001(387):90-4.

125. Schindeler A, McDonald MM, Bokko P, Little DG. Bone remodeling during fracture repair: The cellular picture. Semin Cell Dev Biol. 2008;19(5):459-66.

126. Seaton KA, Bowie KE, Sipes WA. Behavioral and Psychological Issues in Long-Duration Head-Down Bed Rest. Aviat Space Envir Md. 2009;80(5):A55-A61.

127. Seaton KA, Slack KJ, Sipes WA, Bowie KE. Cognitive Functioning In Long-Duration Head-Down Bed Rest. Aviat Space Envir Md. 2009;80(5):A62-A5.

128. Sessions ND, Halloran BP, Bikle DD, Wronski TJ, Cone CM, Morey-Holton E. Bone response to normal weight bearing after a period of skeletal unloading. The American journal of physiology. 1989;257(4 Pt 1):E606-10.

129. Shefelbine SJ, Simon U, Claes L, Gold A, Gabet Y, Bab I, Muller R, Augat P. Prediction of fracture callus mechanical properties using micro-CT images and voxel-based finite element analysis. Bone. 2005;36(3):480-8.

130. Shetye SS. Development of a novel endoprosthesis for canine limb-sparing using a finite element approach. [Dissertation]. Fort Collins, CO: Colorado State University; 2010.

131. Shimano MM, Volpon, J.B. Mechanical Behavior of rats' femoral proximal thirds after a period of tail suspension and exercises. Acta ortop bras. 2007;15(5):254-7.

132. Skerry TM, Bitensky L, Chayen J, Lanyon LE. Early strain-related changes in enzyme activity in osteocytes following bone loading in vivo. Journal of bone and mineral research : the official journal of the American Society for Bone and Mineral Research. 1989;4(5):783-8.

133. Smith SM, Nillen JL, Leblanc A, Lipton A, Demers LM, Lane HW, Leach CS. Collagen cross-link excretion during space flight and bed rest. J Clin Endocr Metab. 1998;83(10):3584-91.

134. Smith SM, Zwart SR, Heer MA, Baecker N, Evans HJ, Feiveson AH, Shackelford LC, Leblanc AD. Effects of artificial gravity during bed rest on bone metabolism in humans. J Appl Physiol. 2009;107(1):47-53.

135. Stoffel K, Klaue K, Perren SM. Functional load of plates in fracture fixation in vivo and its correlate in bone healing. Injury. 2000;31 Suppl 2:S-B37-50.

136. Sukul DMKSK, Johannes EJ, Pierik EGJM, Vaneijck GJWM, Kristelijn MJE. The Effect of High-Energy Shock-Waves Focused on Cortical Bone - an Invitro Study. J Surg Res. 1993;54(1):46-51.

137. Sweeney JR, Gruber HE, Kirchen ME, Marshall GJ. Effects of non weight bearing on callus formation. The Physiologist. 1985;28(6 Suppl):S63-4.

138. Swift JM, Nilsson MI, Hogan HA, Sumner LR, Bloomfield SA. Simulated resistance training during hindlimb unloading abolishes disuse bone loss and maintains muscle strength. Journal of bone and mineral research : the official journal of the American Society for Bone and Mineral Research. 2010;25(3):564-74.

139. Taibbi G, Kaplowitz K, Cromwell RL, Godley BF, Zanello SB, Vizzeri G. Effects of 30-Day Head-Down Bed Rest on Ocular Structures and Visual Function in a Healthy Subject. Aviat Space Envir Md. 2013;84(2):148-54.

140. Tamma R, Dell'Endice S, Notarnicola A, Moretti L, Patella S, Patella V, Zallone A, Moretti B. Extracorporeal Shock Waves Stimulate Osteoblast Activities. Ultrasound Med Biol. 2009;35(12):2093-100.

141. Thompson Z, Miclau T, Hu D, Helms JA. A model for intramembranous ossification during fracture healing. J Orthopaed Res. 2002;20(5):1091-8.

142. Tischer T, Milz F, Weiler C, Pautke C, Hausdorf J, Schmitz C, Maier M. Dose-dependent new bone formation by extracorporeal shock wave application on the intact femur of rabbits. Eur Surg Res. 2008;41(1):44-53.

143. Turner RT. Invited Review: What do we know about the effects of spaceflight on bone? J Appl Physiol. 2000;89:840-7.

144. Uebelhart D, Bernard J, Hartmann DJ, Moro L, Roth M, Uebelhart B, Rehailia M, Mauco G, Schmitt DA, Alexandre C, Vico L. Modifications of bone and connective tissue after orthostatic bedrest. Osteoporosis Int. 2000;11(1):59-67.

145. Vashishth D, Verborgt O, Divine G, Schaffler MB, Fyhrie DP. Decline in osteocyte lacunar density in human cortical bone is associated with accumulation of microcracks with age. Bone. 2000;26(4):375-80.

146. Vico L, Alexandre C. Microgravity and Bone Adaptation at the Tissue-Level. J Bone Miner Res. 1992;7:S445-S7.

147. Vico L, Chappard D, Alexandre C, Palle S, Minaire P, Riffat G, Morukov B, Rakhmanov S. Effects of a 120 Day Period of Bed-Rest on Bone Mass and Bone Cell Activities in Man - Attempts at Countermeasure. Bone Miner. 1987;2(5):383-94.

148. Vico L, Collet P, Guignandon A, Lafage-Proust MH, Thomas T, Rehaillia M, Alexandre C. Effects of long-term microgravity exposure on cancellous and cortical weight-bearing bones of cosmonauts. Lancet. 2000;355(9215):1607-11.

149. Vogel JM. Bone mineral measurement: Skylab experiment M-078. Acta astronautica. 1975;2(1-2):129-39.

150. Vulpiani MC, Vetrano M, Conforti F, Minutolo L, Trischitta D, Furia JP, Ferretti A. Effects of extracorporeal shock wave therapy on fracture nonunions. Am J Orthop (Belle Mead NJ). 2012;41(9):E122-7.

151. Wang CJ. An overview of shock wave therapy in musculoskeletal disorders. Chang Gung medical journal. 2003;26(4):220-32.

152. Wang CJ, Yang KD, Wang FS, Hsu CC, Chen HH. Shock wave treatment shows dose-dependent enhancement of bone mass and bone strength after fracture of the femur. Bone. 2004;34(1):225-30.

153. Weiner S, Wagner HD. The material bone: Structure mechanical function relations. Annu Rev Mater Sci. 1998;28:271-98.

154. Whedon GD, Lutwak L, Rambaut P, Whittle M, Leach C, Reid J, Smith M. Effect of weightlessness on mineral metabolism; metabolic studies on Skylab orbital space flights. Calcified tissue research. 1976;21 Suppl:423-30.

155. Woldtvedt DJ, Womack W, Gadomski BC, Schuldt D, Puttlitz CM. Finite Element Lumbar Spine Facet Contact Parameter Predictions are Affected by the Cartilage Thickness Distribution and Initial Joint Gap Size. J Biomech Eng-T Asme. 2011;133(6).

156. Wolf JH. [Julis Wolff and his "law of bone remodeling"]. Der Orthopade. 1995;24(5):378-86.

157. Womack W, Ayturk UM, Puttlitz CM. Cartilage Thickness Distribution Affects Computational Model Predictions of Cervical Spine Facet Contact Parameters. J Biomech Eng-T Asme. 2011;133(1).

158. Wu SL, Kawahara Y, Manabe T, Ogawa K, Matsumoto M, Sasaki A, Yuge L. Low-Intensity Pulsed Ultrasound Accelerates Osteoblast Differentiation and Promotes Bone Formation in an Osteoporosis Rat Model. Pathobiology. 2009;76(3):99-107.

159. Xu ZH, Jiang Q, Chen DY, Xiong J, Shi DQ, Yuan T, Zhu XL. Extracorporeal shock wave treatment in nonunions of long bone fractures. Int Orthop. 2009;33(3):789-93.

160. Yang P, Jia B, Ding C, Wang Z, Qian AR, Shang P. Whole-Body Vibration Effects on Bone Before and After Hind-Limb Unloading in Rats. Aviat Space Envir Md. 2009;80(2):88-93.

161. Zerwekh JE, Ruml LA, Gottschalk F, Pak CYC. The effects of twelve weeks of bed rest on bone histology, biochemical markers of bone turnover, and calcium homeostasis in eleven normal subjects. J Bone Miner Res. 1998;13(10):1594-601.